TUDelft

Delft University of Technology

Variability of the raindrop size distribution: model and estimation uncertainties across different scales

Gatidis, C.

DOI
10.4233/uuid:4a6b3544-c7ce-4456-af3e-000c64d531d7

Publication date
2024

Document Version
Final published version

Citation (APA)
Gatidis, C. (2024). *Variability of the raindrop size distribution: model and estimation uncertainties across different scales*. [Dissertation (TU Delft), Delft University of Technology]. https://doi.org/10.4233/uuid:4a6b3544-c7ce-4456-af3e-000c64d531d7

Important note
To cite this publication, please use the final published version (if applicable).
Please check the document version above.

Variability of the raindrop size distribution: model and estimation uncertainties across different scales

Variability of the raindrop size distribution: model and estimation uncertainties across different scales

Dissertation

for the purpose of obtaining the degree of doctor
at Delft University of Technology
by the authority of the Rector Magnificus, prof. dr. ir. T.H.J.J. van der Hagen,
chair of the Board for Doctorates
to be defended publicly on
Thursday 21 March 2024 at 12:30 o'clock

by

Christos *GATIDIS*

Master of Science in Atmospheric Sciences and the Environment
University of Ioannina, Ioannina, Greece
born in Kavala, Greece

This dissertation has been approved by the promotor and the copromotor.

Composition of the doctoral committee:
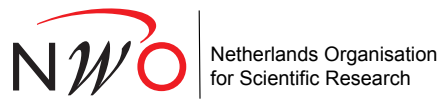
Typeset by the author with the LaTeX Documentation System.

An electronic version of this dissertation is available at
https://repository.tudelft.nl/.

Somewhere, something incredible is waiting to be known.

Carl Sagan

Contents

Summary

Precipitation is an important component for a range of different scientific sectors such as hydrology, numerical weather prediction, climate modeling etc. and needs to be carefully monitored. However, rainfall is extremely variable meteorological phenomenon in space and time making the measurement of rain notoriously challenging task. Point measurements provide generally accurate direct rain observations but their lack of spatial coverage is a significant limitation. On the contrary, radars are sensors capable of indirectly measuring rainfall over extended domains with higher level of uncertainty. For accurate rainfall estimates from weather radar, the complex microphysical properties of the rain must be known or inferred. The raindrop size distribution (DSD) statistically describes the microstructure of rainfall. However, similarly to rainfall, DSD also exhibits significant variability in space and time. The work in this thesis contributes to a better understanding of the small-scale variability of rainfall by investigating the DSD modeling and DSD estimation across different scales.

Initially the aspect of the DSD model was investigated. For remote sensing related applications it is often necessary to parameterize the DSD in a form of a simple distribution. Several mathematical models have been proposed in the literature to approximate naturally occurring DSDs with the gamma distribution to be the most common. Despite being the most widely accepted model, only a few studies have focused on precisely quantifying its adequacy. To investigate that, the gamma model was fitted to Parsivel optical disdrometer data collected during a two-month campaign in the Netherlands. The adequacy of the gamma model was analyzed using a combination of Kolmogorov–Smirnov goodness-of-fit test and Kullback–Leibler divergence. Then, the influence of the sampling resolution on the adequacy of the gamma model was studied. The findings show that the majority of the DSDs are not perfectly gamma but are well approximated by the gamma model at high sampling resolutions.

To better understand the DSD estimation in different scales, a widely used DSD retrieval technique based on polarimetric radar data was investigated. Critical assumptions behind the retrieval procedure were highlighted in order to outline potential sources of errors and uncertainties. An initial step involved a sensitivity analysis on a key component of the retrieval technique: the μ-Λ relationship. The μ-Λ relations are often taken for granted without much critical discussion neglecting the fact that the disdrometer data used to define them correspond to much smaller sampling volumes than the radar measurements to which they are applied. The overall analysis shows that the relationship remains remarkably robust, regardless of the sample size, sampling resolution, inter-event variability, or adequacy of the gamma model. Then, the influence of calibration errors in radar observations and scale differences between radar and disdrometer observations were studied. The calibration correction significantly improved the accuracy of the retrievals. Determining the scale correction, on the contrary, proved to be challenging task.

Finally, the μ-Λ relationship was further examined. Using twenty-month DSD data collected by two co-located disdrometers, the observations were cross-checked reveal-

ing that reliable μ-Λ relationships can be derived using a single disdrometer, despite large measurement uncertainties. Even though the second-degree polynomial model has been extensively used to represent empirical μ-Λ relationships, its coefficients have not clear interpretation. Basis on the double normalization framework a new power-law model for representing μ-Λ relationships was presented. The new power-law relationship was consistent with other relationships from the literature. Then, an analysis of the μ-Λ relationship in convective and stratiform rainfall in the Netherlands was conducted and potential differences were examined. The derived μ-Λ relations were significantly different from each other highlighting that the relationship is not a statistical artifact but influenced by several factors such as the rainfall type, the DSD model and the moments used to normalize the DSD.

Samenvatting[1] (in Dutch)

Neerslag is een belangrijke input voor veel wetenschappelijke problemen, waaronder hydrologie, numerieke weersvoorspelling en klimaatmodellering. Daarom moet het zorgvuldig worden gecontroleerd en gemeten. Niettemin blijft het meten van regenval een uitdagende taak, vooral vanwege de grote ruimtelijke en temporele variabiliteit. Hoewel in-situ metingen nauwkeurige lokale neerslagwaarnemingen opleveren, ontberen ze een ruimtelijke dekking, wat hun bruikbaarheid op wereldschaal beperkt. Aan de andere kant kunnen weerradars de regenval over veel grotere ruimtelijke domeinen meten, maar hun schattingen worden beïnvloed door hogere niveaus van onzekerheid. Om de nauwkeurigheid van op radar gebaseerde neerslagschattingen te vergroten, moeten de complexe, kleinschalige microfysische eigenschappen van de regen bekend zijn of afgeleid worden. In deze context komt de regendruppelgrootteverdeling (DSD) naar voren als een belangrijke parameter. Net als de neerslagcijfers vertoont de DSD ook aanzienlijke ruimtelijke en temporele variabiliteit, die moeilijk te meten en te modelleren zijn. Dit proefschrift draagt bij aan een beter begrip van de kleinschalige variabiliteit van regenval door verschillende manieren te onderzoeken om de modellering en schatting van DSD's op verschillende schalen te verfijnen.

Het eerste vraagstuk dat wordt onderzocht heeft betrekking op de parametrisering van de DSD in de vorm van een eenvoudige verdeling. In de literatuur zijn verschillende wiskundige modellen voorgesteld om natuurlijk voorkomende DSD's te benaderen, waarbij de gammaverdeling de meest voorkomende is. Er zijn echter maar heel weinig onderzoeken die de geschiktheid van dit model rigoureus hebben gekwantificeerd. Onze eerste bijdrage is de ontwikkeling van een nieuwe methode om de geschiktheid van het gammamodel te kwantificeren, gebaseerd op een combinatie van de Kolmogorov-Smirnov goodness-of-fit-test en Kullback-Leibler-divergentie. Deze nieuwe methode wordt vervolgens toegepast op empirische DSD's gegevens verzameld tijdens een campagne van twee maanden in Nederland. Vervolgens werd de invloed van de temporele bemonsteringsresolutie op de geschiktheid van het gammamodel bestudeerd. De bevindingen tonen aan dat de meerderheid van de DSD's niet perfect gamma zijn, maar goed worden benaderd door het gammamodel bij hoge bemonsteringsresoluties.

Vervolgens wordt een veelgebruikte DSD ophaaltechniek, gebaseerd op polarimetrische radargegevens, onderzocht. Kritische aannames achter de ophaalprocedure worden uitgelicht om potentiële bronnen van fouten en onzekerheden te schetsen. Een belangrijk onderdeel van de ophaalmethode, bekend als de μ-Λ relatie, wordt geanalyseerd en kritisch besproken. In de literatuur worden μ-Λ relaties vaak als vanzelfsprekend beschouwd zonder veel kritische discussie. Studies negeren bijvoorbeeld vaak het feit dat μ-Λ relaties zijn afgeleid van disdrometer gegevens, die een groter bemonsteringsvolume hebben dan de radarmetingen waarop ze worden toegepast. Uit ons onderzoek blijkt dat dit schaalverschil toch geen groot probleem is, omdat μ-Λ relaties opmerkelijk robuust lijken te zijn voor veranderingen in de steekproefomvang, de resolutie van de monsters, de variabiliteit van de neerslag tussen gebeurtenissen en zelfs de geschikt-

---

[1] translated in Dutch by Wouter Paul van Brummelen

heid van het gammamodel. Dit resultaat wordt vervolgens gebruikt om de invloed van kalibratiefouten in radarwaarnemingen te bestuderen, evenals schaalverschillen tussen radar en disdrometer waarnemingen.

In het laatste deel van het proefschrift wordt de μ-Λ relatie verder onderzocht. Met behulp van een dataset van twintig maanden van co-gelokaliseerde DSD metingen laten we zien dat het ondanks de grote meetonzekerheden mogelijk is om betrouwbare μ-Λ relaties af te leiden met behulp van een enkele disdrometer, zonder de noodzaak van co-locatie. Vervolgens analyseren we de afgeleide μ-Λ relaties in convectieve en stratiforme regenval in Nederland om aan te tonen dat verschillende neerslagtypen worden gekenmerkt door verschillende μ-Λ relaties. Ten slotte bespreken we kritisch het gebruik van tweedegraadspolynomen voor het fitten van empirische μ-Λ relaties, zoals gewoonlijk in de literatuur wordt gedaan. Nadat we hebben uitgelegd waarom polynomen ontoereikend zijn, stellen we een nieuw, verbeterd machtswetmodel voor, gebaseerd op het DSD modelleringsraamwerk met dubbele normalisatie. We laten zien dat deze nieuwe machtswetrelatie consistent is met andere relaties uit de literatuur, maar dat de parameters ervan een duidelijke fysieke interpretatie hebben in termen van de onderliggende schaalwet die de verschillende momenten van de DSD met elkaar verbindt.

Chapter 1

Introduction

*Nature uses only the longest
threads to weave her patterns,
so that each small piece of her fabric
reveals the organization of the entire tapestry.*

Richard Feynman

1.1 Motivation

The water cycle, i.e., the continuous transport of water throughout the ecosystem (land, ocean and atmosphere), is a fundamental mechanism in the complex equilibrium of the Earth. It is the process by which water evaporates from the surface, rises into the atmosphere, and condenses to form clouds. These clouds then produce precipitation (liquid and solid), which falls back to the surface of the Earth. The water that falls onto the land can either evaporate, flow into rivers and streams, or seep into the ground to become groundwater. This water eventually makes its way back to the ocean, where the process starts all over again. The water cycle is an essential component of Earth's natural systems, playing a crucial role in regulating the distribution and availability of water for all living organisms. Any alteration to the delicate balance of the water cycle could have significant implications for the planet's ecosystem.

Precipitation is a governing process of the global water cycle. According to the latest IPCC report (Caretta *et al.*, 2022), the climate crisis has led to more frequent heavy precipitation events which are expected to continue increasing in intensity separated by more prolonged dry spells. The increase in extremes over the next decades is expected to impact water supplies, natural ecosystems, global economy, human health, transportation, agriculture and national security in a profound way. Every year, extreme precipitation events cause floods and droughts, which cost innumerable human lives and billions of dollars in damages (Ralph *et al.*, 2014).

In this context, a continuous and reliable monitoring of precipitation at global scale

is of paramount importance for a range of societal and scientific issues such as weather forecasting, hydrology and management of fresh water resources. However, accurately estimating precipitation, its type and intensity at planetary scale remains a challenging task. Global scale monitoring of precipitation heavily relies on remote sensing techniques such as weather radars (ground-based or spaceborne). Unlike rain gauges, radars do not directly provide the quantity of interest (i.e., the rainfall amount or rainfall intensity). A weather radar only provides the backscattered signal of raindrops from which rainfall intensities must be inferred. One of the key quantities that is needed to perform this conversion is the so-called drop size distribution (DSD). The DSD is a statistical summary of the size and number density of rain droplets in a unit volume of air. Studies have shown that similarly to rainfall rates, the DSD can be highly variable in time and space (Berne *et al.*, 2012; Uijlenhoet *et al.*, 2003). This natural variability within and between storms greatly affects the accuracy of rainfall retrievals from remote sensing sensors.

The main objective of this thesis is to contribute to the improvement of quantitative precipitation estimation (QPE) through a better understanding of the small-scale variability of rainfall. More specifically, our goal is to enhance the scientific understanding of how to model and estimate raindrop size distributions across different scales. This requires a comprehensive understanding of precipitation microphysics and small-scale dynamics.

1.2 Rainfall microphysics

Precipitation is a dynamically interacting system of complex microphysical processes (McFarquhar, 2022; Michaelides *et al.*, 2009) starting from the formation of raindrops inside the cloud (e.g., nucleation, condensation, collision-coalescence) until the later stages when the drops exit the cloud (e.g., evaporation, breakup). Because of the chaotic nature of the involved microphysical processes, precipitation remains notoriously challenging to analyze, measure and predict (Figure 1.1a).

The initial step in precipitation formation is the lift of an air parcel. Rising motion in the atmosphere can be triggered by several factors such as a passing front, a mountain, convergence or convection. As the air rises, it cools due to adiabatic expansion. When the temperature falls below the dew-point, saturation is reached and the cloud formation starts (i.e., water vapour condenses to form cloud droplets). A necessary element for cloud formation is the presence of aerosols (Barthlott *et al.*, 2022). These are micrometer-sized particles such as salt, dust or air pollutants which serve as condensation nuclei for water vapor. Once condensation is initiated, cloud particles continue to grow turning into water droplets. Cloud droplets gradually increase in size through collision and coalescence processes as they float. When they become too heavy to be maintained aloft, they start to fall. During their descent, they continue to collide with other drops, forming larger ones that may break up into smaller ones when they become too large. Other factors which limit the size growth of raindrops are the evaporation and the breakup due to strong wind gusts or turbulence (Hu and Srivastava, 1995). All these processes happening in the air (aloft) govern the DSD, which can be observed on the ground.
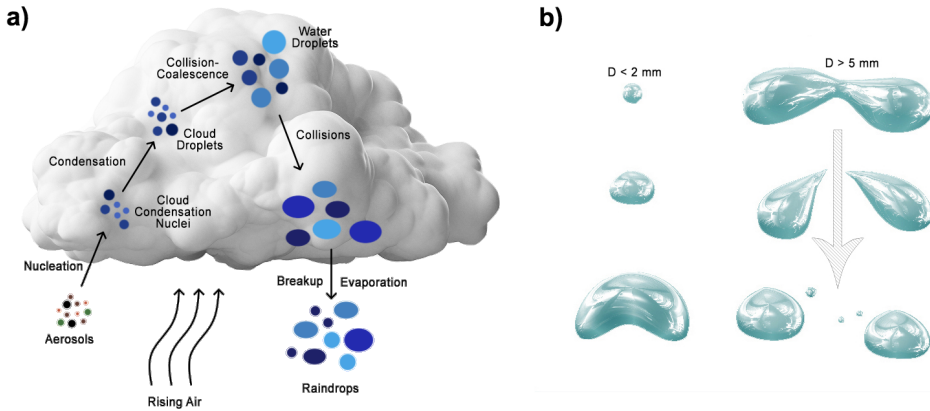
Figure 1.1: A schematic representation of a) the microphysical processes in liquid-phase cloud b) the shape of raindrops depending upon their size.

It is worth mentioning that the rainfall formation mechanism described above is called "warm rain". There is also the "cold rain" formation process which involves ice particles and the presence of supercooled liquid water through the Bergeron-Findeisen-Wegener process (Findeisen *et al.*, 2015). A more detailed description of both mechanisms and all the individual steps involved in the formation of precipitation can be found in McFarquhar (2022).

Apart from the microphysical processes affecting rain droplets inside and outside the cloud, there are few other important drop characteristics which are worth mentioning as well: the drop shape, the drop oscillation, and the canting angle of raindrops. At the early stage of a raindrop's life, drop shape is approximately spherical (Figure 1.1b). However, as a drop grows bigger, its shape also becomes more complicated due to a constant tug-of-war between counteracting forces. According to Gorgucci *et al.* (2006), the surface tension, hydrostatic pressure, aerodynamic forces, internal circulation and electric stress are the main forces influencing the size and shape of raindrops. For small raindrops less than 2 millimeter in size, the spherical shape is retained because of surface tension. As raindrops grow in size, surface tension becomes insufficient to hold the water molecules together and the shape changes from spherical to an oblate spheroid. At the same time, as the size increases, the fall velocity of the drop also increases, causing unequal pressure over its surface (Gorgucci *et al.*, 2006). The increasing pressure at the bottom of the drop overcomes the surface tension while the decreasing pressure at the top is not enough to overcome it, making the drop keep its rounded shape on the sides and the top. This mechanism deforms the raindrop by flattening the bottom surface and spreading the shape sideways. Drops that are 2 to 3 mm in size are big and heavy enough to be affected by air pushing against them as they fall (Pruppacher and Beard, 1970). In nature, the observed drops can reach several thousands per cubic meter, with the majority having diameters between 0.1 and 3 mm. When the diameter grows larger than 4.5 mm, drop becomes increasingly distorted and unstable until they burst, producing a fine spray of smaller droplets (Villermaux and Bossa, 2009). Because raindrop shapes depend on drop

size (spherical, oblate spheroid), it is common practice to express drop sizes through the equivolumetric spherical diameter, i.e., the diameter of a sphere that contains the same amount of water as the considered drop (Andsager *et al.*, 1999).

Another aspect of raindrops which should be taken in account is their oscillation. Several field observations and laboratory studies have shown that a rain particle falling from the sky may exhibit oscillations (Beard and Kubesh, 1991; Chandrasekar *et al.*, 1988; Pruppacher and Beard, 1970; Tokay *et al.*, 2000). According to Beard and Kubesh (1991) the oscillation of raindrops can be distinguished into three different modes: i) the axisymmetric mode with oscillations between oblate and prolate shapes, ii) the transverse mode with side-to-side perpendicular to each other movements, and iii) the horizontal mode with oscillations in the horizontal plane.

As rain particles travel through the atmosphere, they also tend to rotate/tilt due to horizontal wind variations with height and the relative airflow around droplets (Brussaard, 1974). The canting angles, combined with the oscillations, varying sizes, shapes, velocities, and positions of raindrops, contribute to making rainfall an extremely complex process of dynamically interacting particles. Since it is often impossible to measure and keep track of all these details, simplified models of rainfall have been built that summarize small-scale properties and dynamics with the help of statistics (such as the DSD).

1.3 The drop size distribution (DSD)

The DSD, denoted by $N(D)$ [mm^{-1} m^{-3}], is a statistical description of the microstructure of rainfall that expresses the number of raindrops per cubic meter as a function of their respective equivolume diameter D. In Figure 1.2 a schematic illustration of rainfall microstructure is presented. The DSD is defined as the product of the total concentration of the drops (N_T) [m^{-3}] and a probability density function $f(D)$:

$$N(D) = N_T f(D). \tag{1.1}$$

Knowledge of the DSD in a given air volume is crucial for the quantitative analysis of cloud and precipitation processes. DSDs also play a key role in remote sensing techniques (Bringi and Chandrasekar, 2001; Marshall and Palmer, 1948), where they are
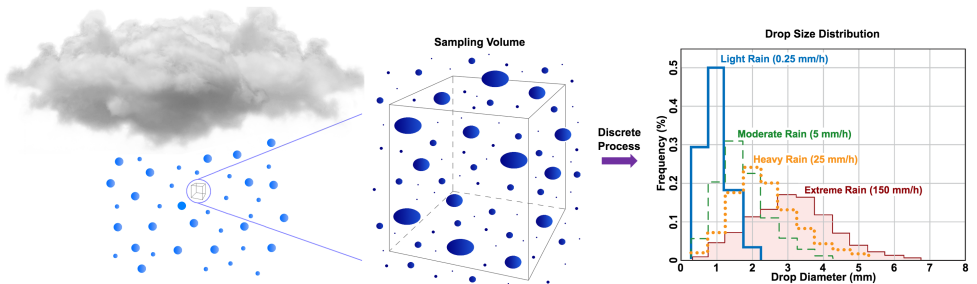
Figure 1.2: Visual illustration of rainfall microstructure in a sample volume and typical distributions of raindrop sizes during different rain rates.

needed to calculate the interactions between hydrometeors and the electromagnetic waves due to scattering and absorption. Most rainfall related variables, such as the rainfall intensity, liquid water content or kinetic energy, can be written as a combination of weighted moments of the DSD. The nth moment of the DSD is defined as:

$$M_n = \int_{D_{min}}^{D_{max}} D^n N(D) dD,$$ (1.2)

where the integration limits are assumed to be D_{min} and D_{max} due to the finite range of drop sizes which can occur in nature (Vivekanandan *et al.*, 2004). The number concentration is the 0th moment of the DSD and it can be expressed as:

$$N_T = \int_{D_{min}}^{D_{max}} N(D) dD = M_0.$$ (1.3)

Both the concentration of raindrops and the probability density function exhibit significant variability in space and time (Torres *et al.*, 1998). Depending on the specific application, either one of these factors can be more important. However, in many cases, a comprehensive understanding of rainfall microstructure requires consideration of both factors. For example high (low) drop concentrations are not always associated with high (low) rain rates. A good example of this are drizzle events, during which a large concentration of relatively small droplets can be can be observed.

An important quantity for distinguishing rainfall types is the mass-weighted mean drop diameter (D_m) [mm], defined as the ratio of the 4th to the 3rd DSD moments:

$$D_m = \frac{\displaystyle\int_{D_{min}}^{D_{max}} N(D) D^4 dD}{\displaystyle\int_{D_{min}}^{D_{max}} N(D) D^3 dD} = \frac{M_4}{M_3}.$$ (1.4)

Depending on the application, other characteristic drop sizes can be used as well, such as the median-volume drop diameter (D_0) [mm], which represents the diameter that divides the DSD sizes into two equal parts of water volume, or the mean drop diameter (D_{mean}) [mm], which is the ratio of the 1st and the 0th DSD moments. D_0, D_{mean} and D_m are similar variables and closely linked to each other. However, for remote sensing applications, D_0 and D_m are preferred because they put more emphasis on larger raindrops (compared to D_{mean}). The median-volume drop diameter (D_0) is defined as:

$$\frac{\pi \rho_w}{6} \int_{D_{min}}^{D_0} D^3 N(D) dD = \frac{\pi \rho_w}{6} \int_{D_0}^{D_{max}} D^3 N(D) dD = \frac{1}{2} LWC,$$ (1.5)

where ρ_w is the density of the water [10^{-3} g mm^{-3}] and LWC is the liquid water content

[g m^{-3}] given by:

$$LWC = \frac{\pi \rho_w}{6} \int_{D_{min}}^{D_{max}} N(D)D^3 dD = \frac{\pi \rho_w}{6} M_3. \tag{1.6}$$

Another essential quantity for quantitative precipitation estimation is the terminal fall velocity $v(D)$ [m s^{-1}] of a raindrop of equivolume spherical diameter D (Beard, 1976; Beard, 1985). According to Atlas *et al.* (1973), $v(D)$ can be approximated reasonably well by a power-law of the form:

$$v(D) = \kappa D^v, \tag{1.7}$$

where κ [m^{1-v} s^{-1}] and v [-] are positive coefficients. The most commonly used values for standard conditions of pressure and temperature are $\kappa = 3.778$ and $v = 0.67$ (Atlas and Ulbrich, 1977). Using the raindrop fall velocity model above, we can calculate the rain rate (R) [mm h^{-1}] as the flux of water arriving at the surface over a period of time:

$$R = 6\pi 10^{-4} \int_{D_{min}}^{D_{max}} D^3 v(D)N(D)dD. \tag{1.8}$$

If the raindrop fall velocity is approximated by Equation 1.7 with $\kappa = 3.778$ and $v = 0.67$, then $R \approx M_{3.67}$. In other words, the rain rate is roughly proportional to the 3.67th order moment of the DSD. The rain rate is an essential parameter of interest for hydrologists, especially for rainfall related studies and rainfall monitoring in a macroscopic level.

1.4 Measurement of the DSD

Sensors for measuring DSDs are called disdrometers. Several types of disdrometers exist: impact disdrometers (e.g., Joss-Waldvogel disdrometer, Joss and Waldvogel, 1967), measure the forces produced by impacting raindrops. The two-dimensional video-disdrometer (2DVD) captures high-resolution images of falling particles at two different heights to determine their speed, shapes, and sizes (Schönhuber *et al.*, 2008). Optical disdrometers measure the size and velocity of particles that fall through a horizontal laser beam. The fall velocity of the particles is estimated from the time it takes for the laser beam power to return to its default power. The working principle and main limitations of this sensor have already been well documented (Raupach and Berne, 2015; Tokay *et al.*, 2014). The main issues are the discretization of the data (drop-size classes), the limited sampling area and the underestimation of small-size particles.

DSD observations taken by disdrometers provide point measurements of rainfall characteristics over specific time intervals, with a small sampling area. By contrast, weather radar tends to have much larger resolution volumes in the order of hundreds of meters up to several kilometers. Unlike disdrometers, weather radars cannot directly measure DSDs. They only provide information about selected moments of the DSD, which latter can be used to indirectly estimate DSDs. However, the accuracy of such retrievals depends on many factors, such as sensor calibration, incidence angle, resolution volume and assumptions made about the shape of the DSD during the retrieval process. Even for

a perfectly calibrated radar, DSD estimates may still differ substantially from measurements made on the ground due to vertical variations in the fall velocities of raindrops, updrafts/downdrafts, collision and coalescence processes. The difference in scale between radar and disdrometer measurement may also play a big role. Many DSD-related quantities such as the number concentration, mean drop size, reflectivity and rain rate have been found to depend on the scale at which they are measured. A good understanding of these scale issues and how they might impact the accuracy of DSD retrievals is a recurrent theme in this thesis.

1.5 Parametric DSD models

In the literature several parametric DSD models have been proposed. One of the earliest and most popular is the exponential distribution introduced by Marshall and Palmer (1948):

$$N(D) = N_0 e^{-\Lambda D}. \tag{1.9}$$

The exponential model is a good choice for representing DSDs that are integrated over time. The original model proposed by Marshall and Palmer (1948) is a particular case of Equation 1.9, with a fixed concentration parameter $N_0 = 8000$ [mm^{-1} m^{-3}] and only one free parameter, the slope Λ [mm^{-1}]. However, nowadays, the most accepted and used model in the literature is the gamma (Ulbrich, 1983; Willis, 1984):

$$N(D) = N_0 D^\mu e^{-\Lambda D}, \tag{1.10}$$

where μ is the shape parameter [-] and N_0 is an intercept parameter [mm$^{-1-\mu}$ m^{-3}] whose units depend on μ. When $\mu = 0$, the gamma model (Equation 1.10) reduces to the exponential form (Equation 1.9). Other common parametric models are the lognormal (Feingold and Levin, 1986) and Weibull (Jiang *et al.*, 1997). Figure 1.3 show example
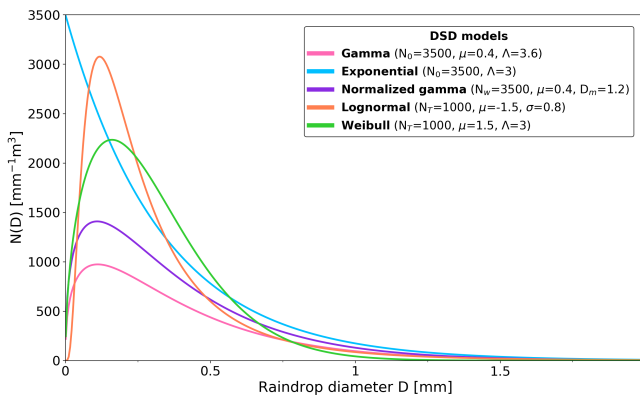

Figure 1.3: Illustration of several conventional DSD models (gamma, exponential, normalized gamma, lognormal, Weibull).

1

shapes of widely used DSD models in the literature. Moreover, it should be pointed out that other studies recommend the use of more complicated models with more parameters (e.g., Johnson SB; Cugerone and De Michele, 2015). While interestingly, DSD models with four or more parameters are not very practical in the context of remote sensing, since it is often impossible to accurately estimate that many independent parameters from weather radar measurements.

Because the gamma model is so prevalent in literature and gamma DSDs play a key role in remote sensing applications, researchers often take this model for granted. This can be problematic, especially when working with DSD data from different sensors and across vastly different spatial and temporal scales. Most of the studies which focused on assessing the adequacy of the gamma DSD model concluded that the gamma provides a better fit than other simple distributions while remaining simple and flexible (Adirosi et al., 2016; Johnson et al., 2015). Adirosi et al. (2016) fitted three conventional distributions, lognormal, gamma and Weibull and investigated the adequacy of them against real observations, using the Kolmogorov–Smirnov goodness of fit test. They showed that the gamma model has the lowest rejection rate, while the Weibull is rejected most frequently. Ekerete et al. (2015) used the chi-square (χ^2) goodness of fit to conclude that gamma and lognormal distributions are not fully adequate, pointing out that empirical DSDs appear to be somewhere between bimodal and gamma shape. They suggested that a Gaussian mixture model with three centers fits better. Cugerone and De Michele (2015) used the Kolmogorov–Smirnov goodness of fit and skewness-kurtosis diagrams to show that gamma and lognormal models are not fully adequate from a statistical point of view and that a Johnson SB distribution should be considered as an alternative choice.

Another important topic of research in the field of DSD modeling revolves around the idea of normalization. Normalization is a useful technique to compare the shapes of DSDs with different moments or characteristic drop diameters. Over the years, different DSD normalization techniques have been proposed (Testud et al., 2001; Torres et al., 1994). In this thesis, the normalized gamma distribution with two reference moments (i.e., D_m and LWC) proposed by Testud et al. (2001) and Bringi et al. (2003) is used:

$$N(D) = N_w f(\mu) \left(\frac{D}{D_m} \right)^\mu e^{-(4+\mu)\frac{D}{D_m}}, \tag{1.11}$$

where N_w is the generalized intercept parameter given by:

$$N_w = \frac{4^4}{\pi \rho_w} \left(\frac{LWC}{D_m^4} \right). \tag{1.12}$$

In contrast to N_0 (see Equation 1.10), now the N_w does not depend on μ [mm^{-1} m^{-3}]. Both D_m and N_w (through LWC, see Equation 1.12) are key physical quantities with clear physical meaning, easier to interpret. A lot of work has gone into the conceptualization of single- and double-moment normalization models, that are better at capturing the natural DSD variability and provide better fits to empirical DSD spectra (Lee et al., 2004). For example, the generalized gamma model, as indicated by several studies (Maur, 2001; Thurai and Bringi, 2018), offers greater flexibility than the standard gamma distribution, making it more effective at describing naturally occurring DSDs. The Equation 1.11 is frequently used in atmospheric remote sensing related applications such as

the ground-based weather radars or the spaceborne-radars (e.g., the precipitation re-
trieval algorithm from GPM Dual-Frequency Radar, Tokay *et al.*, 2020). In this thesis,
a new method for rigorously and automatically testing the adequacy of the normalized
gamma DSD model across different temporal scales is proposed.

1.6 QPE using weather radars

Weather RADAR which stands for RAdio Detection And Ranging is an advanced system
used for monitoring (Atlas and Ulbrich, 1990; Bringi and Chandrasekar, 2001) and study-
ing the location, intensity, movement, and type of precipitation (rain, snow, hail etc.).
However, initially when it was first introduced in 1940s, radar had a different use. The
main objective of these systems was to detect ships and airplanes during World War
II. Luckily, apart from the metallic targets, radar operators noticed some "unwanted"
noise due to precipitation and the concept of the weather radar was born. Since then
weather radar has evolved to become an essential tool in meteorology, aviation, emer-
gency management, and various other sectors that rely on the accurate, real-time mon-
itoring of weather. The ability to detect and track severe weather phenomena such as
thunderstorms and hurricanes at high spatial and temporal resolutions over large do-
mains means that weather radar plays a crucial role in nowcasting (Foresti *et al.*, 2019;
Imhoff *et al.*, 2020).

Unlike rain gauges which provide direct, point rain observations, remote sensing sen-
sors like radars indirectly measure rainfall with better spacial coverage but with higher
observation uncertainty. A weather radar emits an electromagnetic wave into the at-
mosphere and analyzes the signal that is returned (i.e., the backscatter). Typically, the
interesting part is the fraction of the transmitted signal that is reflected back as a result
of scattering by precipitation particles. The average returned power to the radar (P_r)
[W] after interacting with the individual particles in the scanned radar volume is given
by (Battan, 1973):

$$\overline{P_r} = \frac{P_t G^2 \lambda^2}{(4\pi)^3 r^4} \sum_{i=1}^{n} \sigma_{b,i},$$ (1.13)

where P_t is the transmitted power [W], G is the antenna gain [-], λ is the wavelength of
the radar [m], r is the range of the objects in meters and $\sigma_{b,i}$ [m^2] are the backscatter
cross-sections for each particle. The volume containing those particles is called radar
resolution volume, and is determined by the pulse length, the beamwidth and the dis-
tance of the target. It is worth mentioning that the radar beam is not strictly uniform
over the volume. The radar energy is strongest in the center of the volume, and weaker
toward the edges. Assuming a Gaussian shape for the beam pattern, the effective volume
of the radar beam is given by:

$$V = \frac{\pi}{2\ln(2)} \left(\frac{r\theta}{2} \right)^2 \frac{h}{2},$$ (1.14)

where h represents the pulse length [m] and θ is the antenna beamwidth [degrees]. Fur-
thermore, under the assumption that the particles are spherical raindrops with sizes
smaller than the radar's wavelength (Rayleigh scattering), σ_b is proportional to the sixth

1

power of the drop diameter D [mm]. Using this and Equation 1.14 to Equation 1.13 gives:

$$\overline{P_r} = \frac{\pi^3}{1024\ln(2)} \left(\frac{P_t G^2 \theta^2 h}{\lambda^2} \right) \left(\frac{|K_w|^2}{r^2} \sum_{1\,m^3} D^6 \right),$$
(1.15)

where $|K_w|$ [-] is the dielectric factor of water (≈ 0.93). Thus, for a collection of spherical small raindrops, the mean received power is determined by radar parameters, range, and by two factors of the target: the value of $|K_w|$ and $\sum D^6$. The last factor is so important that a separate quantity, called the equivalent reflectivity factor (Z), is introduced for it:

$$Z = \sum_{1\,m^3} D^6 = \int_{D_{min}}^{D_{max}} D^6 N(D) dD = M_6,$$
(1.16)

where Z is expressed in $mm^6\ m^{-3}$, $\sum$ denotes a summation over the unit volume [1 m^3] and $N(D)$ is the DSD. Due to its large range of variation, the reflectivity is often expressed in logarithmic scale [dBZ, $10\log_{10}$]. Using Equation 1.16 in Equation 1.15, we get the weather radar equation:

$$\overline{P_r} = \frac{C|K_w|^2}{r^2} Z,$$
(1.17)

where the variable C replaces all the radar-related variables from Equation 1.15 with $C = \frac{\pi^3 10^{-18} P_t G^2 \theta^2 h}{1024\ln(2)\lambda^2}$ and 10^{-18} being added to get the desired unit for Z [$mm^6\ m^{-3}$]. At this point, it is worth mentioning that Equation 1.17 and Equation 1.16 are valid under three main assumptions: 1) there is no attenuation (i.e., no loss of power), 2) the radar resolution volume is uniformly filled with precipitation particles and 3) we are in the Rayleigh scattering regime (i.e., raindrops are much smaller than the wavelength of the radar).

Unlike the returned power, the radar reflectivity factor is independent of sensor characteristics and solely depends on the characteristics of hydrometeors. This is why reflectivity is preferred over power. Indeed, comparing the returned power signals from two sensors directly, even if they measure the same volume, would be highly impractical since they may differ substantially due to hardware differences between radar systems.

From Equation 1.16 it is evident that both the number and size of raindrops per cubic meter contribute to the value of the radar reflectivity factor. However, due to the dependence on D^6, the reflectivity exhibits much greater sensitivity to the presence of large raindrops compared to smaller ones. For example, one can show that a single raindrop of diameter D gives exactly the same reflectivity as 64 half-sized raindrops of diameter $\frac{D}{2}$, even though the liquid water content (3rd order moment of the DSD) corresponding to the 64 drops is 8 times larger than the LWC of the one large drop.

Radar is an invaluable tool for monitoring rainfall. But when it comes to accurately estimating rainfall, radar suffers from a fundamental limitation: reflectivity measurements first need to be converted to rainfall rates. In order to perform this transformation, detailed knowledge about the DSD is required. For many years, scientists have tried to circumvent this dependence on DSD by proposing different empirical relationships between reflectivity and rain rate. The most popular approach is the famous Z-R power-law model:

$$Z = aR^b,$$
(1.18)

where Z is expressed in mm^6 m^{-3}, R in mm h^{-1} and a [mm^{6-b} m^{-3} h^b] and b [-] are two empirical constants. Unfortunately, there is no single relation that can satisfy all meteorological phenomena under which Equation 1.18 is valid. Values for the prefactor typically range from 200 to 600 and 1.5 to 2 for the exponent. The combination $a = 200$ and $b = 1.6$ leads to the well known Marshall–Palmer relation for stratiform precipitation (Marshall *et al.*, 1955).

The key factor governing the values of a and b in the Z-R power-law is the DSD (Marshall and Palmer, 1948; Uijlenhoet, 2001). Since DSDs are highly variable in time and space, this variability has a major impact on the uncertainty affecting rainfall estimates from weather radar. According to Lee and Zawadzki (2005), the variability of the DSD alone can cause uncertainties in rainfall rates in the order of 40%. This is on top of all the other measurement uncertainties and illustrates why quantitative precipitation estimation (QPE) using radar is such a difficult task.

In the recent decades significant progress has been made to reduce uncertainties in precipitation estimation by taking advantage of the full potential of polarimetric radars. A dual-polarization radar transmits and receives electromagnetic waves in both vertical and horizontal polarization. The returned signals at perpendicular polarization provide additional information about the horizontal and vertical dimensions of targets, which can be used to estimate the average size, shape, and type of precipitation particles in the radar volume. The shape of raindrop is a key factor for the characteristics of polarimetric measurements since the oblateness of the raindrops accounts for the different scattering properties between horizontal and vertical polarization (Gorgucci and Baldini, 2009; Thurai *et al.*, 2007). A key polarimetric parameter is the differential reflectivity (Z_{dr}) [dB] which is obtained by taking the logarithm of the ratio between horizontally polarized reflectivity (Z_h) and vertically polarized reflectivity (Z_v). Positive Z_{dr} values indicate that the dominant hydrometeors have larger sizes in the horizontal dimension, while negative values that hydrometeors are larger in the vertical dimension. Values close to zero suggest that the hydrometeors have similar sizes in both vertical and horizontal dimensions such as the small spherical droplets. Utilizing Z_{dr} along with Z can provide information about raindrop sizes through their shape, which can lead to better rainfall estimation algorithms than with Z alone. For example, a $R(Z, Z_{dr})$ relation can be used:

$$R = cZ^d Z_{dr}^e, \tag{1.19}$$

where c [mm^{1-6d} m^{3d} h^{-1}], d [-] and e [-] are empirical constants. According to Brandes *et al.* (2002) and Ryzhkov *et al.* (2005), a relation with a combination of Z and Z_{dr} is less sensitive to variations in DSD and leads to better quantitative precipitation estimation.

Another polarimetric variable is the co-polar correlation coefficient (ρ_{co}) [-] which measures the degree of correlation between horizontal and vertical polarizations of the received signals. This coefficient decreases from a maximum value of 1 as the raindrop oblateness distribution widens. ρ_{co} is a very useful quantity for identifying the melting layer or distinguishing meteorological from non-meteorological targets. Other polarimetric parameters are the specific differential phase (K_{dp}) [deg km^{-1}], linear depolarization ratio (L_{dr}) [dB] and differential phase shift (Φ_{dp}) [deg] however, they will not be discussed in detail because they are not directly relevant to this thesis.

1.7 DSD retrievals using weather radars

As explained in the previous section, DSDs play a key role in radar-rainfall estimation. Consequently, a lot of efforts have been devoted to retrieving DSDs from various types of remote sensing measurements. Such retrievals provide valuable insight into the microphysical properties of rainfall, which is essential for remote sensing, numerical weather prediction (NWP), hydrological modeling and climate studies (Bringi and Chandrasekar, 2001; Michaelides *et al.*, 2009). One way to retrieve DSDs from weather radar observations is to exploit the dual-polarization capabilities of modern radars, by analyzing the backscattered signals from precipitation particles at horizontal and vertical polarizations. Retrieval algorithms often involve complex mathematical models and require to take into account factors such as signal attenuation due to heavy precipitation, instrumental limitations, clutter, calibration issues and the high temporal and spatial variability of the DSD.

Usually a parametric DSD model is used to represent the DSD in the radar volume. The complexity of the DSD model (i.e., the number of the unknown parameters) depends on radar characteristic and the number of available observations. Often, only two or three parameters are realistic. If the number of independent radar measurements is less than the number of DSD parameters, the degrees of freedom in the DSD model should be reduced. This can be achieved either by fixing the value of one of the DSD parameters (e.g., the GPM DSD retrieval algorithm assumes that μ has a fixed value equals to 3, Tokay *et al.*, 2020) or by using an empirical relationship between two of the DSD parameters, such as the well known μ-Λ relationship.

The most common DSD retrieval technique is based on the gamma DSD model, two observables from a polarimetric weather radar (Z_h and Z_{dr}) and an empirical relationship between μ and Λ. The retrieval method has been described in detail by Zhang *et al.* (2001). Even though the μ-Λ relationship is an important element for the retrieval process, little is known about how stable it is. The relationship is often taken for granted with no critical discussion, neglecting the potential effect of various factors such as the sampling resolution or the the validity of the gamma assumption. Moreover, another important aspect which tends to be overlooked is differences between sensors (e.g., radars, disdrometers) due to scale. For example little is known about the scale-related bias affecting retrieved DSDs from weather radar when a μ-Λ relationship derived from disdrometer data (which have much smaller sampling volume) is used.

1.8 μ-Λ relationship

As mentioned in the previous section, the most common method to retrieve DSDs from a dual-polarization radar requires two radar observables Z_h, Z_{dr} and a constrained relationship between two of the gamma DSD parameters, e.g., Ulbrich (1983) proposed a relation between N_0 and μ. Nowadays, the most widely accepted empirical relation is between μ and Λ. So far, several deterministic functions linking μ and Λ have been proposed in the literature with the most popular being the second-order polynomial model.

The first relationships were proposed by Zhang *et al.* (2001) and Zhang *et al.* (2003):

$$\mu = -0.016\Lambda^2 + 1.213\Lambda - 1.957 \qquad \text{and} \qquad \Lambda = 0.0365\mu^2 + 0.735\mu + 1.935 \qquad (1.20)$$

respectively, using DSD observations from Florida. The μ-Λ relationship shows variability across different climatological regimes, types of rain (convective or stratiform), regions or even seasons (Chen *et al.*, 2016; Gatidis *et al.*, 2024; Seela *et al.*, 2018). According to Zhang *et al.* (2001) regardless of the above factors, the DSD parameters are governed by the following rule: large (small) μ corresponds to small (large) D_m, narrow (broad) distribution and large (small) Λ, keeping in mind that large values of μ are linked to low rain intensity (rain rate less than 5 mm h^{-1}).

It is worth mentioning that even though initially the μ-Λ relationship was conceptualized because remote sensing measurements were not sufficient to fully estimate all parameters of the DSD, there are several studies questioning whether there is any real physical meaning behind such a relation. For example Chandrasekar and Bringi (1987) and Moisseev and Chandrasekar (2007) claim that the relation is a statistical artifact caused by the fact that the quantities are derived from the same DSD measurements. On the other hand, other authors (Seifert, 2005; Zhang *et al.*, 2003) suggested that the μ-Λ relationship is more than a statistical artifact. According to Seifert (2005) there is a physical correlation between the two DSD parameters which links the width of the distribution to its mean value, especially in strong convection. However, they suggested to use the standard deviation of the drop mass distribution (σ_m) and the median volume diameter (D_0) which have more physical meaning than μ and Λ and are independent of the validity of the gamma model.

Another important aspect of the μ-Λ relation which was never questioned, is the chosen model for the relationship. Even though in the literature there is a long list of different μ-Λ relationships based on different characteristics such as the rainfall regime, rain rate intensity and seasonal/regional criteria (Chen *et al.*, 2016; Seela *et al.*, 2018), all of them fit the same second-order polynomial model to the data (e.g., see Equations 1.20). A parabolic curve can effectively approximate empirical μ-Λ relationships. However, the model coefficients lack a clear physical interpretation, and there is no theoretical justification for the parametric form of the model.

1.9 Overview of this thesis

The objective of this thesis is to enhance our understanding of the small-scale variability of rainfall by specifically focusing on the critical rainfall quantity: the drop size distribution. This includes a detailed investigation of the adequacy of the gamma DSD model, the assumptions behind the DSD retrieval algorithms from weather radars, the use of μ-Λ relationships and the effect of scale differences to the DSD estimation. The thesis is organized in 5 chapters, including the current one that serves as an introduction and Chapter 5 which provides the conclusions and outlook of the thesis. The thesis is a compilation of three published manuscripts from peer-reviewed journals, each presented in Chapters 2, 3 and 4, respectively. More details about the structure of the thesis and the topic of each of these chapters is provided in the following paragraphs.

Chapter 2 _____

A fundamental quantity to sufficiently describe the microstructure of rainfall is the DSD. The most common model in the literature to approximate naturally occurring DSDs is gamma distribution, even though it is generally accepted that it is imperfect. In this chapter a precise quantification of the gamma DSD model adequacy was examined. Based on a two-month dataset from a Parsivel disdrometer in the Netherlands, gamma distributions were fitted and μ-Λ pairs were derived. The adequacy of the gamma model was analyzed using a combination of Kolmogorov–Smirnov goodness-of-fit test and Kullback–Leibler divergence. The key questions addressed in Chapter 2 are as follows.

Key Question I: *How adequate is the gamma model for representing DSDs?*

Key Question II: *How sampling resolution can affect the adequacy of the gamma model?*

Chapter 3 _____

A common technique for DSD retrievals from polarimetric radar data is based on two radar observables (Z_h and Z_{dr}) and a constrained relationship between μ and Λ. However, radar data is likely to contain systematic errors while at the same time μ-Λ relationships are frequently taken for granted without any critical thought. In this chapter, we utilized observations from a radar and a nearby disdrometer to study several events of light to moderate stratiform rain in the Netherlands. Initially the robustness of μ-Λ relationship to sampling resolution, sample size, adequacy of the gamma model and event-by-event variability was examined. Later the sensitivity of the retrieval algorithm to errors linked to the radar measurements and their effect on the DSD retrievals was investigated and presented. The main questions answered in Chapter 3 are the following.

Key Question III: *How much factors like sampling resolution, sample size, gamma model validity and inter-event variability influence μ-Λ relationship?*

Key Question IV: *Considering DSD retrieval algorithms are sensitive to errors in radar measurements, how easy is to determine the source of the error and make a correction?*

Chapter 4 _____

In this section twenty-month DSD data from two co-located disdrometers in the Netherlands was used. Initially, we introduced a new power-law model based on the double normalization framework to represent μ-Λ relationships. Then taking advantage of the two disdrometers next to each other, we applied a quality control filter based on the mass-weighted mean drop diameter (D_m) and liquid water content (LWC). Finally, an analysis of μ-Λ relationships in convective and stratiform rainfall was conducted and potential differences were examined. The key questions addressed in Chapter 4 are as follows.

Key Question V: *Given that a second-order polynomial function can sufficiently represent empirical μ-Λ relationships, is it possible to use another model with better theoretical justification whose coefficients have clearer physical interpretations?*

Key Question VI: *Are there differences in μ-Λ relationships between convective and stratiform rainfall?*

1

Chapter 2

Evaluation of the gamma DSD model

The adequacy of the gamma model to describe the variability of raindrop size distributions (DSD) is studied using observations from an optical disdrometer. Model adequacy is checked using a combination of Kolmogorov-Smirnov goodness-of-fit test and Kullback-Leibler divergence and the sensitivity of the results to the sampling resolution is investigated. A new adaptive DSD sampling technique capable of determining the highest possible temporal sampling resolution at which the gamma model provides an adequate representation of sampled DSDs is proposed. The results show that most DSDs at 30 s are not strictly distributed according to a gamma model, while at the same time they are not far away from it either. According to the adaptive DSD sampling algorithm, the gamma model proves to be an adequate choice for the majority (85.81%) of the DSD spectra at resolutions up to 300 s. At the same time, it also reveals a considerable number of DSD spectra (5.55%) that do not follow a gamma distribution at any resolution (up to 1800 s). These are attributed to transitional periods during which the DSD is not stationary and exhibits a bimodal shape that cannot be modeled by a gamma distribution. The proposed resampling procedure is capable of automatically identifying and flagging these periods, providing new valuable quality control mechanisms for DSD retrievals in disdrometers and weather radars.

2.1 Introduction

Continuous and reliable precipitation monitoring is of fundamental importance for understanding the water cycle. Every year, extreme precipitation events cause floods and trigger landslides, which cost many human lives and billions of dollars (Ralph *et al.*, 2014). However, obtaining accurate precipitation measurements can be extremely challenging due to the high underlying variability of the meteorological phenomenon in space and time (Jameson and Kostinski, 2001; Uijlenhoet *et al.*, 2003).

One fundamental quantity needed to understand rainfall variability is the raindrop size distribution (DSD). The DSD is considered to be the key source of uncertainty in quantitative precipitation estimations (QPE), affecting rain rate estimates from ground-based radars and satellites. Several studies have shown that QPE can be significantly improved using accurate DSD observations (Rose and Chandrasekar, 2006) but is difficult in practice as natural DSDs rapidly vary in space and time and exhibit a wide range of shapes. For radar and satellite related applications, where a limited amount of information is available, it is often necessary to parameterize the DSD in the form of a simple distribution.

Several mathematical models have been proposed to approximate naturally occurring DSDs (Bringi *et al.*, 2003; Marshall and Palmer, 1948; Testud *et al.*, 2001; Ulbrich, 1983; Zhang *et al.*, 2001). The most popular and widely accepted of them in the remote sensing community is the gamma distribution. However, the gamma distribution is not a perfect model and several studies have questioned its adequacy (Cugerone and De Michele, 2015; Ekerete *et al.*, 2015; Kliche *et al.*, 2008). Its acceptance mainly comes from the fact that it is relatively versatile yet simple enough to be useful in practice. It is more flexible than the exponential (Marshall and Palmer, 1948) and provides a "reasonably good fit" to measured DSDs. In addition to the conventional distributions like gamma, more complex models have also been proposed in the literature (Cugerone and De Michele, 2015; Ekerete *et al.*, 2015; Ignaccolo and De Michele, 2014; Thurai and Bringi, 2018). Although they are better at representing real DSDs, they are more difficult to use in practice due to their large number of parameters that cannot be retrieved using remote sensing measurements.

Despite its being the most widely used model, only a few studies have focused on precisely quantifying the adequacy of the gamma distribution. Johnson *et al.* (2015) compared the performance of four conventional unimodal and skewed to the right distributions that may be considered as potential DSD models. They highlighted that the gamma model provided the best fit, followed by the lognormal, beta and, finally, the Weibull. Adirosi *et al.* (2016) fitted three distributions, lognormal, gamma, and Weibull, and compared their goodness of fit using the Kolmogorov–Smirnov test (K-S test). They showed that the gamma distribution has the lowest rejection rate, while Weibull is the most frequently rejected. Ekerete *et al.* (2015) used the chi-square goodness-of-fit test for testing several candidate models against the observations and concluded that DSDs are somewhere between the bimodal and the gamma shape, suggesting that gamma or lognormal distributions are not fully adequate. Their recommendation is to use a Gaussian mixture model with three centers. Similarly, Cugerone and De Michele (2015) pointed out that the gamma and lognormal model are not accurate enough based on K-S test and

a skewness-kurtosis diagram and suggested to use a four-parameter distribution (i.e., Johnson SB) instead. That diagram is one of the various graphical methods for determining visually whether sample data conform to a reference distribution. Among them the most commonly used graphical tools are the quantile-to-quantile plots or Q-Q plots (Watanabe and Ingram, 2016; Yakubu *et al.*, 2014) and the density plots (Adirosi *et al.*, 2016; Ekerete *et al.*, 2015) as well.

None of these studies focused on sampling resolution as a major factor nor provided clear guidelines for how it should be taken into account when evaluating the gamma model. All of them used a similar resolution (1-min DSDs), ignoring questions like "Does the gamma model perform better at lower/higher resolutions than 60 seconds?" or "When should we not use a gamma model?" These are very relevant questions when we take into consideration that DSD measurements at higher temporal resolutions are affected by larger sampling uncertainties. Although it was not the main scope of their study, Adirosi *et al.* (2015) suggested that the adequacy of the gamma model is likely to decrease with higher temporal resolutions.

In this paper, we take a closer look at the adequacy of the gamma model for representing DSDs. Our analysis starts by fitting gamma distributions on a DSD dataset collected by an optical disdrometer over a 2-month period. The adequacy of the fit is assessed based on a combination of Kolmogorov-Smirnov goodness-of-fit test and Kullback-Leibler divergence. The novelty of the study lies in its focus on the influence of the sampling resolution and how it affects the adequacy of the gamma model. A new adaptive DSD sampling technique capable of determining the highest possible temporal sampling resolution at which the gamma model provides an adequate fit is proposed.

The work is organized as follows. In Section 2.2, we introduce the data used in our study, and in Section 2.3 we present the followed methodology. The adequacy of the gamma model and its sensitivity to the sampling resolution is presented in Section 2.4. Finally, the conclusions are provided in Section 2.5.

2.2 Data

The DSD data used in this study were collected by a Parsivel[2] (Particle Size and Velocity) optical disdrometer located at the CESAR (Cabauw Experimental Site for Atmospheric Research) observatory during the ACCEPT (Analysis of the Composition of Clouds with Extended Polarization Techniques) campaign in October and November 2014, in a collaboration between TROPOS (Leibniz Institute for Tropospheric Research, Germany) and Delft University of Technology. Cabauw is located in the western part of the Netherlands, in a polder area, 0.7 m below mean sea level.

The measurement principle and performance of the Parsivel disdrometer have been extensively described in previous studies (Löffler-Mang and Joss, 2000; Tokay *et al.*, 2014); it uses a horizontal laser beam with an approximately 54 cm^2 measuring, sampling surface. When a raindrop passes through the laser beam, the attenuation in the received voltage and the time for the particle to leave the beam can be used to estimate the equivolume spherical raindrop diameter and the terminal fall velocity of the raindrop.

2

Diameter and velocity are divided in 32 non-uniformly spaced classes ranging from 0 to 25 mm and 0 to 21 m s^{-1}, respectively. All the drops in a given class are assigned to the center of the bin. Thus, the raw output data for a sampling interval is a 32×32 matrix of detected number of drops for each diameter and velocity class from which the volumetric size distribution of drops [m^{-3} mm^{-1}] can be estimated (Raupach and Berne, 2015). The first two diameter classes (0.062 and 0.187 mm) in the Parsivel are always empty due to the low signal-to-noise ratio. Therefore, the minimum detectable drop diameter is approximately 0.25 mm. From the DSD, integrated quantities can be inferred, such as rainfall rate (R) expressed in mm h^{-1} which is the amount of rain that falls over a given interval of time and radar equivalent reflectivity factor (Z) expressed in dBZ which is related to the backscattered radar signal of hydrometeors. For this study, volumetric DSD values at several temporal sampling resolutions were used, the highest being 30 s.

As in other related DSD studies (Adirosi *et al.*, 2014; Jaffrain and Berne, 2011; Thurai and Bringi, 2018) a selection criterion is applied to the whole DSD dataset before the analysis. Our selection is based on two main requirements:

- Only liquid precipitation is considered. This means that only the first 22 diameter classes of the Parsivel are used, starting from the 3rd (0.25 - 0.375 mm) up to the 22nd (6 - 7 mm), the latter corresponding to the biggest physically possible raindrops. DSDs with measurements between the 23rd and 32nd class (solid or mixed precipitation) were discarded. Further, the classification of precipitation particles provided by Parsivel was used, and only the following precipitation types were accepted: drizzle, drizzle with rain and rain. All DSDs attributed to other precipitation types were discarded.

- A threshold on the minimum number of size classes was set. All DSDs comprised of fewer than three different size classes were discarded. Moreover, all DSDs for which the rain rate estimated by the Parsivel is zero were discarded. This is necessary in order to remove suspicious observations such as noise from insects or other objects crossing the beam.

Table 2.1: Overview of the DSD dataset from Parsivel[2] optical disdrometer during the ACCEPT campaign. Sampling resolution, available number of DSD samples, accepted number of samples after applying the filtering criteria, mean, 50%, 90%, and 99.9% quantile and maximum value of rain intensity, reflectivity factor, mass-weighted mean diameter, and number concentration.

Sampling resolution 30 sec	No. of DSD spectra 24289		No. of samples after selection 12329
	Rain intensity (R) [mmh^{-1}]	Reflectivity factor (Z) [dBZ]	Mass-weighted mean diameter (D_m) [mm]	Number concentration (N_T) [m^{-3}]
Mean	0.76	16.17	0.89	401
50.0% (median)	0.33	16.20	0.82	225
90.0%	2.02	29.36	1.33	700
99.9%	11.20	42.08	3.12	8263
Max	26.31	47.82	4.92	11193
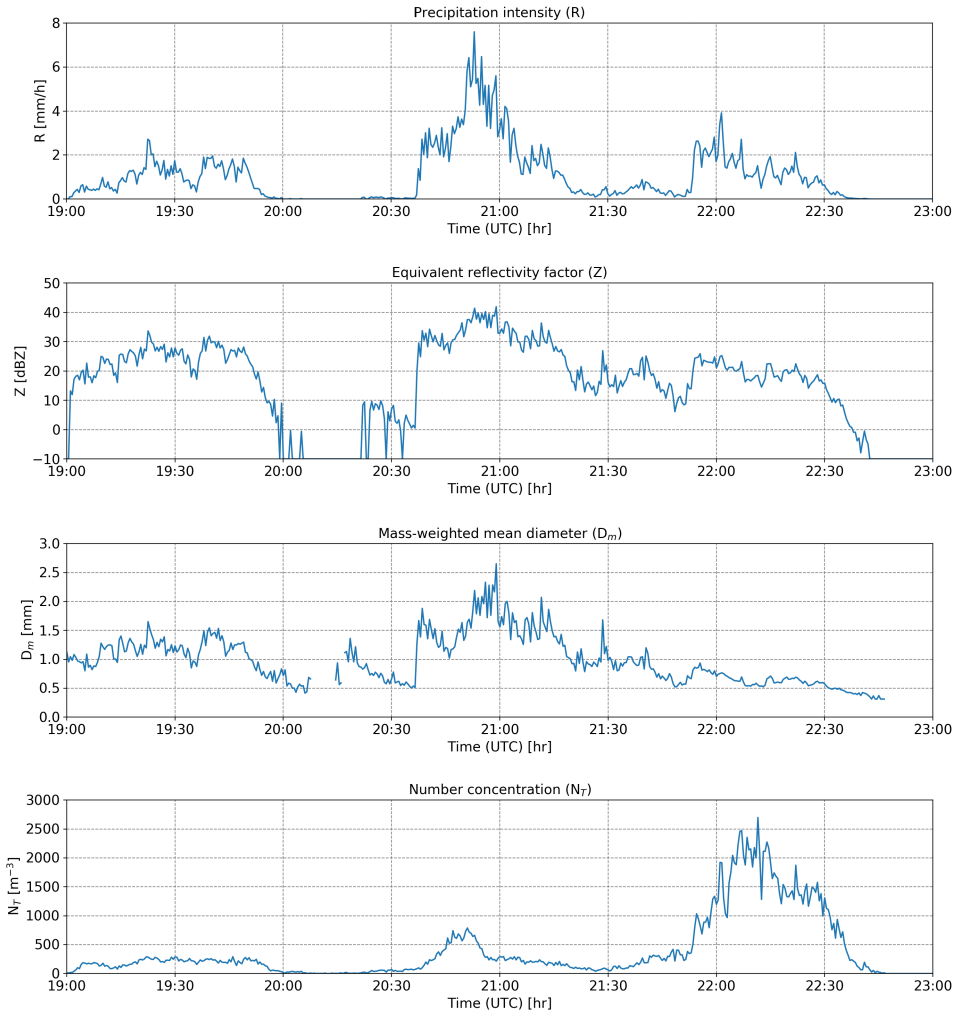
Figure 2.1: Time series of (top to bottom) precipitation intensity [mm h^{-1}], reflectivity factor [dBZ], mass-weighted mean diameter [mm], and number concentration [m^{-3}] from disdrometer data on 12 October 2014.

The application of the selection procedure described above to the whole dataset (24289 DSD spectra) resulted in 12329 30-s DSD spectra. From the 11960 DSD that were excluded, more than 80% were discarded due to the spurious signals (noise) with only one diameter class and around 1.5% because of solid or mixed precipitation. In Table 2.1 we present the different percentiles of rain rate, reflectivity factor, mean diameter and number concentration corresponding to the whole dataset. These values indicate that the dataset mostly contains light rain, with 90% of the time steps corresponding to rain rates of less than 2 mm h^{-1}, which in terms of reflectivity factor is less than 30 dBZ and in terms of mean drop sizes less than 1.33 mm. This can be explained if we take into account the fact that the ACCEPT campaign took place in October-November in the

Netherlands, during the cold season. Hence most of the rain events are frontal in nature and convective events are rare. However, there are also some larger values with rain rates between 11.2 and 26.31 mm h^{-1}, number concentration between 8263 and 11193 drops per cubic meter and mean diameter between 3.12 and 4.92 mm. Note that the maximum mean diameter (4.92 mm) is suspicious and probably corresponds to solid precipitation incorrectly classified by the disdrometer highlighting the limitations of the Parsivel in terms of detection of small/big droplets (Tokay *et al.*, 2014). For example, an overestimation of large drops is possible due to the sensor's limited sampling area or multiple drops passing through the laser beam at the same time, resulting in artificially larger drop sizes.

For illustration and study purposes, one particularly interesting event during the campaign was chosen (12 October, 2014). This event was selected because it exhibits a large natural variability in DSD. As can be seen from Figure 2.1, the event started at 19:00 UTC and lasted almost 4 h. According to the measured DSDs in Figure 2.2, the event can be divided into three separate parts, each of them with its own characteristics. The first part between 19:00 and 20:00 UTC is characterized by a relatively stationary DSD, with no remarkable changes in the number concentration (between 200 and 300 raindrops per cubic meter) and a mean diameter mainly between 1 and 1.5 mm. During the second part between 20:40 and 21:20 UTC, the mean drop size increases and the DSD becomes more variable, with rain rates between 1.5 and 7.5 mm h^{-1}. The last part between 21:58 and 22:37 UTC exhibits a more stable DSD with a large number of small drops below 1 mm (drizzle conditions). It should be noted that even though the number concentration has a peak around 22:11 UTC ($N_{T,max} = 2698$ m^{-3}), the equivalent reflectivity factor and the precipitation intensity peak before 21:00 UTC, highlighting the larger sensitivity of both variables to the drop sizes rather than concentration.
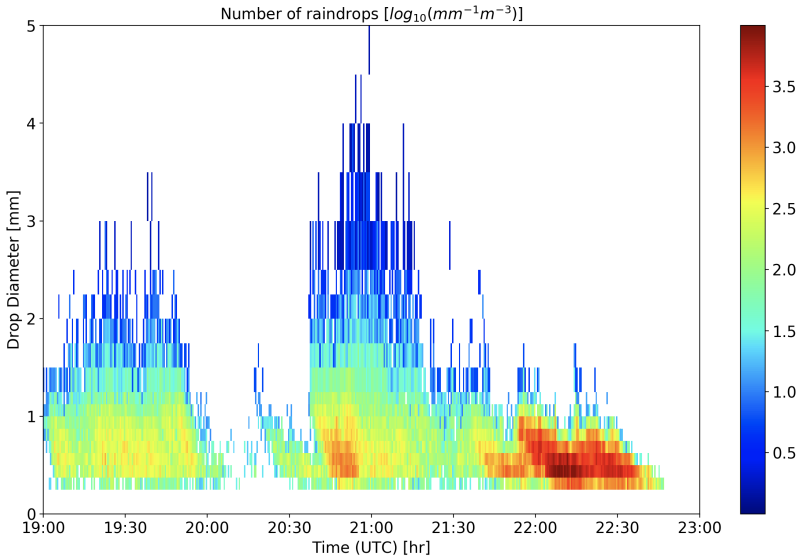

Figure 2.2: Volumetric drop size distributions $N(D)$ [m^{-3}mm^{-1}] in logarithmic scale as a function of time for the study case on 12 October 2014.

2.3 Methodology

Disdrometers provide detailed information about the DSD and its variation over time. However, when we need to derive DSDs using radar or satellite data, because of the limited set of available observables, it is necessary to summarize this information in the form of a mathematical model. Unfortunately, it is impossible to find simple models that perfectly capture the complex, natural properties of observed DSDs. One of the most common DSD models used in practice is the gamma model by Ulbrich (1983):

$$N(D) = N_0 D^\mu e^{-\Lambda D}, \tag{2.1}$$

where N_0 is the intercept parameter [m^{-3} mm$^{-1-\mu}$]; μ is the shape parameter [unitless] and Λ is the slope parameter [mm^{-1}]. To overcome the dependence of N_0 to μ, the model is often reformulated and normalized (Bringi *et al.*, 2003; Testud *et al.*, 2001):

$$N_{model}(D) = N_w f(\mu) \left(\frac{D}{D_m}\right)^\mu e^{-(4+\mu)\frac{D}{D_m}}, \tag{2.2}$$

with

$$f(\mu) = \frac{6}{4^4} \frac{(\mu+4)^{(\mu+4)}}{\Gamma(\mu+4)}, \tag{2.3}$$

$$\Lambda = \frac{4+\mu}{D_m}, \tag{2.4}$$

where D_m [mm] is the mass-weighted mean diameter and N_w the generalized intercept parameter [m^{-3} mm^{-1}] whose unit does not depend on μ. Various methods have been proposed to estimate gamma DSD parameters (N_w, μ, D_m) from disdrometer observations. In this study we focus on the two most common: the Method of Moments (MoM) and Maximum Likelihood Estimation (MLE).

2.3.1 Method of Moments (MoM)

The MoM is based on the fact that the unknown parameters of the fitted DSDs can be expressed as a combination of different weighted moments of the DSD (Ulbrich, 1983). Different versions of MoM have been proposed depending on the application: the μ-search method applied to normalised spectra (Thurai *et al.*, 2014), the L-moment method (Johnson *et al.*, 2011; Kliche *et al.*, 2008) and the method of truncated moments (Ulbrich, 1985). Here we focus on the first. For each observed DSD provided by the Parsivel disdrometer, the D_m and N_w are calculated:

$$D_m = \frac{\sum\limits_{i=3}^{22} N(D_i) D_i^4 dD_i}{\sum\limits_{i=3}^{22} N(D_i) D_i^3 dD_i}, \tag{2.5}$$

$$LWC = \frac{\pi \rho_w}{6} \sum_{i=3}^{22} N(D_i) D_i^3 dD_i, \tag{2.6}$$

$$N_w = \frac{4^4}{\pi \rho_w} \left(\frac{LWC}{D_m^4} \right),$$

(2.7)

where LWC denotes the liquid water content expressed in g m^{-3}, ρ_w is the density of water [10^{-3} g mm^{-3}], D_i is the center of the ith diameter class, $N(D_i)$ is the measurement by Parsivel (volumetric size distribution), and dD_i is the width of the ith diameter class. D_m is computed as the ratio of the 4th to the 3rd moment of the DSD. Using the calculated N_w and D_m values, the shape parameter μ can be computed. The optimal shape parameter μ is estimated for every individual time step, by determining the value of $\mu \in$ [-3, 15] that minimizes the following cost function (Thurai *et al.*, 2014):

$$CF = \sum_{i=3}^{22} | \log_{10}[N(D_i)] - \log_{10}[N_{model}(D_i \,|\, \mu)] |.$$

(2.8)

The applied brute force search tests all possible values of μ between -3 and 15 with steps of 0.01 and selects the one that minimizes Equation 2.8. Note that due to the large number of zeros in measured DSD spectra ($N(D_i) = 0$) and the numerical issues related to $\log_{10}(0)$ in Equation 2.8, instead of the logarithms, square roots were used in this study.

2.3.2 Maximum Likelihood Estimation (MLE)

The second method used to estimate the parameters of the gamma DSD model is the MLE. MLE is a statistical technique for evaluating how likely it is to observe a specific output under the assumption of a given set of model parameters. Several studies have applied MLE method for DSD retrievals (Adirosi *et al.*, 2016; Schleiss *et al.*, 2009; Thurai *et al.*, 2014). The goal of MLE is to find a pair of μ, Λ values (μ^*, Λ^*) that maximizes the log-likelihood function:

$$\sum_{i=1}^{n} \ln[f(y_i; \mu^*, \Lambda^*)] = max,$$

(2.9)

where $y_1, y_2, ..., y_n$ are the observations, $f(y_i)$ denotes the density, and n the total number of observations. In case of a gamma distribution $f(y)$ is given by:

$$f(y; \mu, \Lambda) = \frac{\Lambda^{\mu+1}}{\Gamma(\mu+1)} y^\mu e^{-\Lambda y}.$$

(2.10)

Note that because the Parsivel disdrometer outputs the number of drops per cubic meter and per diameter class i [$N(D_i)$] and not the total number of observations, n is given by:

$$n = \sum_{i=3}^{22} N(D_i).$$

(2.11)

To take the binning into account, Equation 2.9 is rewritten in terms of the Parsivel observations:

$$\sum_{i=3}^{22} N(D_i) ln[f(D_i; \mu^*, \Lambda^*)] = max.$$

(2.12)

The MLE is the pair of parameters (μ^*, Λ^*) that maximizes Equation 2.12. This is determined through numerical optimization, for example by using a steepest gradient method. As initial values (μ_0, Λ_0) for the optimization, the results from the MoM and Equation 2.4 can be used.

One important limitation of the Parsivel data is the effect of censoring at the lower and higher drop end. Therefore, some studies have suggested to rescale the density function in the likelihood function over the range of observable diameter classes (Johnson *et al.*, 2014). In this case the density in Equation 2.10 becomes:

$$f(D_i; \mu, \Lambda) = \frac{\int_{D_{i,min}}^{D_{i,max}} \frac{\Lambda^{\mu+1} y^\mu e^{-\Lambda y}}{\Gamma(\mu+1)} dy}{\frac{\gamma(\mu+1, \Lambda D_{22,max})}{\Gamma(\mu+1)} - \frac{\gamma(\mu+1, \Lambda D_{3,min})}{\Gamma(\mu+1)}}, \tag{2.13}$$

where γ is the incomplete gamma function, $D_{i,max}$ and $D_{i,min}$ are the upper and lower boundary of the ith diameter bin (with i = 3, 4,.., 22), respectively, with $D_{22,max}$ = 7.0 mm and $D_{3,min}$ = 0.25 mm. In this study, both approaches were used whereas it should be pointed out that the first (without rescaling) is significantly faster than the second. The MLE for truncated and binned data will be discussed further in Appendix A.

2.3.3 Kolmogorov-Smirnov goodness of fit test (K-S test)

As mentioned before, this study primarily focuses on the adequacy of the gamma model. This will be examined using two statistical tools. The first is the K-S test. The K-S test is a non-parametric test that quantifies the difference D_n between the empirical distribution function (ECDF) of the sample (F_n) and the cumulative distribution function (CDF) of a reference distribution (F):

$$D_n = \sup_x | F_n(x) - F(x) |, \tag{2.14}$$

where $\sup_x$ is the supremum of the set of distances. From D_n, a p-value can be calculated which is used to reject or accept the null hypothesis (H$_0$) that the DSD sample comes from the theoretical gamma distribution (Adirosi *et al.*, 2016; Cugerone and De Michele, 2015). When the p-value is smaller than the significance level (α = 0.05) the gamma model is rejected. To apply the K-S test, the function "scipy.stats.kstest" from the SciPy Python library was used.

At this point it is worth mentioning that because the K-S test can be applied only to continuous distributions, it is not directly applicable to a discrete dataset like the binned DSD observations provided by a Parsivel disdrometer. To overcome this issue, randomization of the drop sizes based on a uniform random distribution of the raindrops over each class was used (Chambers *et al.*, 1983; Ignaccolo and De Michele, 2014). The drops can also be redistributed according to the density function of a gamma distribution. But our analyses showed that this is much slower and does not significantly change the results.

Also, it should be noted that because the K-S test is applied to estimated model parameters, the mathematically correct but computationally expensive way to determine the p-values is through Monte Carlo simulations, as recommended by several authors

(Adirosi *et al.*, 2016;   Ignaccolo and De Michele, 2014;   Laio, 2004).   Again, both approaches were considered. For the application of the K-S test using Monte Carlo simulations ("exact" K-S test), the reader is referred to Appendix B.

2.3.4 Kullback-Leibler divergence

The second tool used to evaluate the adequacy of the gamma model is the Kullback–Leibler divergence (D_{KL}) also known as relative entropy (Kullback and Leibler, 1951):

$$D_{KL}(P \parallel Q) = \sum_{i=3}^{22} P(D_i) \ln \left[\frac{P(D_i)}{Q(D_i)} \right], \tag{2.15}$$

$$P(D_i) = \frac{N(D_i)}{\sum\limits_{i=3}^{22} N(D_i)}, \tag{2.16}$$

where $P(D_i)$ denotes the probability distribution function (PDF) of the observations from the disdrometer and Q is the PDF of the reference distribution (gamma model, Equation 2.10). The D_{KL} measures how much work needs to be made in order to transform one distribution into the other. Values close to 0 mean that P and Q are very similar, while a value of 1 indicates that they are completely different. In contrast to the K-S test output which is a "Yes" or "No", the D_{KL} provides a more nuanced answer in terms of how close or far away the modeled DSD is from our initial gamma DSD assumption. By combining K-S test and D_{KL}, a more detailed assessment of the adequacy of the gamma model can be made. Similarly to the K-S test, D_{KL} is calculated using the Python function "scipy.stats.entropy" from the SciPy library.

2.3.5 Adaptive sampling

Natural variability in rain means that the DSD is seldomly constant over time. However, for everything that follows, we assume local statistical stationarity in the DSD, i.e., that the unconditional joint probability function of raindrop sizes and number concentrations are invariant over small time intervals and spatial volumes. This is common practice and necessary for making inference, although questionable from an observational point of view (see, e.g., Jameson and Kostinski (2001), Ignaccolo *et al.* (2009), Schleiss *et al.* (2014) and Gires *et al.* (2015)). In fact, non-stationarity in rainfall could be one of the reasons why the gamma model is not equally good at representing DSDs across different aggregation time scales.

In addition to that, measurements can also be affected by significant uncertainties due to the limited sampling area of the Parsivel. As a result, the adequacy of the model will change depending on the considered sampling resolution. To reveal this sensitivity, the original measurements at 30 s were resampled to lower temporal resolutions. Resampling was done by averaging the 30-s DSDs (i.e., summing consecutive DSDs and dividing by the number of measurements) backward in time, using overlapping 30-s windows.
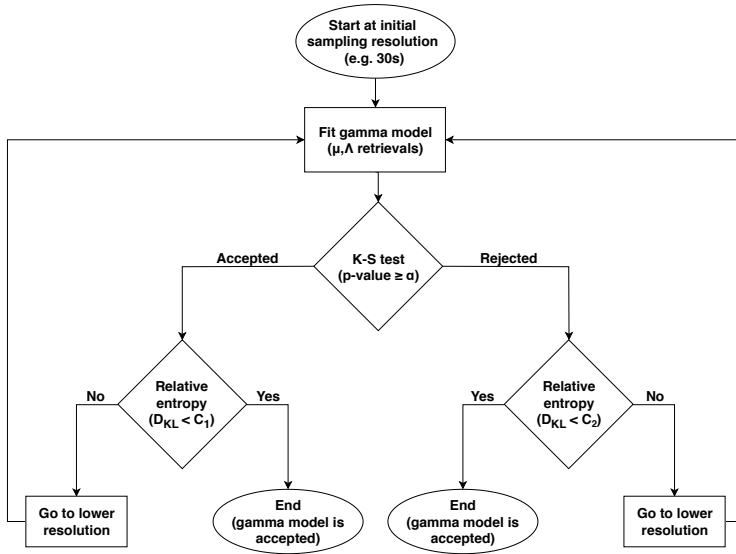
Figure 2.3: Flow-chart of the adaptive sampling algorithm for determining the highest possible resolution at which the gamma hypothesis is adequate.

An adaptive sampling technique is used to determine the highest possible temporal sampling resolution at which the gamma model provides an adequate fit. The adequacy is assessed by using a combination of K-S test and Kullback-Leibler divergence (D_{KL}). As can be seen schematically (Figure 2.3), the algorithm is an iterative procedure which starts at the highest possible sampling resolution (e.g., 30 s). At this resolution, the gamma model is fitted and its parameters (μ, Λ) are retrieved. The K-S test is applied to the fitted model and D_{KL} is calculated. Based on the acceptance or the rejection of the K-S test, the right or left branch of the decision tree is followed. In both cases, an additional test on the D_{KL} with thresholds C_1 and C_2 determines whether the algorithm ends or not. If D_{KL} is greater than C_1 and the K-S test is accepted or if D_{KL} is greater than C_2 and the K-S test rejects, the gamma model is rejected at this specific resolution and this procedure continues to a lower sampling resolution. The two other cases result in the gamma model being accepted and the algorithm moves on to the next DSD observation. The two thresholds C_1 and C_2 characterize how tolerant the algorithm is with respect to deviations from the gamma model. To set them, the gamma model was fitted for every DSD in the database at every possible resolution from 30 seconds up to 30 minutes with a step of 30 s and the K-S test was applied to each sample. The 90th quantile of D_{KL} for all cases where the K-S test was rejected was taken as an estimate for C_1. Similarly, C_2 was estimated by taking the 90th quantile of D_{KL} for all cases for which the K-S test was accepted. This resulted in $C_1 = 0.09$ and $C_2 = 0.05$ meaning that the tolerance level is lower when K-S test rejects than when it accepts. The values of C_1 and C_2 above were derived empirically without any considerations for performance. They are specific to our dataset and other values can be chosen depending on user requirements. For more discussion on the choice of C_1 and C_2 and how they affect the results, see Appendix C.

2.4 Results

2.4.1 Adequacy of gamma model at 30 seconds

In the following, the adequacy of the gamma model is investigated at 30-s resolution through the K-S test and Kullback-Leibler divergence (D_{KL}) described in Sections 2.3.3 and 2.3.4. For the following computations, the simple K-S test (without Monte Carlo simulations) and the simple MLE (without truncation and rescaling) were used. For more details about the other versions ("exact" K-S test, truncated MLE), see Appendixes A and B. We start by examining the results for the study case on 12 October 2014. The p-values from K-S test and D_{KL} are shown in Figure 2.4. They show that 89.8% of the 30-s samples do not pass the K-S test at a significance level of $\alpha = 0.05$, meaning that the majority of the observed DSDs during this event are not strictly distributed according to the gamma model. At the same time, most D_{KL} values during this rain event remain relatively close to zero, indicating that the DSDs are not far away from a gamma distribution either, in contrast to what the K-S test suggests. This can be explained by the fact that D_{KL} only looks at the shape of the distribution while the power of the K-S test is heavily dependent on the number concentration, with large samples being more likely to result in rejection (Cugerone and De Michele, 2015; Mohd Razali and Yap, 2011).

An example of this situation can been seen from 20:40 to 21:00 UTC at the beginning of the second part of the event and from 21:45 UTC until the end of the event (third part) where the K-S test rejects the gamma assumption but D_{KL} is low ($D_{KL} < 0.1$), suggesting that the gamma model is a reasonable approximation. The disagreement between K-S test and D_{KL} during these periods was expected since the two peaks of number concentration were detected here (Figure 2.1). By contrast, higher acceptance rates for the K-S test were found in the first part of the event (19:00-20:00 UTC) which is characterized by a relatively stable period of light rain with stationary DSD (Figure 2.2) and p-values that are frequently above 0.05.

Two (special) periods during which the K-S test mostly accepts the gamma hypothesis were identified from 20:23 to 20:37 and from 21:26 to 21:41 UTC. The first period is characterized by a very peaked DSD covering a limited number of diameter classes (i.e., between 3 and 5) and forming a triangular shape distribution. The second is a transitional period of very light rain between the second and the third part of the event. Both periods are characterized by small number concentrations which is the main reason the gamma model gets accepted by the K-S test, even though visually the distributions do not look like a gamma distribution, especially for the transitional period (Figure 2.2).

Except for the cases when the number concentration is high enough for the p-value of the K-S test to be equal to 0, we see that often a local maximum for the K-S test corresponds to a local minimum for the D_{KL}. However, the overall agreement between the two metrics (K-S test and D_{KL}) remains weak (correlation coefficient of -0.31), highlighting the different type of information provided by the K-S test and D_{KL}.

Based on the output of K-S test and D_{KL}, four interesting cases are presented in Figure 2.5. The first (Figures 2.5a and 2.5b) corresponds to a measurement made at 19:34 UTC when the p-value is high and the Kullback-Leibler divergence is almost zero. There is an agreement between the two metrics, since K-S test clearly accepts the gamma hy-
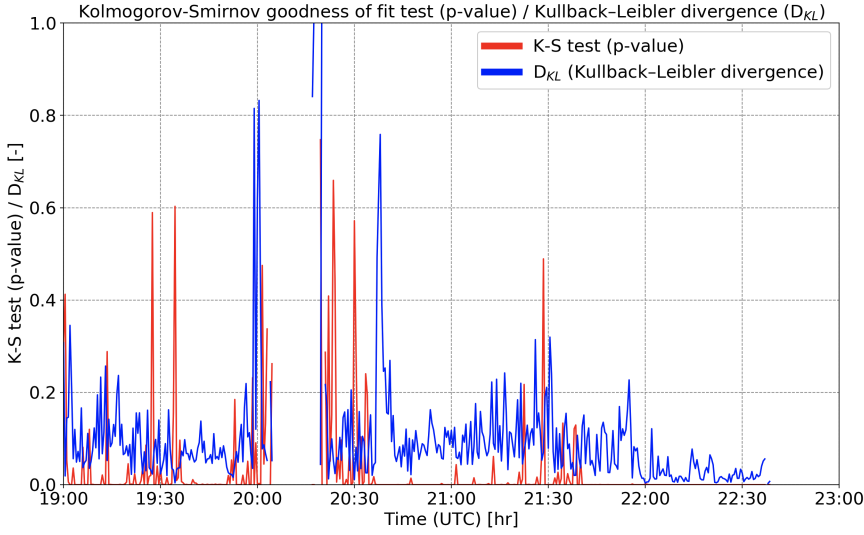
Figure 2.4: The p-values (K-S test) and D_{KL} (Kullback-Leibler divergence) at 30 s on 12 October 2014.
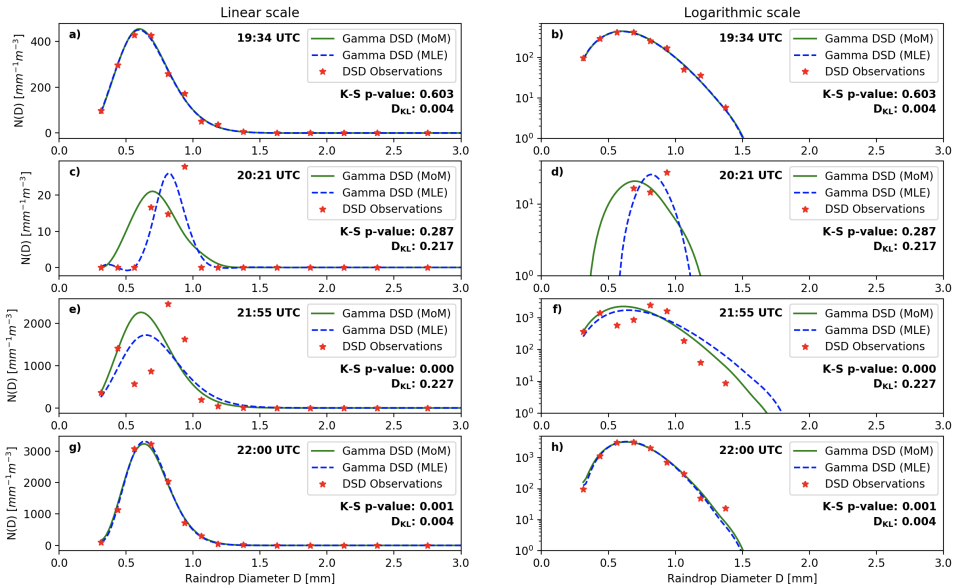
Figure 2.5: Four interesting DSDs from the case study. a-b) High p-value and low D_{KL}, c-d) both p-value and D_{KL} relatively high, e-f) p-value low and D_{KL} high, and g-h) both p-value and D_{KL} low.

pothesis and D_{KL} indicates good agreement between observations and the fitted gamma distribution (Figures 2.5a and 2.5b). However, this is not always the case, as shown by the observation at 22:00 UTC in Figures 2.5g and 2.5h. Here the agreement between the ob-

servations and the fitted gamma model is visually good as confirmed by a D_{KL} value close to zero. Nevertheless, the K-S test rejects the gamma hypothesis due to a large number concentration (N_T = 1196 m^{-3}). The two remaining cases (Figures 2.5c, 2.5d, 2.5e, and 2.5f) correspond to spectra that cannot be approximated by a gamma distribution. Figures 2.5e and 2.5f shows a DSD that exhibits bimodal characteristics (forcing both statistical tests to reject the gamma hypothesis no matter what the number concentration is), while Figures 2.5c and 2.5d shows a case where the Kullback-Leibler divergence is rather large (D_{KL} = 0.217) but the K-S test accepts the gamma hypothesis (p-value = 0.287 > α) due to the low number concentration (N_T = 23 m^{-3}).

On average, over the whole event, only 1 out of 10 DSDs at 30 s strictly conformed to the gamma model (according to K-S test only). A similar low acceptance rate was found for the whole dataset. Out of 12329 DSD spectra at 30-s resolution, 42% were accepted as gamma, of which only 21% were accepted by both K-S test and D_{KL} which means that almost 79% were not perfectly gamma according to the K-S test, but it is close enough to be approximated by one according to the D_{KL}. One reason to explain the low acceptance rate can relate to the cases with large N_T values. Another reason which could explain the high rejection of the gamma hypothesis is related to the limitations of the measurements, since Parsivel is susceptible to errors in the recorded drop concentrations, particularly for small and large drops (Raupach and Berne, 2015; Tokay *et al.*, 2014). However, the implications of this are not fully clear yet. For example, another study (Thurai and Bringi, 2018) has suggested that there might be larger deviations from the gamma model at smaller diameters than suggested by the Parsivel, meaning that the rejection rates could be even higher in case better data at the low end of the spectra were available. Therefore, several other studies (Lee *et al.*, 2004; Thurai and Bringi, 2018) proposed to use the generalized gamma formulation, which is a more flexible model with additional parameters that appears to better fit naturally occurring DSDs than the standard gamma.

2.4.2 Influence of sampling resolution on gamma model adequacy

In Section 2.3.5, a novel adaptive sampling technique was proposed where the temporal sampling resolution is adapted until the gamma model provides an adequate representation of raindrop size distributions. The approach is based on an iterative use of Kolmogorov-Smirnov goodness-of-fit test and Kullback-Leibler divergence (Figure 2.3). In the following, the technique was applied to the whole dataset for 60 different sampling resolutions, starting from 30 s (sampling resolution of the original disdrometer DSD data) up to 30 m in regular steps of 30 s. If the gamma model is rejected at all resolutions, the procedure stops and the sample is flagged as being incompatible with the gamma model. Resolutions lower than 30 m were not used as the main objective is to work at the highest possible temporal resolution to capture the dynamics and microphysics of the rain and not mix different DSDs together.

In Figure 2.6 the application of the decision tree algorithm to the study case is presented. It shows that for the majority of the time-steps (86.8%), the gamma model was accepted at resolutions between 30 and 300 s. Most of the time (73.8%), the right part of the flow-chart was followed (D_{KL} < C$_2$) which means that the gamma hypothesis is not
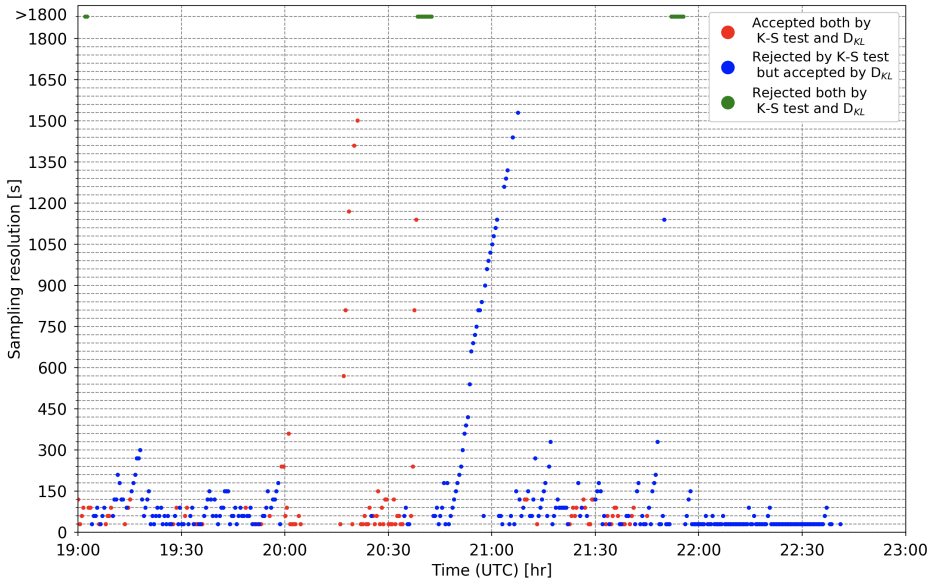
Figure 2.6: The output of the adaptive sampling algorithm for determining the highest possible resolution at which the gamma hypothesis is adequate (applied on the study case on 12 October 2014).

accepted by K-S test but the model is close enough to the observations to be useful. On the other hand, there are also a few interesting cases where lower resolutions are needed. One example is the period between 20:48 and 21:07 UTC during which the highest resolution at which the gamma assumption is acceptable increases at every time-step. Looking closer, we can see that at the beginning of that period (20:45 UTC), the gamma hypothesis was accepted at rather high resolution (below 90-s resolution). However, for the rest of the period, the DSDs were consistently incompatible with the gamma model, forcing the algorithm to downsample until the beginning of the period was included.

For a deeper understanding of the adaptive sampling algorithm, some examples highlighting the sensitivity of the results to the sampling resolution are presented. The four cases which were already discussed in the previous section (Section 2.4.1, Figure 2.5) are analyzed further here. Figures 2.7 and 2.8 present the fitted gamma DSDs, the p-values (K-S test output) and D_{KL} (Kullback-Leibler divergence) for different sampling resolutions (30, 60, 90 seconds etc.) until the iterative resampling algorithm stops. Together, these four cases cover all four possible paths in the decision tree algorithm.

The first case at 19:34 UTC (Figures 2.7 left, 2.5a, and 2.5b). is an example of a DSD for which the gamma model gets accepted right at the beginning at the 30-s sampling resolution (K-S test: 0.603 > 0.05, D_{KL}: 0.004 < 0.09). Thus, there is no need to downsample. Similarly for the spectra at 22:00 UTC (Figures 2.7 right, 2.5g, and 2.5h). The only difference in this example is that the gamma hypothesis gets rejected by K-S test (K-S test: 0.001 $\ngtr$ 0.05) but accepted by D_{KL} (D_{KL}: 0.004 < 0.05) which means that we follow the right branch of the flow-chart instead of the left one. This example demonstrates the importance of the D_{KL} criterion in the algorithm when the K-S test decisions

2
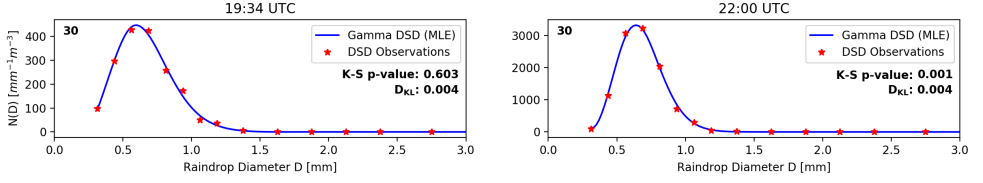
Figure 2.7: DSDs at 19:34 (left) and 22:00 UTC (right) at 30 s. The fitted gamma distribution is shown in blue. The p-values (K-S test) and D_{KL} (Kullback-Leibler divergence) result in acceptance of the gamma hypothesis.
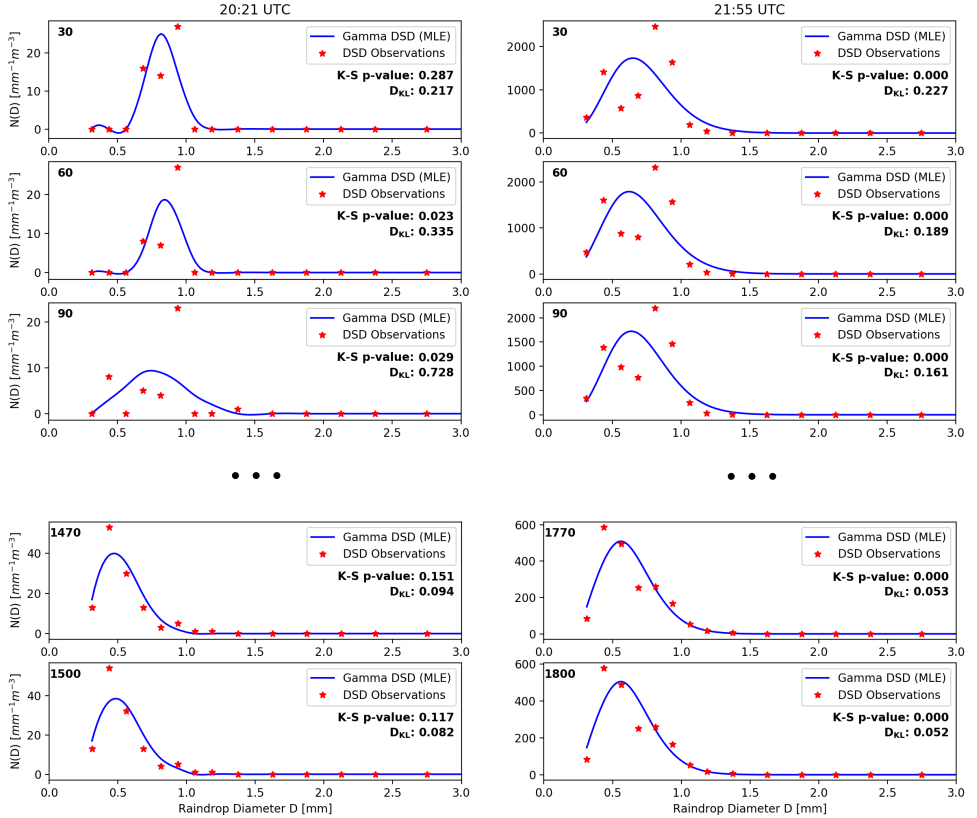
Figure 2.8: DSDs at 20:21 (left) and 21:55 UTC (right) for different sampling resolutions (30, 60, 90 s etc.) until the iterative resampling algorithm stops.

are heavily influenced by sample size. The two remaining cases are examples of situations where downsampling is required and more iterations of the algorithm are needed in order to have an acceptable agreement between the gamma model and the observations. The case at 20:21 UTC (Figures 2.8 left, 2.5c, and 2.5d) is an example of a DSD that passes the K-S test (p-value = 0.287 > 0.05) at 30-s resolution due to low sample size but is rejected by D_{KL} (0.217 $\not<$ 0.09). A lot of downsampling is required until both K-S test and D_{KL} accept the gamma assumption at 1500-s resolution (K-S test: 0.117 > 0.05,

D_{KL}: 0.082 < 0.09). The last case (21:55 UTC, (Figures 2.8 right, 2.5e, and 2.5f) is an example of a bimodal distribution. For that particular case, the distribution is too far away from the gamma model. Therefore, the algorithm rejects the gamma at all sampling resolutions up to 30 m. This last case is particularly interesting because it shows that the algorithm is also capable of revealing entire time periods during which the DSDs are completely incompatible with the gamma assumption irrespective of the temporal resolution. The latter is very valuable as mismatches between the model and the observations may not always be obvious to spot by eye just by looking at the disdrometer data. In our study case, two such periods were found (Figure 2.6). They last for approximately 4 min and can be characterized as transitional rain periods corresponding to the beginning of the second and third part in the event (see Section 2.2). Visual inspection of these two periods confirms that the DSDs are indeed bimodal. The first one (20:38-20:42 UTC) relates to a transition from peaked DSDs to broad DSDs with a large number of small raindrops. The second one (21:52-21:56 UTC) is just before the drizzle mode starts. A possible physical explanation for the second transition could be a raindrop break-up process during which larger drops break up into smaller ones. Both transitional periods are characterized by a bimodal shape resulting from the mixture of two different DSDs which is impossible to model by a gamma distribution. As long as the old and the new DSD regime overlap and none of them dominates the other, the model cannot be used.

For a more general overview of the performance of the resampling procedure, the decision tree algorithm was applied to the whole DSD dataset. Table 2.2 shows the acceptance rates for every possible resolution over the entire dataset. In addition, for every acceptance rate, the percentage which corresponds to the left part of the flow-chart (K-S accepts and $D_{KL} < C_1$) and the percentage due to the right branch of the decision tree (K-S rejects and $D_{KL} < C_2$) are given. We see that the acceptance rate of the gamma model at 30 s is 42.14%. When combined with the 60-s resolution, acceptance increases to 60.02%. When all the resolutions up to 300 s are combined, the overall acceptance rate is about 85.81%. While this is encouraging, it also means that in 15% of all cases, the gamma model did not fit the data reasonably well at high resolutions (5 min or higher). The high resolution requirement is crucial for hydrological applications or remote sensing since DSD can change quickly over the course of an event. Among the 15%, approximately one-third (5.55%) correspond to DSD spectra that do not follow a gamma distribution at any resolution (up to 1800 s), highlighting the importance of a careful DSD inspection and selection before the fitting procedure.

From the table we can also see a clear trend in the contributions of the left and right parts of the flow-chart which remain stable around 25-75% regardless of which sampling resolution was selected. This means that three out of four times the observed distribution is not perfectly gamma according to the K-S test, but it is close enough to be approximated by one according to the Kullback-Leibler divergence. Above 900 s, that proportion changes to 35-65%; however, the cases are noticeably fewer, representing only 2.3% of the entire dataset.

At this point it is worth highlighting that these results depend on the choice of C_1 and C_2, and will change for different thresholds and levels of tolerance. Even though for this study specific values for C_1 and C_2 were chosen, these are not optimal and other combinations can be used depending on the application. If one wants to be extremely strict,

2

Table 2.2: Acceptance rates for all possible resolutions from 30 to 1800 s for the whole dataset and the relative contributions of the left and right branches of the flow-chart to the acceptance rate.

Sampling resolution [s]	Acceptance rate [%]	Accepted both by K-S test [%] and D_{KL} [%]	Rejected by K-S test but accepted by D_{KL} [%]
30	42.14	21.04	78.96
60	17.88	30.17	69.83
90	9.17	27.43	72.57
120	5.26	26.50	73.50
150	3.54	24.08	75.92
180	2.34	18.34	81.66
210	1.73	25.82	74.18
240	1.46	24.44	75.56
270	1.26	25.16	74.84
300	1.03	24.41	75.59
[30 , 300]	85.81	24.27	75.73
[330 , 600]	4.59	23.67	76.33
[630 , 900]	1.75	20.37	79.63
[930 , 1200]	1.22	33.11	66.89
[1230 , 1500]	0.67	37.35	62.65
[1530 , 1800]	0.41	33.33	66.67
>1800 (never accepted)	5.55	-	-

C_1 and C_2 can be lowered, which will result in a drop of the acceptance rates, especially at higher resolutions. In this case the algorithm becomes equivalent to a single K-S test output. On the other hand, in case C_1 and C_2 are increased, the algorithm will accept the vast majority of the spectra, even the ones that are very far away from a gamma distribution. In general, results are more sensitive to C_2 than C_1 because the former defines the level of tolerance for the right branch of the decision tree (where the most of the acceptance comes from). For more details about the influence of C_1 and C_2 and the sensitivity of the results to the choice of these values, see Appendix C.

2.4.3 Model adequacy based on bulk variables (R, Z, D_m, N_T)

In the previous section, we showed how well the gamma model can describe DSD observations, based on the entire DSD spectra. However, for many applications only integrated values of the DSD (R, Z, D_m, N_T) are needed. Since these bulk variables are related to weighted moments of the DSD, the adequacy of the gamma model can also be examined as a function of these moments. For a deeper investigation of the importance of the method used to fit the DSDs, two different DSD parameter estimation methods (MoM and MLE) were used for the retrievals of μ and Λ, described in Sections 2.3.1 and 2.3.2.

The four bulk variables corresponding to the fitted DSDs during the case study are presented in Figure 2.9, together with the "true" values calculated directly from the disdrometer data. We can see that the observed bulk variables (R, Z, D_m, N_T) measured by the disdrometer and the bulk variables derived from the fitted gamma models using MLE and MoM do not always agree with each other, especially when the MLE is chosen as the parameter estimation method. This is clearly visible during the second part of the rain event (and partly during the first) during which MLE strongly underestimates D_m, R, and Z compared with the Parsivel and MoM.
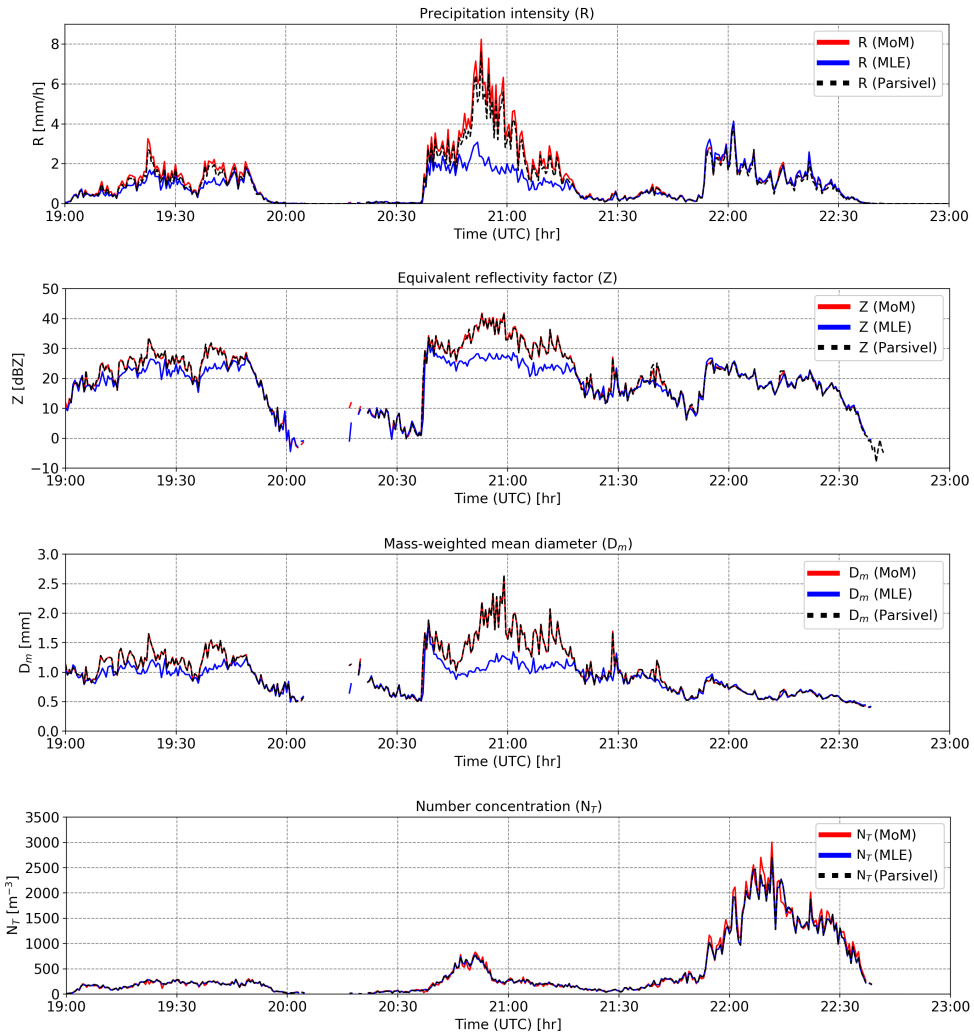
Figure 2.9: Time series of (top to bottom) precipitation intensity [mm h^{-1}], equivalent reflectivity factor [dBZ], mass-weighted mean diameter [mm], and number concentration [m^{-3}] on 12 October 2014 using MoM and MLE. The black line represents the value measured by the Parsivel disdrometer.

The disagreements can be explained by the fact that most DSDs during the second time period are not well approximated by the gamma model according to Figure 2.6. Also, the DSD spectra include bigger drops which are known to have a large influence on higher order moments. Even though MoM makes the same mistake as MLE by assuming that the DSD is gamma, it is a better choice than MLE during this particular period because it explicitly tries to conserve the liquid water content, which is closely related to D_m and R and (to a lower degree), to the reflectivity factor Z. By contrast, MLE does not conserve the liquid water content, giving more weight to the smaller more numer-

ous drops in the spectra. Nevertheless, one should not discard MLE simply on that basis that it produces biased rainfall rates and reflectivities, as it can also lead to superior performance for lower-order moments of the DSD (such as N_T). Also, it is very important to point out that MLE performs very well in cases where the DSD is in good agreement with the gamma hypothesis. This can be seen during the third part of the event during which the gamma hypothesis is reasonable and both methods (MLE and MoM) are in good overall agreement with the Parsivel observations.

Table 2.3 provides a more general overview of the performance of MLE and MoM for the whole dataset, showing the root mean square errors for 4 bulk variables (R, Z, D_m and N_T). We can see that MoM results in errors that are almost 3 times smaller for rain rate and 9 times for reflectivity. On the other hand, MLE performs much better than MoM for low order moments, such as N_T. The conclusion is that both MoM and MLE can be good/bad choices depending on 1) the intended application and 2) how close or far the observed DSDs are from the gamma distribution.

Focusing on the third part of the event, the gamma DSD assumption is reasonable and the MLE method is capable of accurately estimating R and Z. This can be seen more clearly in Figure 2.10 where a scatter plot between the observations of D_m and the estimations of D_m using MLE are presented. It shows that for mean diameters up to 1 mm, there is good agreement between mass-weighted mean diameter observations and model estimates regardless of the acceptance or rejection of the gamma assumption. On the other hand, for diameters above 1 mm, MLE estimates of D_m tend to be underestimated compared with the observations. This underestimation is more severe when the gamma model is rejected than when it is accepted. Consequently, the performance of MLE bulk parameters depends both on the acceptance or rejection of the gamma hypothesis and on the value of D_m.

From the last two examples (second and third parts of the rain event), it is evident that the gamma model should not be viewed as an absolute truth for all DSDs but as an approximation whose validity needs to be assessed on a case by case basis. Failing to do so can result in large errors between calculated and measured moments. The same argument applies to the DSD estimation methods based on MoM and MLE, which have different behavior and properties depending on the validity of the gamma assumption and the D_m value. For example, while MLE is superior to MoM for cases where the DSD is gamma, it should be avoided in cases where the gamma DSD assumption is questionable or D_m is large. Similarly, in case the DSD is not perfectly gamma, it is better not to use truncated and rescaled MLE (for more details see Appendix A). The adaptive sampling algorithm presented in this paper can provide information about the adequacy of

Table 2.3: Root-mean-square error for the four bulk variables (R, Z, D_m, N_T) at 30-s resolution, for the whole dataset using Method of Moments (MoM) and Maximum Likelihood Estimation (MLE).

	Method of Moments (MoM)	Maximum Likelihood Estimation (MLE)
Rain intensity (R) [mm h^{-1}]	0.28	0.75
Reflectivity factor (Z) [dBZ]	0.41	3.53
Mass-weighted mean diameter (D_m) [mm]	0.02	0.21
Number concentration (N_T) [m^{-3}]	64.11	3.98

the gamma model from a statistical point of view, which can be helpful for interpreting changes in the microphysics of rain and selecting the most appropriate fitting method. This is an often overlooked aspect of DSD analyses that is crucial for creating robust and representative DSD databases for use in radar retrievals.
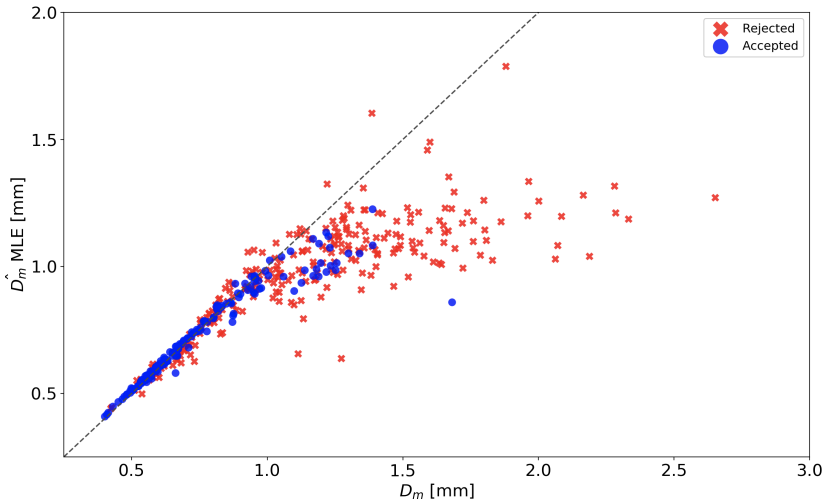

Figure 2.10: Scatter plot between the observations of D_m (from the Parsivel) and the estimated values $\hat{D}_m$ using MLE when the gamma DSD hypothesis is accepted and rejected for the case study on 12 October 2014.

2.5 Conclusions

A critical evaluation of the adequacy of the gamma model for representing raindrop size distributions was presented. The results are based on DSD data collected by a Parsivel optical disdrometer during a 2-month campaign in the Netherlands. A study case was presented and a table summarizing the results for the whole DSD dataset was provided. At first, the adequacy of the gamma model at 30 s was analyzed using the K-S test and Kullback-Leibler divergence and four interesting cases were highlighted. Then, the influence of the sampling resolution on the adequacy of the gamma model was investigated. A novel adaptive sampling technique was proposed to determine the highest temporal sampling resolution at which the gamma model provides an adequate representation of sampled DSDs. Finally, in order to assess the gamma DSD model from a more practical point of view, the accuracy of retrieved bulk variables (R, Z, D_m, N_T) was examined. According to the results the following conclusions can be drawn.

1. The majority of the DSD spectra are not perfectly gamma but are well approximated by the gamma model at high sampling resolutions (60.02% of the DSDs up to 60 s, 85.81% of the DSDs up to 300 s). However, a substantial number of DSDs (5.55%) were absolutely not complying with the gamma model, which means that careful selection of the DSD spectra is needed before fitting.

2

2. About three out of four times (across all temporal scales), the gamma hypothesis gets accepted not because of the K-S test (it is not perfectly gamma) but because of the Kullback-Leibler divergence. Thus, most DSDs are not truly gamma but come close to it.

3. One should not fit the two parameters μ and Λ of the DSD using MLE when the distribution is not perfectly gamma or, at least, very close to it. The same argumentation holds for truncated and rescaled MLE. Failing to do so results in underestimated D_m and R values. In this case the safer option is to use the MoM assuming that we want to retrieve high-order moments of the distribution (e.g., rain intensity, reflectivity factor).

4. The adaptive sampling algorithm proposed in this paper is capable of automatically identifying transition periods during which the DSD cannot be represented by a gamma model (at any resolution). These may not be easily visible in the data but become very clear after applying our algorithm.

Finally, it should be mentioned that this study is not a statement against the use of the gamma model which is often a good approximation. However, it highlights the importance of checking the adequacy of these assumptions. It also lays the foundation for a better automatic quality control of DSD retrievals for use in remote sensing applications. The main idea could also be applicable to other relevant research in the future, including an evaluation of the gamma model assumption on μ-Λ relationships used in polarimetric radar retrievals.

Chapter 3

Sensitivity analysis of DSD retrievals based on the μ-Λ relationship

Raindrop size distributions (DSDs) play a crucial role in quantitative rainfall estimation using weather radar. Thanks to dual-polarization capabilities, crucial information about the DSD in a given volume of air can be retrieved. One popular retrieval method assumes that the DSD can be modeled by a constrained gamma distribution in which the shape (μ) and rate (Λ) parameters are linked together by a deterministic relationship. In the literature, μ-Λ relationships are often taken for granted and applied without much critical discussion. In this study, we take another look at this important issue by conducting a detailed analysis of μ-Λ relations in stratiform rain and quantifying the accuracy of the associated DSD retrievals. Crucial aspects of our research include the sensitivity of μ-Λ relations to the temporal aggregation scale, drop concentration, inter-event variability and adequacy of the gamma distribution model. Our results show that μ-Λ relationships in stratiform rain are surprisingly robust to the choice of the sampling resolution, sample size and adequacy of the gamma model. Overall, the retrieved DSDs are in a rather decent agreement with ground observations (correlation coefficient of 0.57 and 0.74 for μ and D_m). The main sources of errors and uncertainty during the retrievals are calibration offsets in reflectivity (Z_{hh}) and differential reflectivity (Z_{dr}). Measurement noise and differences in scale between radars and disdrometers also play a minor role. The raindrop concentration (N_T) remains the most difficult parameter to retrieve, which can be off by several orders of magnitude. After careful data filtering and removal of problematic Z_{hh}/Z_{dr} pairs, the correlation coefficient for the retrieved N_T values remained low, only slightly increasing from 0.12 into 0.24.

3.1 Introduction

Understanding the natural variability of raindrop size distributions (DSDs) is crucial for radar remote sensing applications and microphysical parameterization in numerical weather prediction models (e.g., Thompson *et al.*, 2004). Most precipitation-related quantities (e.g., rain rate, mean drop diameter, number concentration, fall velocity, or liquid water content) directly depend on the DSD. Similarly, most radar observables (e.g., Z_{hh}, Z_{dr}) are weighted moments of the DSD. For these reasons, DSD retrieval methods play a central role in numerous weather radar studies.

Efforts to improve quantitative rainfall estimates by retrieving information about DSDs from radar and satellite observations have captured a great deal of interest in the meteorological community, especially after the introduction of polarimetric weather radar (Seliga and Bringi, 1976). Retrievals based on the reflectivity factor at horizontal polarization (Z_{hh}), differential reflectivity (Z_{dr}), and specific differential phase (K_{dp}) are the most common choices because of their natural link to raindrop concentrations, sizes, and shapes.

According to the literature, DSDs can be parameterized in the form of relatively simple models such as a gamma distribution with the three parameters μ, Λ and N_0 representing the shape, scale, and concentration, respectively. Algorithms for DSD retrievals take advantage of different relationships between radar observables and the three parameters of the gamma. Three main categories of retrieval methods can be distinguished: the first one consists of methods that use two radar observations Z_{hh} and Z_{dr}, as well as a constrained relationship between μ and Λ (Zhang *et al.*, 2001; Zhang *et al.*, 2003) or N_0 and μ (Ulbrich, 1983). The second category proposed by Bringi *et al.* (2002) and Gorgucci *et al.* (2002) uses the three radar observables Z_{hh}, Z_{dr}, and K_{dp}. However, this method is known to be very sensitive to noise in K_{dp} estimates. To reduce the uncertainty, the differential phase needs to be filtered and down-sampled, which limits the accuracy and spatial resolution of the retrievals. The last category consists of various retrieval techniques that require special types of radars or measurements, such as double frequency (Rose and Chandrasekar, 2006), triple frequency (Mróz *et al.*, 2020), and/or Doppler power spectra (Unal, 2015). In this paper, only the first category will be discussed.

The main challenges when retrieving DSDs from Z_{hh} and Z_{dr} are the choice of the N_0-μ or μ-Λ relationship and its validity across different rain types as well as spatial and temporal aggregation scales. In the literature, μ-Λ relationships are often taken for granted or transferred from one location or scale to another without much critical discussion. And while some studies have documented large differences in relationships across rain types (e.g., stratiform vs. convective), little is known about the sensitivity of μ-Λ relationships to the temporal sampling resolution of the disdrometer data used to infer them or the validity of the gamma assumption. Another important issue concerns the fact that the disdrometer data used to define μ-Λ relationships correspond to much smaller sampling volumes than the radar measurements to which they are applied. Therefore, it might be necessary to first apply a statistical transformation to the radar data before retrieving DSDs based on μ-Λ relationships or, equivalently, modify the μ-Λ relation to account for the difference in scale.

Finally, one last issue that tends to be overlooked is that radar measurements are likely to contain systematic errors in the form of calibration offsets in Z_{hh} and Z_{dr}. A possible error in the latter could induce large biases in the retrieved DSDs, especially in light rain with low Z_{dr} and a small signal-to-noise ratio. Several operational polarimetric weather radar networks such as the US Nexrad (Hubbert and Pratte, 2006) and the German DWD network (Frech and Hubbert, 2020) have already devoted extensive efforts toward mitigating these calibration issues. However, achieving and maintaining good calibration over time for research radars remain challenging.

In this paper, we perform a detailed analysis of the sensitivity of DSD retrievals from polarimetric radar to various error sources such as the validity of the μ-Λ relationship and its sensitivity to the temporal sampling resolution, inter-event variability, changes in number concentrations, and adequacy of the gamma distribution model. We also examine the sensitivity of the retrievals to measurement biases in Z_{hh} and potential biases in Z_{dr} due to differences in measurement scale. We illustrate the importance of all these issues by retrieving DSDs during several episodes of light to moderate stratiform rain in Cabauw, the Netherlands, and indirectly validating our retrievals by comparing them to disdrometer observations on the ground. The main focus is not on optimizing the DSD retrieval algorithm but on understanding its sensitivity to potential sources of errors, either directly linked to the radar measurements or indirectly through the critical modeling assumptions behind the method.

This paper is organized as follows. In Section 3.2, the data used are introduced. In Section 3.3, the methodology is presented. In Section 3.4, the main results for the μ-Λ relationship analysis are shown, followed by the sensitivity analysis of the DSD retrievals in Section 3.5. Finally, the conclusions are provided in Section 3.6.

3.2 Data

The data used in this study were collected in the Netherlands during the ACCEPT (Analysis of the Composition of Clouds with Extended Polarization Techniques) campaign between October and November 2014. During this campaign, a variety of different in situ and remote sensing measurements were collected at the CESAR (Cabauw Experimental Site for Atmospheric Research) observatory.

3.2.1 The disdrometer data

The ground DSD spectra used for calibration and validation were collected by a Parsivel[2] (Particle Size and Velocity) optical disdrometer. The working principle, strengths, and limitations of the Parsivel[2] have already been discussed in great depth in previous studies and will not be part of this study (Battaglia *et al.*, 2010; Löffler-Mang and Joss, 2000; Raupach and Berne, 2015; Thurai *et al.*, 2011; Tokay *et al.*, 2014). For example, the Parsivel is susceptible to errors in the lower drop diameter range, which can affect the DSD shape and number concentrations. However, no efforts have been made to try to correct for these issues within the context of this study. The raw DSD data consist of particle counts across 32 non-uniformly spaced diameter classes ranging from 0 to 25 mm with a

sampling resolution of 30 s. From the raw DSD, integrated quantities such as rainfall rate (R) and radar equivalent reflectivity factor (Z) can be derived (Bringi and Chandrasekar, 2001; Thurai and Bringi, 2008). The disdrometer measurements were used to fit gamma DSD models and derive constrained relations between μ and Λ parameters at different temporal resolutions, which is necessary for retrieving DSDs from polarimetric radar measurements. At the same time, the disdrometer measurements were also used to (indirectly) validate the radar retrievals and study their consistency over time and across different events.

Similarly to Gatidis *et al.* (2020), pre-processing is applied to the disdrometer data:

1. Only the liquid type of precipitation was considered for further analysis. All DSDs with observations above the 22nd diameter class (drop diameters greater than 7 mm) were discarded, since they correspond to mixed or solid precipitation.

2. Each DSD should be comprised of at least three different diameter size classes in order to exclude spurious observations not related to rain.

3.2.2 Radar data

The radar data used to perform the DSD retrievals were collected by TU Delft's polarimetric S-band (λ = 9.1 cm) FMCW radar TARA (Transportable Atmospheric RAdar; Heijnen *et al.*, 2000) in Cabauw, the Netherlands. TARA radar was collocated with additional sensors. This included a Parsivel disdrometer (see Pfitzenmaier *et al.*, 2018, Figure 1) provided by the Leibniz Institute for Tropospheric Research (TROPOS). For this experiment, the radar antenna elevation angle of TARA was fixed at 45° with constant azimuth. The collected polarimetric radar observables included the reflectivity factor at horizontal polarization (Z_{hh}) and differential reflectivity (Z_{dr}) at 200 m of height (corresponding to the minimum range of TARA). The full specifications of TARA during the ACCEPT campaign are given in Table 1 of Pfitzenmaier *et al.* (2018).

In order to make the radar data comparable with the disdrometer data, all Z_{hh} and Z_{dr} measurements were down-sampled over successive 30 s sampling intervals. The radar and disdrometer data were then synchronized by determining the time shift that maximized the correlation coefficient between Z_{hh} Parsivel and Z_{hh} TARA.

Concerning the calibration of Z_{hh} and Z_{dr}, noise measurements were performed every day to account for possible variations in range, especially at the beginning and end of the IF-filter. Before the start of the campaign, the calibration of Z_{dr} was verified using vertical profiling of drizzle and very light rain. The resulting histograms showed a mean offset of -0.11 dB with a standard deviation of 0.05 dB. Consequently, an offset of +0.11 dB was added to the measured Z_{dr} for the whole ACCEPT campaign. For the calibration of Z_{hh}, the transmit power was stored in the dataset, and there was a near-field correction for the non-full-overlap of the transmit and receive antenna beams using the method described in Sekelsky and Clothiaux (2002). However, an end-to-end calibration for Z_{hh} was missing.

3.2.3 List of events

A total of seven rain events over the whole measurement campaign were selected for further analysis. The criteria used to select events were as follows:

1. Each event must consist of predominantly stratiform rain and exhibit a well-defined melting layer signal in the radar data.

2. Each rain event must be at least 2 h in duration. This was deemed necessary to have enough data to fit a reliable μ-Λ relation and compute relevant performance metrics.

3. There should be no clear sign of changes in dynamics or microphysics (Gorgucci *et al.*, 2001; Jameson and Kostinski, 2001; Uijlenhoet *et al.*, 2003) with no long dry periods within each event.

4. Each event must contain several Z_{dr} and Z_{hh} values larger than 0.1 dB and 5 dBZ, respectively.

Table 3.1 presents a summary of the duration, rain intensity and mass-weighted mean diameter (based on the disdrometer data) for each of the seven selected events. As can be seen, most of the events last between 120 and 150 minutes. The longest on November 3 is slightly longer than 4 hours. The low rain intensity and mass-weighted mean drop diameter values confirm that the selected events are mostly comprised of light to moderate stratiform rain. This makes sense given the criteria used to select the events and the fact that the ACCEPT campaign took place in October-November in the Netherlands at a time when heavy convective events are rare.

For illustration purposes, one of the seven events (E2, 11 October, 2014) is plotted in Figure 3.1. As can be seen, this event mostly consists of stratiform rain with a moderate intensity of approximately 1.8 mm h^{-1} and a total duration of approximately 3 hours between 10:30 and 13:45 UTC, including a short break between 12:45 and 12:55 UTC according to disdrometer observations on the ground (Figure 3.2). The mass-weighted mean diameter is 1.1 mm, which is typical for light stratiform rain and small raindrop

Table 3.1: Overview of the selected events. Date, duration, number of samples, average rain intensity ($\overline{RR}$), average mass-weighted mean diameter ($\overline{D_m}$), average number concentration ($\overline{N_T}$), parameters of the μ-Λ relationship (α, β), their corresponding percentage relative errors, correlation coefficient between μ and Λ for each event, and root-mean-square deviation (RMSD) between μ and Λ points of each event as well as the overall relationship. Note that only the DSDs conforming to the gamma model (see Section 3.3.1, DSD model) were considered when computing these statistics.

| Event	Date	Duration [hh:mm]	No. of samples	$\overline{RR}$ [mm/h]	$\overline{D_m}$ [mm]	$\overline{N_T}$ [m^{-3}]	α	Percentage relative error α [%]	β	Percentage relative error β [%]	Correlation coefficient	RMSD
1	8 Oct	2:00	77	1.22	1.08	279	0.514	0.0	1.347	0.6	0.971	0.836
2	11 Oct	3:15	88	1.81	1.12	383	0.227	55.84	1.720	28.45	0.938	1.772
3	15 Oct	2:30	147	0.86	0.9	295	0.676	31.52	1.241	7.32	0.95	1.339
4	16 Oct	2:20	110	2.46	1.18	418	0.354	31.13	1.494	11.58	0.93	1.73
5	24 Oct A'	2:00	38	1.0	1.02	254	0.415	19.26	1.410	5.3	0.962	1.053
6	24 Oct B'	2:00	27	2.76	1.44	315	0.178	65.37	1.795	34.06	0.913	0.653
7	3 Nov	4:25	165	0.78	0.92	292	0.832	61.87	1.144	14.56	0.922	1.617
Overall	-	18:30	652	1.37	1.03	323	0.514	-	1.339	-	-	-
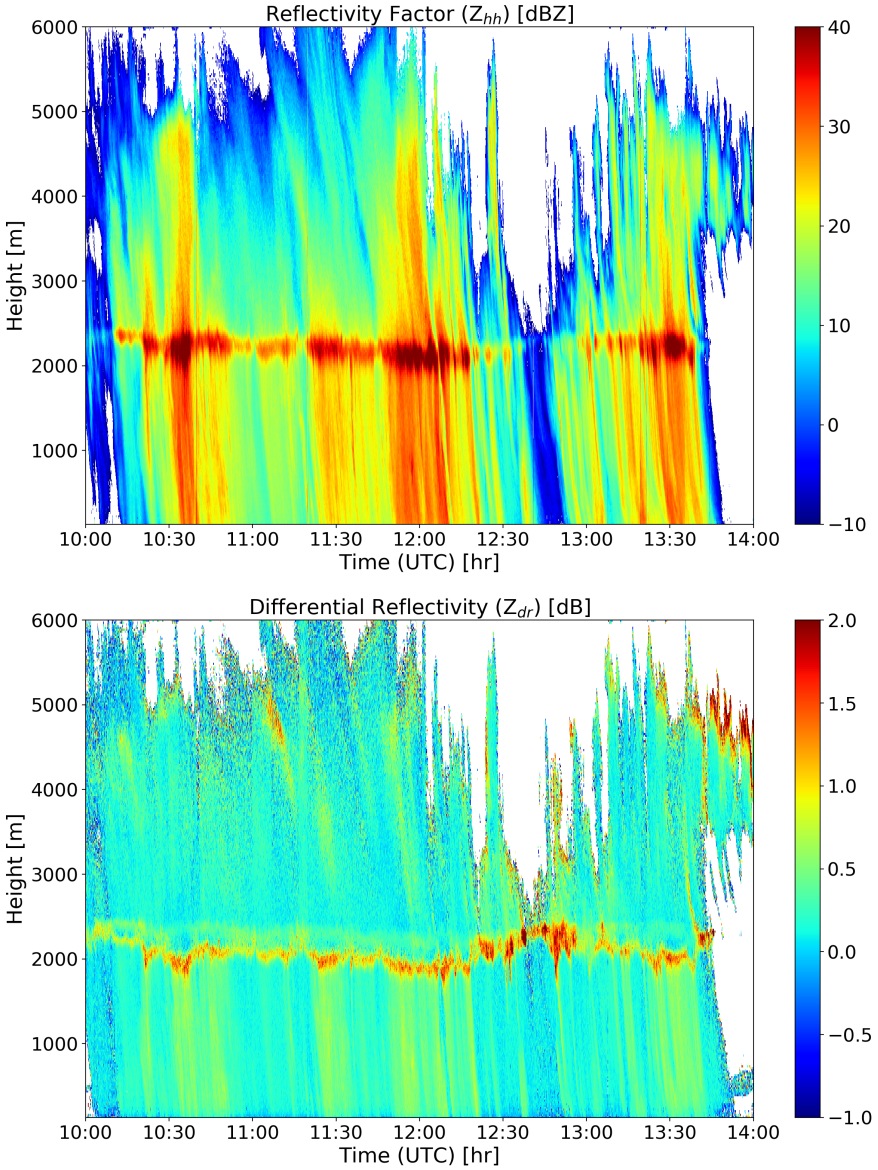
Figure 3.1: Height-time plots (top to bottom) of reflectivity factor [dBZ] and differential reflectivity [dB] on 11 October 2014.

sizes. Event 2 was chosen because it has a relatively stable, well-defined melting layer around 2 km height as shown by the enhanced values of Z_{hh} and Z_{dr} in Figure 3.1 at the top and bottom, respectively. The event also has a relatively low horizontal wind speed, which makes it easier to compare the radar retrievals aloft with the disdrometer measurements on the ground.
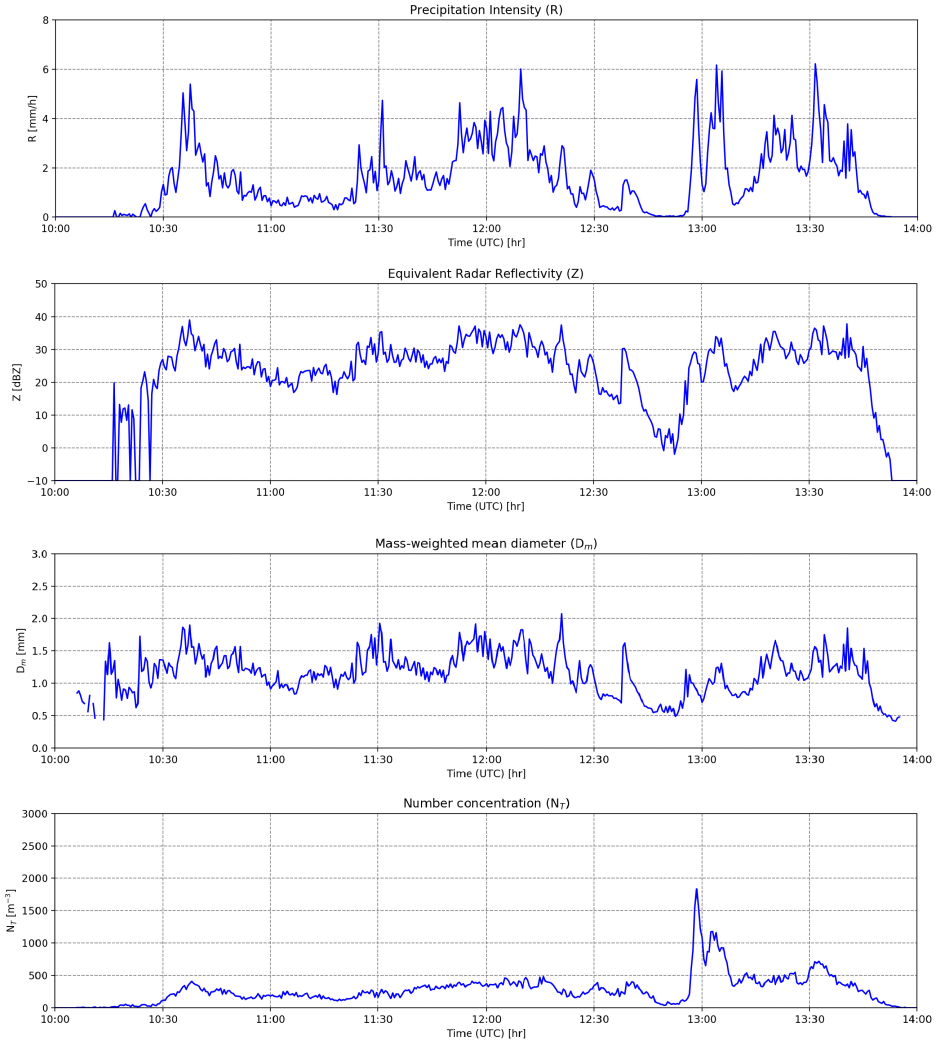
Figure 3.2: Time series of (top to bottom) precipitation intensity (mm h^{-1}), reflectivity factor (dBZ), mass-weighted mean diameter (mm) and number concentration (m^{-3}) from disdrometer data on 11 October 2014.

3.3 Methods

3.3.1 DSD model

The model used to approximate raindrop size distributions (DSDs) in this paper is the gamma distribution proposed by Ulbrich (1983):

$$N(D) = N_0 D^\mu e^{-\Lambda D} = N_T \frac{\Lambda^{\mu+1} D^\mu}{\Gamma(\mu+1)} e^{-\Lambda D}, \tag{3.1}$$

where $N(D)$ is the raindrop size distribution in mm^{-1} m^{-3}, μ is the shape parameter [unitless], Λ is the slope parameter [mm^{-1}], N_0 is the intercept parameter [mm$^{-1-\mu}$ m^{-3}] and N_T is the total number concentration [m^{-3}]. The advantage of N_T over N_0 is that its unit does not depend on μ (Bringi and Chandrasekar, 2001). For convenience, the gamma model is reformulated in terms of the mass-weighted mean diameter D_m [mm] and the generalized intercept parameter N_w [mm^{-1} m^{-3}] (Bringi *et al.*, 2003; Testud *et al.*, 2001) to:

$$N(D) = N_w f(\mu) \left(\frac{D}{D_m} \right)^{\mu} e^{-(4+\mu)\frac{D}{D_m}}, \tag{3.2}$$

where $f(\mu)$, N_w, and D_m are given by:

$$f(\mu) = \frac{6}{4^4} \frac{(\mu+4)^{(\mu+4)}}{\Gamma(\mu+4)}, \tag{3.3}$$

$$N_w = \frac{4^4}{\pi \rho_w} \left(\frac{LWC}{D_m{}^4} \right), \tag{3.4}$$

$$D_m = \frac{4+\mu}{\Lambda}. \tag{3.5}$$

In the equations above, LWC denotes the liquid water content [in g m^{-3}], and ρ_w is the density of liquid water [10^{-3} g mm^{-3}].

It should be mentioned that even though the gamma distribution is the most popular and widely accepted model for representing DSDs in the literature, several studies have questioned its adequacy (Adirosi *et al.*, 2016; Cugerone and De Michele, 2015; Gatidis *et al.*, 2020; Thurai *et al.*, 2019), setting criteria and proposing different tools to check the gamma hypothesis on a case-by-case basis.

3.3.2 Parameter fitting

The best parameters (μ, D_m, and N_w) for describing the DSDs measured by the disdrometer are obtained by using normalized parameterization of the gamma DSD model based on D_m (ratio of 4th to 3rd order moment). To estimate μ, we first calculate D_m and N_w (directly from the measured DSD spectra). The value of μ is determined by testing all possible values of μ between -3 and 15 and choosing the one that minimizes the cost function (CF, Equation 3.6):

$$CF = \sum_{i=3}^{22} | \log_{10}[N_{\text{obs}}(D_i)] - \log_{10}[N(D_i \mid \mu)] |, \tag{3.6}$$

where D_i is the center of the ith diameter class in the Parsivel disdrometer and $N_{\text{obs}}(D_i)$ represents the volumetric size distribution measurements for each diameter class. Note that the index i ranges from 3 to 22 because the first two diameter classes in the Parsivel are always zero and the diameter classes above 22 correspond to particles that are too large to be associated with rain. Finally, we derive Λ through its relationship with D_m and μ (Equation 3.5).

3.3.3 μ-Λ relationship

When an empirical relation between shape and scale parameters is used the gamma model is often called constrained gamma. Note that the term "constrained gamma" denotes a gamma DSD model in which the shape and rate parameters are linked by a deterministic function. Mathematically, this is equivalent to reducing the number of free parameters from three to two, which is convenient in radar-based DSD retrievals. However, the uncertainty related to estimating μ and Λ based on observed DSD spectra remains. Hence, the constrained gamma DSD model and all its associated moments still remain stochastic in nature.

Numerous studies have used and proposed constrained relationships between these two DSD parameters. The most common models are based on second-order polynomial fits, firstly introduced by Zhang *et al.* (2001) and Zhang *et al.* (2003). Since then, several other studies have proposed updated polynomial μ-Λ relationships based on either seasonal (Seela *et al.*, 2018) or regional criteria (Chen *et al.*, 2016). Polynomial models between μ and Λ were also proposed for DSD retrievals using microwave link measurements (Berne and Schleiss, 2009; van Leth *et al.*, 2020). In this study, μ-Λ relationships are modeled using a slightly different power-law model:

$$\Lambda = \alpha(\mu + 3)^{\beta},\tag{3.7}$$

with two coefficients α and β as given in Equation 3.8.

The power-law model above was chosen mainly for mathematical reasons since it ensures that Λ remains positive across all scales and avoids the problem of having to choose between a first-, second- or third-order polynomial. The power-law model is also easier to justify than a parabola from a physical and mathematical point in light of the scale invariance of DSDs under proper normalization, as pointed out by previous researchers (Testud *et al.*, 2001; Torres *et al.*, 1994). However, for the sake of completeness, we also examined the polynomial model during our study and concluded that it did not make a big difference from a practical point of view (i.e., it has similar goodness of fit over the considered range of μ values). Nevertheless, we decided to use the power-law model in this study since it is more appropriate than a polynomial from a theoretical point of view.

Note that the goal of this study is not to question the validity of previous μ-Λ relationships nor optimize the parameters behind them (which depend on the dataset used) but to take a closer look at the sensitivity of the obtained fits to various underlying assumptions. Critical aspects that were investigated include whether the μ-Λ relation remains stable with respect to different sampling resolutions, drop number concentrations, types of stratiform rain events, or the validity of the gamma DSD hypothesis itself. At the same time, one has to keep in mind that the limitation of the Parsivel in terms of the detection of small droplets might lead to overestimated D_m and μ values, since the width of the distribution will be underestimated.

3.3.4 DSD retrieval method

Because the gamma DSD model involves three parameters, three different radar measurements representative of three weighted moments of the DSD are required to retrieve the DSD in a given radar resolution volume. The retrieval method used in this paper is described in Zhang *et al.* (2001). It involves a combination of reflectivity factor at horizontal polarization (Z_{hh}), differential reflectivity (Z_{dr}), and a empirical relationship between the DSD shape parameter (μ) and slope parameter (Λ), commonly referred to as a μ-Λ relationship. The main steps of the retrieval method can be summarized as follows:

1. Impose a μ-Λ relationship $\Lambda = g(\mu)$ based on nearby disdrometer observations or literature values. In our case, a power-law relationship is used:

$$\Lambda = 0.514(\mu + 3)^{1.339}, \tag{3.8}$$

   where the prefactor and exponent were determined by combining all the data from all seven events in Table 3.1.

2. Consider all possible values of μ between -3 and 15 in steps of 0.01. For each μ value, calculate Z_{dr} through Equation 3.9:

$$Z_{dr} = \frac{Z_{hh}}{Z_{vv}} = \frac{\int_0^{D_{max}} N(D)\sigma_{hh}(D)dD}{\int_0^{D_{max}} N(D)\sigma_{vv}(D)dD} = \frac{\int_0^{D_{max}} D^\mu e^{-g(\mu)D}\sigma_{hh}(D)dD}{\int_0^{D_{max}} D^\mu e^{-g(\mu)D}\sigma_{vv}(D)dD} = \frac{h_1(\mu)}{h_2(\mu)}, \tag{3.9}$$

   where σ_{hh} [mm^2] and σ_{vv} [mm^2] are the copolar radar cross-sections of raindrops with equivolume spherical diameter D at horizontal and vertical polarizations, respectively, and D_{max} [mm] is a reasonable maximum drop diameter (e.g., 7 mm in our case). In the literature several studies tried to link D_{max} with D_0 such as Ulbrich and Atlas (1984), who concluded that $D_{max} / D_0 > 2.5$ is what is typically observed in natural rainfall, and Carey and Petersen (2015) who recommended using $D_{max} = 3 \cdot D_0$. The detailed expression of the radar cross-sections can be found in Equation 3 in Unal (2015).

3. Keep the μ value for which the Z_{dr} value in Equation 3.9 is closest to the measured Z_{dr} value by the radar.

4. Infer N_w from Z_{hh} in Equation 3.10, where $\hat{\mu}$ is the retrieved μ value from the previous step:

$$Z_{hh} = N_w \frac{\lambda^4 f(\hat{\mu})}{\pi^5 |K_w|^2} \int_0^{D_{max}} \left(\frac{D}{\hat{D}_m}\right)^{\hat{\mu}} e^{-(4+\hat{\mu})\frac{D}{\hat{D}_m}} \sigma_{hh}(D)dD, \tag{3.10}$$

   where λ is the radar wavelength in millimeters, (i.e., 90.96 mm for TARA), $|K_w|^2$ is the dielectric factor of water, and $\hat{D}_m = \frac{4+\hat{\mu}}{g(\hat{\mu})}$.

5. Retrieve $\hat{N}_T$ by integrating the retrieved DSD:

$$\hat{N}_T = \int\limits_0^{D_{max}} \hat{N}(D)\,dD = \int\limits_0^{D_{max}} \hat{N}_w f(\hat{\mu})\left(\frac{D}{\hat{D}_m}\right)^{\hat{\mu}} e^{-(4+\hat{\mu})\frac{D}{\hat{D}_m}}\,dD. \qquad (3.11)$$

3.4 Analysis of μ-Λ relationship

3.4.1 Variations in μ-Λ relationship from one event to another

In the following, we analyze the variations of the μ-Λ relationships from one event to another. For this, a filter was applied identical to Gatidis *et al.* (2020), and only the cases which satisfied the gamma model hypothesis were considered. The adequacy of the gamma model was assessed based on a combination of a Kolmogorov–Smirnov goodness-of-fit test and Kullback–Leibler divergence. In total, approximately 40% of the DSDs passed the tests and were accepted. On an event-to-event basis, that number varies between 36% and 45%.

In order to investigate and visualize possible differences between events, all seven events were plotted using different colors in Figure 3.3. The overall relationships by Zhang *et al.* (2001) and Zhang *et al.* (2003) were added for comparison. As can be seen in Figure 3.3, most of the event-specific μ-Λ relations stay relatively close to the overall relation, except for events 2 and 6 for which larger deviations for higher values of μ (i.e., $\mu > 8$) are visible. For event 6, the differences can be explained by the limited range of μ, with most values remaining between 3 and 5, and only a single observation falling between 5 and 15. This limited range of variability significantly affects the reliability of the estimated μ-Λ relationship, especially for values smaller than 3 and larger than 5. For event 2, the differences can be explained by the presence of a few outliers in the upper-right part of the scatter plot, corresponding to DSDs with low number concentrations and high sampling uncertainties.

For each selected event, the sample sizes, the fitted power-law parameters α and β, and their percentage relative differences against the overall relation are presented in Table 3.1. The relative errors of the parameters depend on the characteristics of each event, with event 1 being the closest to the overall relation and event 6 exhibiting the largest differences. In order to have a more complete picture of each event, the correlation coefficient between μ and Λ as well as root-mean-square deviation (RMSD) between μ and Λ points of each event and the overall relationship were calculated and are presented in Table 3.1. Even though event 6 has the weakest correlation coefficient, it has the lowest RMSD mainly due to its small sample size (the smallest in the event list) and the way the data are concentrated close to the fitted line. Event 1 shows the strongest relation between μ and Λ, while at the same time event 2 has the highest RMSD because of its outliers in the upper-right part of the scatter plot.

The event-specific and overall μ-Λ relations are clearly different from previously proposed relations by Zhang *et al.* (2001) and Zhang *et al.* (2003). For a fixed μ value, the overall μ-Λ relation for the seven selected events predicts higher Λ values compared with the ones by Zhang *et al.* (2001) and Zhang *et al.* (2003). This can be explained by
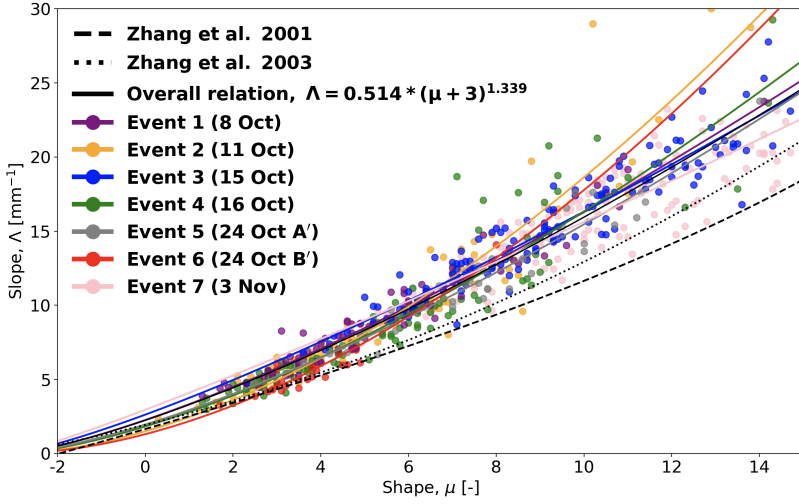
Figure 3.3: Scatter plot between μ and Λ of the selected events colored by event (only gamma DSDs were considered). The μ-Λ relationship of each event was fitted and plotted against the overall relationship. The proposed relations by Zhang *et al.* (2001) and Zhang *et al.* (2003) were plotted as a reference from the literature.

the fact that Λ is inversely proportional to the mass-weighted mean diameter and that the previous relations were derived under different climatological conditions in Florida in the US, where convective rain events with larger raindrops are more common than in the Netherlands.

Although the overall relationship might not necessarily be optimal for each individual event, our results show that it still provides a fairly good approximation of the average μ-Λ relationship across all the seven considered events. Also, one has to keep in mind that the low sample sizes and limited ranges for μ make it practically impossible to derive reliable and representative μ-Λ relations for each individual event. To avoid sampling issues such as those encountered in event 6 and increase the robustness of our results, all remaining sensitivity analyses and retrievals were therefore conducted using the overall μ-Λ relation.

3.4.2 Sensitivity of μ-Λ relationship to gamma hypothesis

One crucial factor that could affect the μ-Λ relationship is the gamma DSD assumption. To investigate this issue, we temporarily added back all DSDs that were excluded from the previous analysis because they did not conform to the gamma model according to the criteria set by Gatidis *et al.* (2020). For each event, we re-calculated the individual μ-Λ relationship and compared the new results to the ones obtained using only the DSDs that satisfied the gamma assumption. In six out of seven cases, the inclusion of the non-gamma cases resulted in larger α and smaller β values. However, these changes were not reflected visually in the μ-Λ scatter plot as the two opposite changes compensate for each other. Therefore, apart from slightly changing the parameter values, the

gamma hypothesis does not appear to have a strong effect on the overall μ-Λ relation. Also, the changes to α (0.518 from 0.514) and β (1.328 from 1.339) were rather small and not statistically significant. The fact that the overall μ-Λ relation is rather stable with respect to the gamma DSD hypothesis is an interesting result, especially given the fact that there are large differences in sample sizes between non-gamma (1829) and gamma DSDs (652).

3.4.3 Sensitivity of μ-Λ relationship to N_T

Using the overall relationship from Section 3.4.1 as a reference, the influence of the number concentration on the μ-Λ relationship was investigated. It would be interesting to investigate whether the events for which the DSD is predominantly number-controlled lead to more or less stable μ-Λ relationships than events with size-controlled DSDs. Three different N_T thresholds corresponding to different percentiles of N_T (25%, 50% and 75%) were applied, and only the DSDs with number concentrations above these thresholds were considered. In Figure 3.4, the three derived μ-Λ relations obtained after applying the N_T filters are shown against the overall relation (no filter). As the N_T threshold is increased from 225 to 300 and 390 m^{-3} (Figures 3.4b, 3.4c, and 3.4d), the μ-Λ relation remains relatively stable for lower μ values, gradually getting closer to the one proposed by Zhang *et al.* (2003), especially for higher values of the shape parameter ($\mu > 7$). This can be partly explained by the fact that, on average, higher N_T values correspond to higher rainfall intensities and larger drop diameters. Also, the average mass-weighted mean diameter increases by approximately 10% as we increase the threshold on N_T. This may not represent a big change, but it can be enough to slightly affect the μ-Λ relation. However, we believe the main reason the μ-Λ relation changes with increasing N_T is sampling uncertainty. Indeed, our dataset predominantly features stratiform rain events with low rainfall intensities, low number concentrations, and relatively low and constant mass-weighted mean diameters (see Table 3.1). As we apply higher thresholds on N_T, the DSD samples that only contain a small number of drops and are associated with a higher sampling uncertainty get removed. Consequently, the remaining DSDs with higher number concentrations tend to be associated with lower sampling uncertainties, which leads to more reliable μ-Λ estimates. Moreover, it is worth pointing out that because of the way μ is estimated through the cost function in Equation 3.6, the error distribution of μ tends to be positively skewed. On average, we are therefore more likely to overestimate μ and underestimate the spread of the DSD rather than the opposite. Since μ and Λ values are positively correlated through their relation with D_m in Equation 3.5, any overestimated μ value automatically results in an overestimated Λ value (to compensate and get the correct D_m). Consequently, as we increase the N_T threshold, sampling errors get reduced and the positively skewed outliers with high μ and Λ values progressively disappear. This removes more and more points on the upper side of the μ-Λ curve, pushing the new relation down towards the one proposed by Zhang *et al.* (2003). Regarding the sensitivity of the α and β parameters describing the μ-Λ relationship, our analyses show that they exhibit an opposite behavior, increasing and decreasing, respectively, as we increase the threshold on N_T. The latter can be attributed to a gradual flattening of the relationship and increase of the intercept parame-

ter. Note that another similar approach to reduce the uncertainty in the estimated μ-Λ relationship without applying a threshold on N_T could be to consider temporal aggregation intervals longer than 30 s. However, this would significantly reduce the amount of data available for analysis.
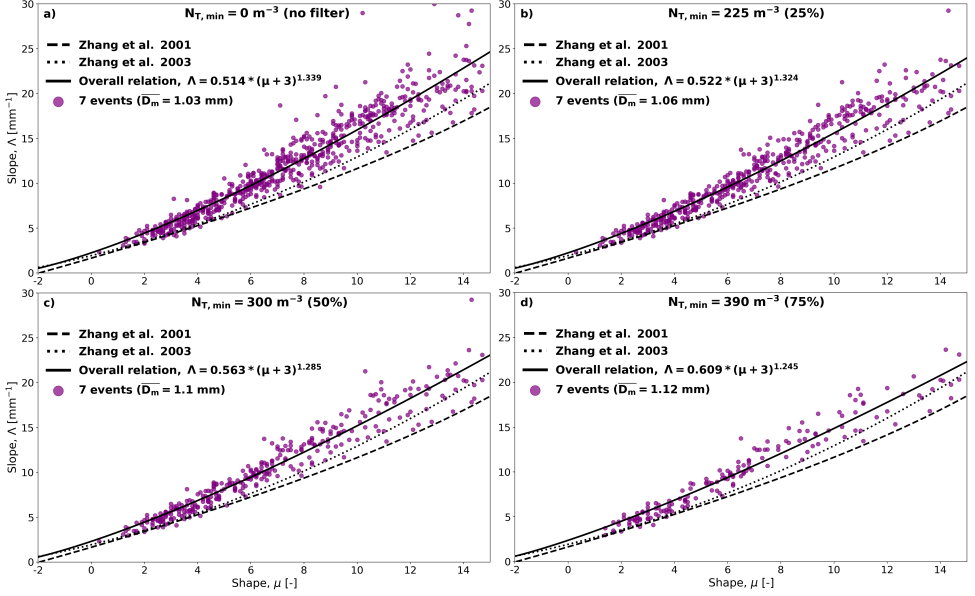

Figure 3.4: Four scatter plots between μ and Λ of the selected events using four different minimum N_T thresholds corresponding to different percentiles of N_T. The μ-Λ relationship of each N_T threshold was fitted and plotted against the proposed relations by Zhang *et al.* (2001) and Zhang *et al.* (2003). a) $N_{T,min}$ = 0 m^{-3} (no filter), b) $N_{T,min}$ = 225 m^{-3}, c) $N_{T,min}$ = 300 m^{-3}, and d) $N_{T,min}$ = 390 m^{-3}.

3.4.4 Influence of sampling resolution on the overall μ-Λ relation

In the following, the DSD data corresponding to the seven selected events were re-sampled at four different temporal resolutions of 30, 60, 240 and 480 s to investigate the sensitivity of the μ-Λ relationship to the choice of the temporal resolution (Figures 3.5a, 3.5b, 3.5c, and 3.5d). Similarly to before, only the re-sampled DSDs which satisfied the gamma hypothesis were kept for analysis. Figure 3.5 shows that the overall μ-Λ relationship remains very stable, regardless of the considered sampling resolution. Table 3.2 shows more details about the fitted power-law parameters α and β at each resolution, including their percentage relative differences against the overall relation at 30-s. We can see that the relative error affecting the parameters slightly increases as the temporal resolution is reduced. The latter can be attributed to the lower number of samples available for fitting the parameters. Apart from these obvious sampling effects, the choice of the temporal aggregation scale seems to have very little effect on the overall μ-Λ relationship, which remains rather stable across multiple aggregation timescales.
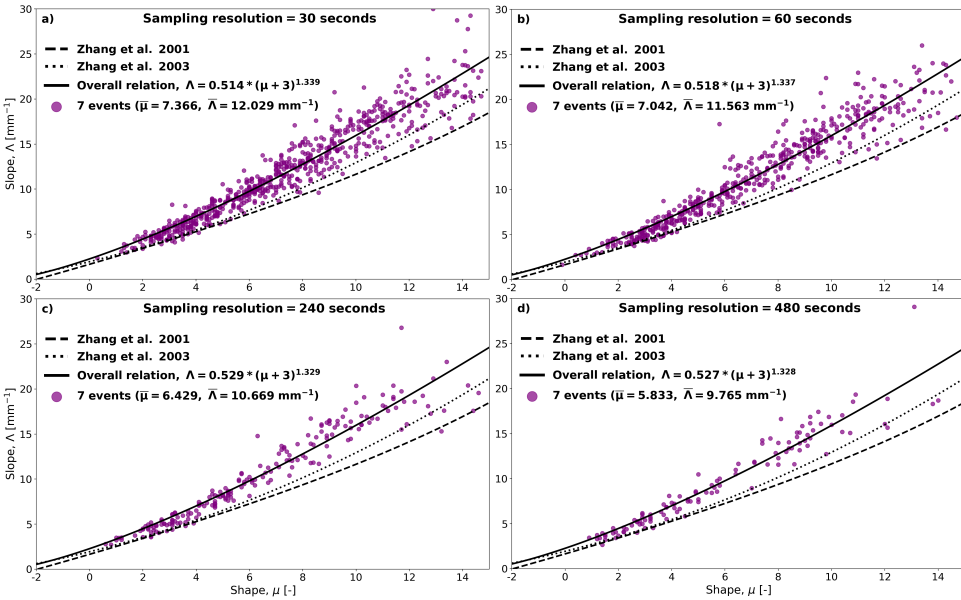
Figure 3.5: Four scatter plots between μ and Λ of the selected events using different resolutions. The μ-Λ relationship of each resolution was fitted and plotted against the proposed relations by Zhang *et al.* (2001) and Zhang *et al.* (2003). a) 30 s, b) 60 s, c) 240 s, and d) 480 s.

Table 3.2: The parameters of the μ-Λ relationship (α, β) for different sampling resolutions and their percentage relative error against the corresponding values at 30 s.

Resolution (sec)	α	Percentage relative error α (%)	β	Percentage relative error β (%)	No. of samples
30	0.514	-	1.339	-	652
60	0.518	0.78	1.337	0.15	519
240	0.529	2.92	1.329	0.75	200
480	0.527	2.53	1.328	0.82	115

Note that as we decrease the temporal resolution, the mean values of μ and Λ (Figure 3.5) also decrease. This means that there is a progressive transition from peaked DSDs at higher sampling resolutions to broader, more widespread DSDs at lower resolutions. Decreasing the sampling resolution therefore causes the μ and Λ values to shift toward the bottom-left part of the scatter plot. However, while the points shift, they remain remarkably close to the initial μ-Λ curve derived at the highest temporal resolution of 30 s. The fact that the μ and Λ values change with resolution but that the overall relation between them is preserved across scales suggests that there is a fundamental physical link between certain moments of the DSD, such as the spread and the mean. Also, this relation seems to be quite robust regardless of whether the gamma assumption is valid or not and is only slightly affected by N_T. In steady rainfall conditions, it should therefore be possible to use the same μ-Λ relationship for DSD retrievals across multiple temporal scales. This is of high importance given the fact that μ-Λ relations are often

used to retrieve DSDs from radar observations, which have different sampling volumes and levels of aggregation than disdrometer data. Moreover, the use of a μ-Λ relationship may still be justified from a physical point of view, even if the underlying DSDs do not strictly comply with the gamma distribution hypothesis. Obviously, the fact that we have selected relatively similar stratiform events with low rainfall intensities and low temporal variability is a crucial factor here since it means that by resampling, we do not significantly change the properties of the DSDs or mix together different rainfall regimes. By contrast, larger differences in μ-Λ relationships can be expected for mixed-type rainfall events with multiple and rapid alternations between stratiform and convective rain.

On the other hand, there is still substantial controversy in the literature around the reason why μ-Λ relations exist in the first place and why certain DSD parameters are linked to each other. One justification could be that the effective number of parameters needed to describe most DSDs is probably fewer than three. In other words, under proper normalization, all DSDs look rather similar to each other. For example, Torres *et al.* (1994) introduced a single DSD normalization technique based on one reference moment (usually the rain rate). Later, Testud *et al.* (2001) and Lee *et al.* (2004) proposed a more general normalization technique based on two reference moments (usually the 3rd and 6th moments). The existence of a μ-Λ relationship may just be the consequence of such scaling laws. In their study, Moisseev and Chandrasekar (2007) have also argued that data filtering can have a strong influence on the relation itself, leading to spurious links between μ and Λ. However, this is not the case in our study. On the contrary, our results show that when events with similar characteristics are chosen, the overall μ-Λ relationship can be rather stable, barely depending on the different filters applied to the data (e.g., inclusion or exclusion of non-gamma DSDs or minimum threshold for Z_{hh} and Z_{dr}). Other studies have pointed out that the constraints linking μ and Λ during parameter fitting can lead to correlated errors between estimated gamma DSD parameters and biased relations (Moisseev and Chandrasekar, 2007; Williams *et al.*, 2014). Indeed, because of the way we fit μ and Λ through D_m (see Section 3.3.1), the parameters end up being positively correlated with each other. In other words, if μ is overestimated, Λ will also be overestimated because it has to compensate for the bias in μ. To address this, Williams *et al.* (2014) proposed a σ'-D_m relation, wherein σ' is the new mass spectrum standard deviation, defined and constructed to be statistically independent of D_m. Even though their approach seems to lead to smaller biases, our results show that it is also possible to derive reliable μ-Λ relations without defining a new σ, simply by excluding the non-gamma DSDs cases and carefully filtering out DSDs with very low N_T values.

3.5 Sensitivity of DSD retrievals

In this section, the sensitivity of the DSD retrieval method as a whole is evaluated. First, the TARA and Parsivel observations are compared with each other to highlight their differences and understand how possible biases in reflectivity or differential reflectivity affect the accuracy of the retrievals. Then, the sensitivity of the retrieved DSD parameters to different bias corrections, scale corrections, and data filters is quantified, and possible ways to mitigate errors during retrievals are proposed.

3.5.1 Overall agreement between radar and disdrometer

Agreement of Z_{hh} and Z_{dr} observations between TARA and Parsivel

In this section the agreement between the Parsivel and TARA measurements is investigated. For the sake of the comparison between TARA and Parsivel observables, the radar equivalent reflectivity factor derived from disdrometer data was used as the measured reflectivity factor at horizontal polarization ($Z_{hh,Pars}$). As for the differential reflectivity, using Rayleigh scattering, the calculated radar cross-sections of raindrops with equiv-olume spherical diameter D at horizontal and vertical polarization were used (Equation 3.9) for estimating reflectivity at horizontal and vertical polarization, respectively. From those, the differential reflectivity value from the Parsivel ($Z_{dr,Pars}$) can be obtained.

The goal is to quantify how well the measurements of the two sensors agree with each other before the DSD retrievals. Figure 3.6 shows the scatter plots of the reflectivity factor (Z_{hh}, top) and differential reflectivity (Z_{dr}, bottom) from the disdrometer versus TARA at
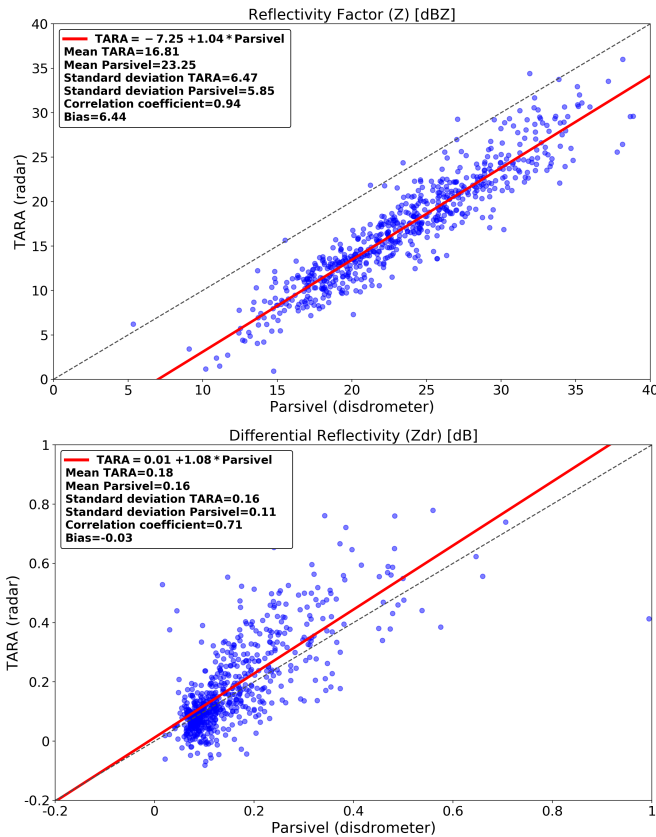

Figure 3.6: Scatter plot between (top to bottom) the observations of Z_{hh} [dBZ] and Z_{dr} [dB] from the disdrometer and the radar.

3

200 m of height. For this first comparison, the Z_{hh} and Z_{vv} measurements of TARA were aggregated (in linear scale) to 30 s in order to be comparable with the disdrometer data. No other additional filter was applied. Figure 3.6, top shows that Z_{hh} measurements are highly correlated (correlation coefficient = 0.94). However, the radar significantly underestimates Z_{hh} compared with the disdrometer. The offset in Z_{hh} slightly varies with time but is of the order of 6 to 7 dBZ (overall bias 6.44 dBZ). Additional bias analyses at a different height of 400 m show that the offset does not change substantially with height, which suggests that the FMCW incomplete beam overlap correction at near ranges (see Section 3.2.2, radar data) works well and that the offset in reflectivity is likely due to calibration issues of TARA rather than range-related issues. Unlike Z_{hh}, the differential reflectivity measurements appear to be in much better agreement with the disdrometer (overall bias -0.03 dB), as can be seen in the bottom panel of Figure 3.6. However, the correlation for Z_{dr} is lower (correlation coefficient = 0.71) and there is significant scatter, especially for higher values of Z_{dr}. Note that the vast majority of Z_{dr} values are small (less than 0.2 dB), which makes sense given that we are mostly dealing with light stratiform rain and that the elevation angle of 45° in TARA further reduces the magnitude of Z_{dr}.

Z_{hh}-Z_{dr} relationships for TARA and Parsivel

In the top panel of Figure 3.7, the Z_{hh}-Z_{dr} relation of each sensor is presented. It shows that most of the time, TARA measures higher Z_{dr} values for a given Z_{hh} than the disdrometer. Once the calibration bias in Z_{hh} is removed (Figure 3.7, bottom), the agreement improves and the radar and disdrometer-derived relationships nicely overlap with each other. Nevertheless, and despite the bias correction, TARA still tends to measure slightly higher Z_{dr} values than the Parsivel for a given Z_{hh}. This can be due to a difference in height or scale between the two measurements. The absence of a clear relation between Z_{hh} and Z_{dr} is not really a problem for the DSD retrieval method itself. In fact, a relation between Z_{hh} and Z_{dr} is not always expected since Z_{hh} depends on N_T, while Z_{dr} does not. However, the fact that TARA and the Parsivel disdrometer exhibit different Z_{hh}-Z_{dr} relationships might negatively impact the accuracy and consistency of the retrieved DSDs.

First DSD retrievals

In the following, we apply the DSD retrieval method described in Section 3.3.4 using Z_{hh} and Z_{dr} measurements from TARA and compare the results to the disdrometer data at 30 s resolution. For the retrievals, we used the overall μ-Λ relationship inferred in Section 3.3.4 (DSD retrieval method) from the disdrometer observations at 30 s sampling resolution.

For illustration purposes, the event on 11 October 2014 was chosen. The time series of retrieved μ, D_m, and N_T as well as observed Z_{hh} and Z_{dr} values for this event are presented in Figure 3.8 and Figure 3.9. Overall, we see that there is rather good agreement in terms of the retrieved μ and D_m values as long as the Z_{dr} values are not too low (i.e., > 0.1 dB). When Z_{dr} is low (e.g., between 12:20 and 13:15 UTC), we see that the retrievals
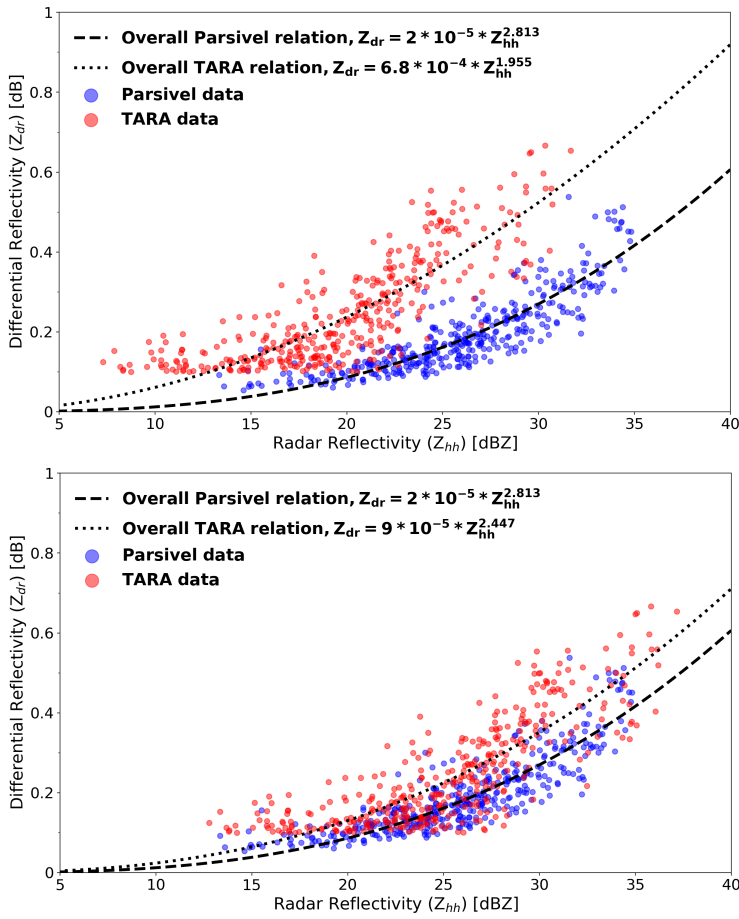
Figure 3.7: Z_{hh}-Z_{dr} relations between the disdrometer and the radar (top to bottom) before and after the calibration bias in Z_{hh} is removed.

become very uncertain, exhibiting much larger fluctuations over time.

Compared with μ, the retrieved N_T values are substantially more uncertain. There are some outliers, and, on average, the retrieved N_T values from TARA are about 100 m^{-3} lower than those from the Parsivel disdrometer (Figure 3.9a). This bias is attributed to the 6-7 dB offset in Z_{hh} in TARA, which propagates non-linearly to N_T through the link between Z_{hh} and N_T in Equations 3.10 and 3.11. On the other hand, we also see some isolated cases in which N_T is overestimated, such as at the beginning (10:57 UTC) and end (13:15 and 13:23 UTC) of the event. These periods are characterized by underestimated Z_{dr} and D_m values by TARA, which, in combination with the relatively high Z_{hh} values, leads to an overestimation of N_T.

For a better overview, the retrieved DSD parameters (μ, D_m, and N_T) for all selected events are plotted against the ones from the disdrometer in Figure 3.10. We can see that the retrieved μ values from the radar tend to be lower compared with the disdrometer.
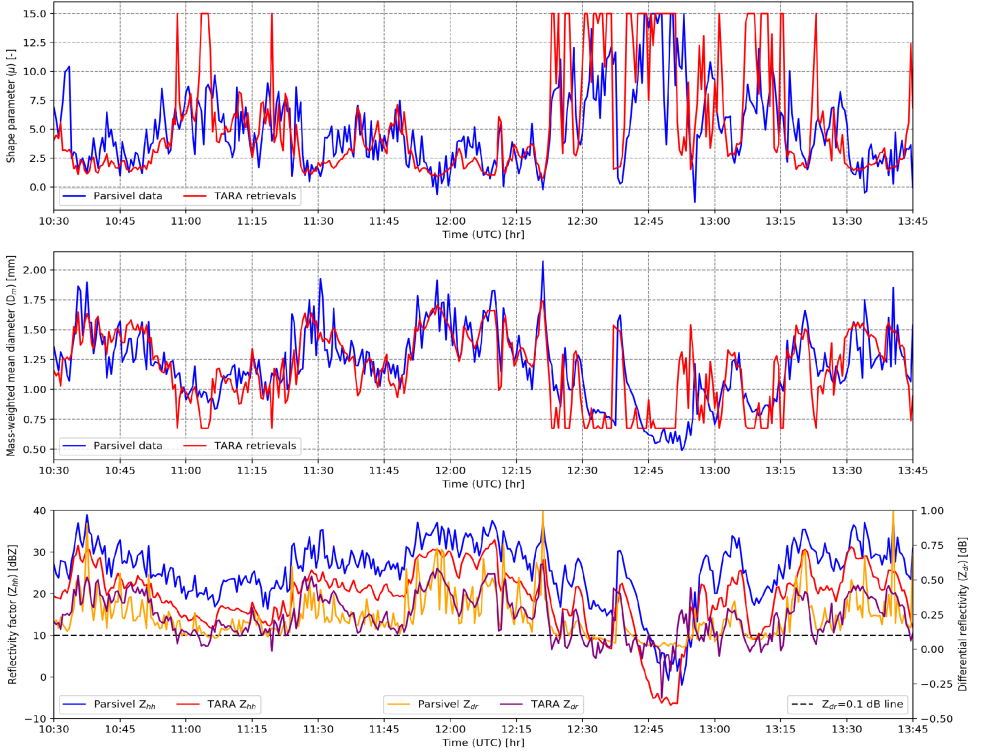
Figure 3.8: Time series of (top to bottom) the DSD retrievals (μ and D_m) as well as Z_{hh} and Z_{dr} observations from the disdrometer and the radar.

The overall bias in the retrieved μ values is 2.11, which is rather large and not immediately apparent from the case study on 11 October (Figure 3.8, top). Note that the retrieved μ values from TARA can never exceed 8 due to the 0.1 dB cutoff applied to Z_{dr} observations (very light rain, peaked DSDs). Because of this, there is a slight conditional bias in the retrieved μ values for low Z_{dr} values. Since μ values are unaffected by the bias in reflectivity and Z_{dr} measurements appear to be well-calibrated, the bias we see in μ values must either be due to the μ-Λ relationship or to differences in scale, height, and measurement principles between the two sensors. Unlike μ, there is better agreement for D_m retrievals with -0.09 overall bias. This holds true for the case study on 11 October as well, for which D_m retrievals from Parsivel and TARA are almost similar throughout the event (Figure 3.8, middle) except for the period between 12:45 and 13:00 UTC when Z_{dr} is low. Looking at the number concentration (Figure 3.10, bottom), we see a significant underestimation in N_T from TARA (overall bias = 276 m^{-3}, multiplicative bias = 4.52), which can be explained by the large 6.44 dBZ bias in Z_{hh} in TARA and is consistent with the previously reported underestimation for the event on 11 October 2014.

Despite the fact that N_T values tend to be underestimated on average, we can also see several large spikes in retrieved N_T values, such as during the second half of the case study event (Figure 3.9a). If we perform a more in-depth analysis of this period
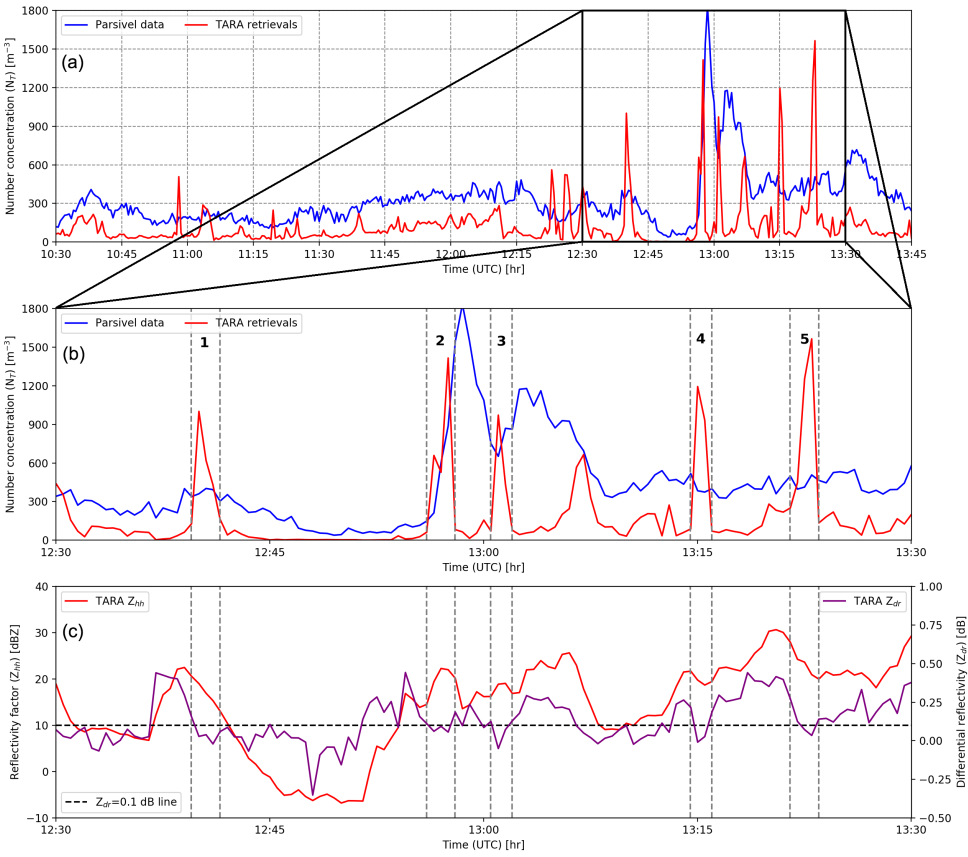
Figure 3.9: Time series of a) the N_T retrievals from the disdrometer and the radar on 11 October 2014, b) the N_T retrievals (zoomed version for the period between 12:30 and 13:30 UTC), c) and the corresponding Z_{hh} and Z_{dr} observations.

(i.e., between 12:30 and 13:30 UTC) in Figure 3.9b and compare it with the Z_{hh} and Z_{dr} observations of the corresponding period (Figure 3.9c), we see that all five spikes in N_T correspond to low values of Z_{dr} and relatively high Z_{hh} values. The low Z_{dr} leads to large μ values and underestimated raindrop sizes during the retrieval. To compensate for this and achieve the correct reflectivity, N_T needs to be increased by a lot. Note that spikes in N_T can still occur even if Z_{hh} is modest or decreasing locally, as long as Z_{dr} is very small; for example, for the spikes 2 and 3 there is a local maximum for Z_{hh}, while for the other spikes the Z_{hh} decreases.

The differences documented above are important because they show that DSD retrievals can be very sensitive to combined biases in Z_{dr} and Z_{hh} relative to each other. The latter can be linked to calibration issues. However, inconsistencies can also arise due to differences in height, sampling volumes and temporal aggregation scales between radar and disdrometer measurements, also known as non-uniform beam-filling problem (Durden and Tanelli, 2008; Ryzhkov, 2007).
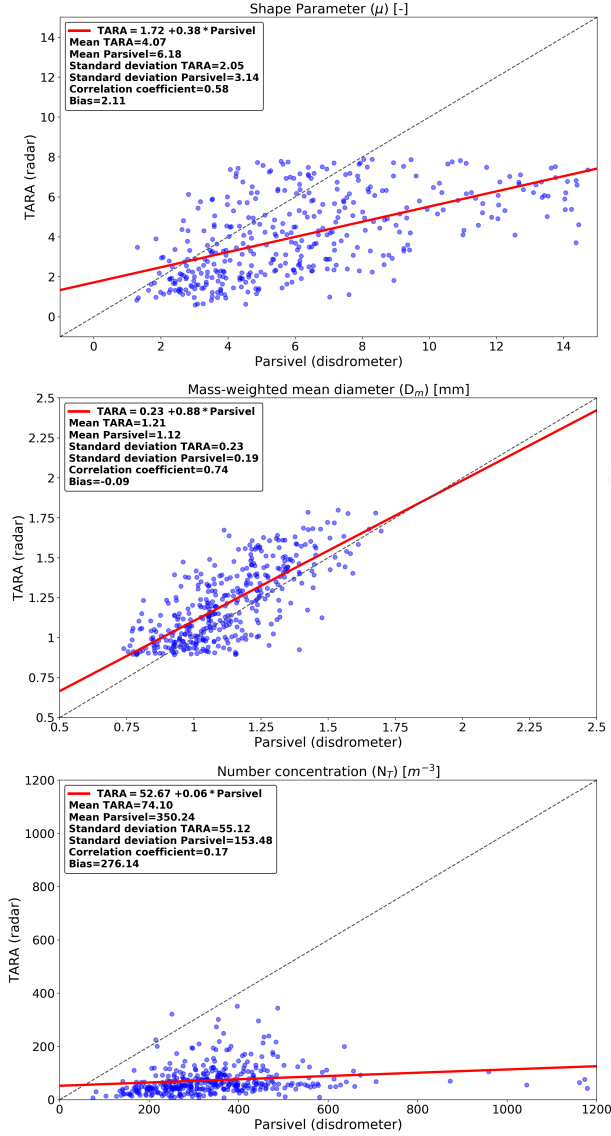
Figure 3.10: Scatter plot of (top to bottom) DSD retrievals (μ, D_m, and N_T) between the radar and disdrometer.

3.5.2 Sensitivity to calibration bias correction

Given the systematic underestimation of the reflectivity factor in TARA, a bias correction was applied before proceeding with the DSD retrievals. Indeed, the bias correction was considered essential to get more reliable results, especially for N_T. Since the N_T retrievals require the reflectivity to be converted from logarithmic [dB] to linear scale [mm^6 m^{-3}], a multiplicative adjustment factor known as the G/R ratio (i.e., the ratio of

the sum of Parsivel to TARA reflectivity values) was used to bias-correct the TARA measurements, treating the disdrometer observations as the reference truth. The value of the G/R ratio was 4.52, which confirmed the large calibration bias of TARA. To address the bias, all TARA reflectivity values (in linear scale) were multiplied by 4.52 and the new DSD parameters were retrieved. As expected, the first two DSD parameters μ and D_m were completely unaffected by the bias adjustment, as they only depend on Z_{dr} (see Section 3.3.4, DSD retrieval method). Figure 3.11, on the other hand, shows that N_T retrievals were substantially improved, and the bias decreased from 276 to 89 m^{-3}. Despite the lower bias, we can see that large uncertainties remain in the retrieved N_T values, as highlighted by the large scatter and frequent outliers.
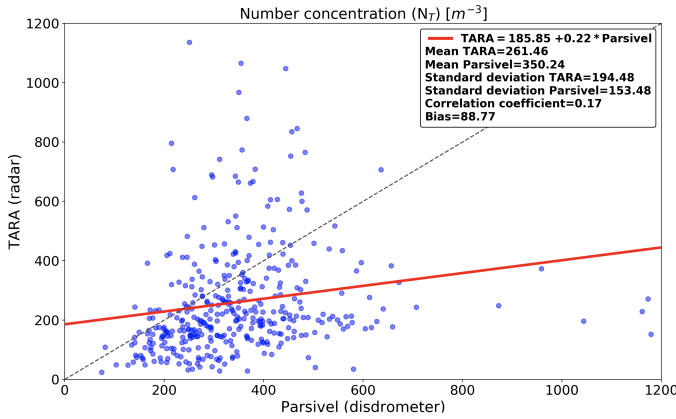
Figure 3.11: Scatter plot of N_T retrievals between the radar and disdrometer after applying the calibration bias correction to Z_{hh}.

3.5.3 Sensitivity to scale bias correction

In the following, a small additional bias adjustment was applied to Z_{dr} to try to account for the large difference in sampling volumes between the TARA radar and the Parsivel disdrometer. This second adjustment is conceptually different from the one applied to Z_{hh}, which was primarily due to calibration issues. Contrarily to Z_{hh}, the differential reflectivity Z_{dr} of TARA is assumed to be well-calibrated. Therefore, the differences in mean and standard deviation are primarily attributed to differences in scale, height, and measurement principles. Note that this scale bias also applies to Z_{hh}. However, for Z_{hh}, the effect is masked by the large calibration bias and the two cannot be separated.

According to Figure 3.6 (bottom), the average Z_{dr} values measured by TARA are 0.03 dB larger than the ones from the Parsivel disdrometer; this makes sense given that the radar sees a larger measurement volume, which makes it more likely to contain at least a few larger drops. Even though a 0.03 dB difference seems small, such a bias can have a significant effect on the DSD retrievals given that the majority of Z_{dr} values are rather small (e.g., between 0.1 and 0.2 dB). A 0.03 dB bias in Z_{dr} therefore represents a relative error of 15-30%.
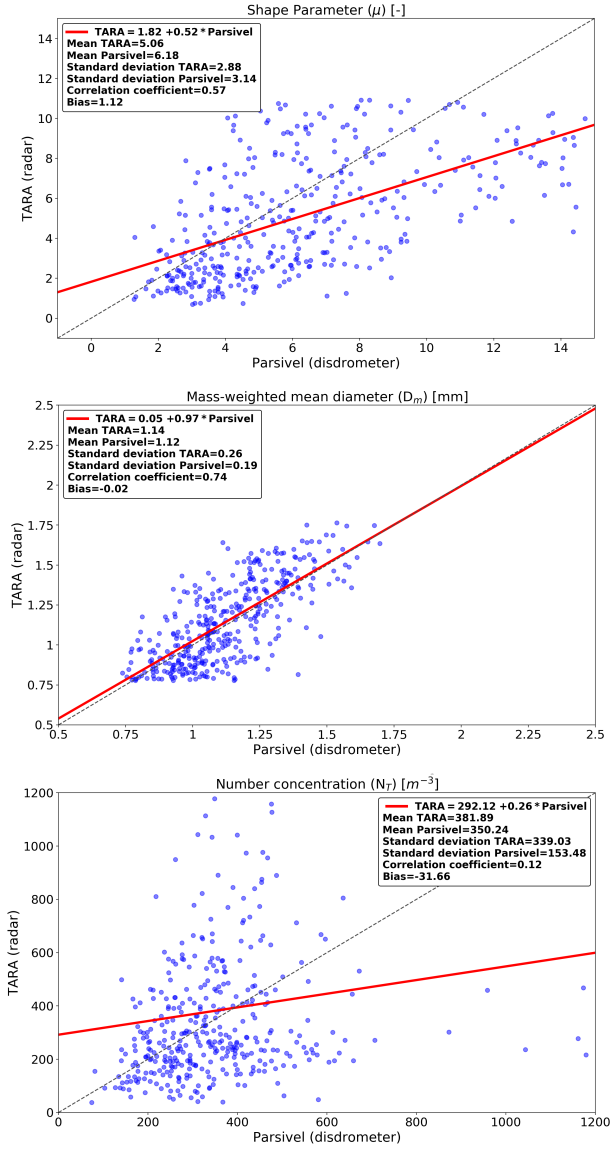
Figure 3.12: Scatter plot of (top to bottom) DSD retrievals (μ, D_m, and N_T) between the radar and disdrometer after applying the scale bias correction to Z_{dr}.

Figure 3.12 shows the retrieved DSD parameters after correcting for the scale bias. We see a reduction of the bias affecting μ and D_m, which are directly linked to Z_{dr}. The bias affecting μ is halved from 2.11 to 1.12, and the bias affecting D_m is reduced from -0.09 to -0.02 mm. The correlation coefficient remains relatively stable, regardless of the scale correction. Despite the improvements for μ and D_m, the N_T retrievals remain

problematic, with a low correlation coefficient of 0.12 (compared to 0.17 without scale bias correction) and moderate bias of -32 m^{-3} (compared to 89 m^{-3} without correction). Also, the average N_T value increased significantly from 261 to 382 m^{-3} (+46%), which highlights the large sensitivity of N_T to changes in the differential reflectivity.

3.5.4 Sensitivity of N_T to outliers

The results presented in the previous sections have shown that, unlike μ and D_m, the uncertainty surrounding the N_T retrievals tends to be much larger. This can be explained by the fact that N_T is the last parameter to be retrieved in Equation 3.11, which makes it more susceptible to error propagation and accumulation during the first steps of the retrieval procedure. Errors in retrieved N_T values can be due to the retrieval method itself (e.g., the assumed μ-Λ relation and gamma DSD model), biased radar observations (e.g., calibration errors in Z_{hh} or/and Z_{dr}), or additional biases due to differences in measurement scale, height, and measurement principle between radars and disdrometers. Considering the fact that the events used in this study mainly consist of weak or light stratiform rain, the errors and uncertainty affecting the measured Z_{dr} values are very likely to play an important role.

The scatter plot of retrieved N_T values versus disdrometer data in Figure 3.10, bottom shows a low correlation coefficient and a significant underestimation from TARA, mainly due to the huge bias in Z_{hh} (6.44 dBZ). However, it is worth noticing that even after applying a calibration bias correction to Z_{hh}, there was no substantial improvement in terms of the N_T retrievals (Figure 3.11). Even though the bias in N_T was reduced (89 m^{-3} compared to 276 m^{-3}), the scatter increased and the correlation coefficient remained low (0.17). The scale correction for Z_{dr} results in even worse agreement (correlation coefficient 0.12; Figure 3.12, bottom). In general, two distinct groups of data points with drastically different error properties can be seen. For the first, the retrieved N_T values are severely overestimated compared to the Parsivel disdrometer by up to 1 order of magnitude. For the second group, the retrieved N_T values are up to 10 times lower than the disdrometer values.

The conclusion is that there are two different types of combinations of Z_{hh}-Z_{dr} that result in unreliable N_T retrievals. The first group is comprised of low Z_{dr} values compared to Z_{hh}, which results in overestimated N_T values. These are all the pairs of Z_{hh}-Z_{dr} in the lower-right part of Figure 3.13. Since Z_{dr} is low, the only way to get a high reflectivity is by increasing N_T. The second group consists of relatively high Z_{dr} values compared to Z_{hh}, which leads to underestimated N_T values. These points correspond to the top-left part of Figure 3.13. Since Z_{dr} is large, the only way to get a low Z_{hh} is to decrease N_T. Together, these two different types of outliers are responsible for the large scatter observed in retrieved N_T values.

Each retrieval has its own uncertainty and error characteristic, depending on the pair of Z_{hh}-Z_{dr}. For example, the scale correction has different impacts on the different subgroups. Even though there is a general increase in N_T to compensate for the new reduced value of Z_{dr}, the aforementioned correction had a significant impact on the subgroup which corresponds to the points that are overestimated by TARA and negligible for the ones that are underestimated.
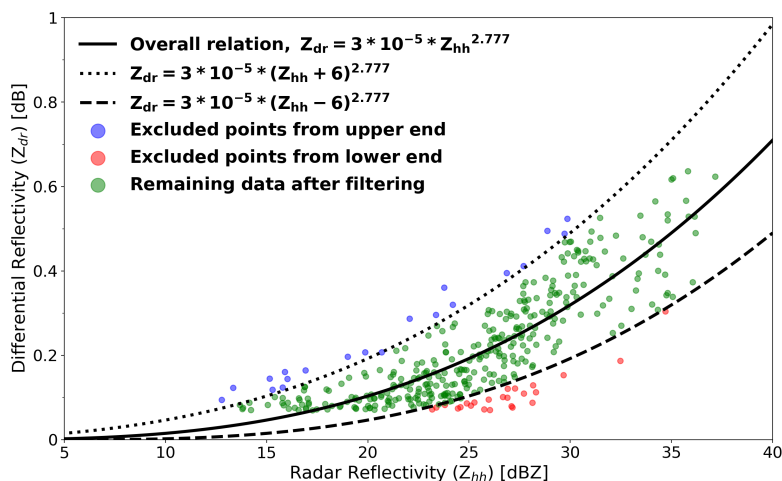
Figure 3.13: Example of the filtering based on the Z_{hh}-Z_{dr} relationship with the overall power-law fit and the corresponding ones for the upper and lower end using $\pm$ 6 dBZ.

Table 3.3: Filter performance (correlation coefficient, bias) of DSD retrievals (μ, D_m, and N_T) for different levels of tolerance ($\pm$ 2, 4, 6, 8, and 10 dBZ).

		correlation coefficient / bias		
$\pm$ dBZ	% of data removed	μ	D_m	N_T
10 (No filter)	0	0.57 / 1.12	0.74 / -0.02	0.12 / -32
8	2.34	0.59 / 1.19	0.75 / -0.02	0.20 / -17
6	8.57	0.60 / 1.14	0.78 / -0.03	0.24 / 10
4	23.12	0.61 / 1.06	0.81 / -0.03	0.21 / 33
2	56.36	0.62 / 1.20	0.85 / -0.03	0.15 / 51

A possible way to reduce the uncertainty affecting the N_T retrievals and thereby avoid large errors is to filter out all potentially problematic combinations of Z_{hh}-Z_{dr}. In the following, a filter which aims to control the uncertainty in N_T by removing certain Z_{hh}-Z_{dr} combinations that are difficult to handle is applied. Note that these "outliers" in the Z_{hh}-Z_{dr} space are not necessarily wrong. They are just problematic in the sense that they can potentially result in very large errors in terms of retrieved N_T. The applied filter is two-dimensional depending on both Z_{hh} and Z_{dr} values since the uncertainty derives from their combination. A power-law model was used to fit the radar observables Z_{hh} and Z_{dr} after calibration and scale bias correction, respectively. Based on that model, an upper and lower curve defining the limits of acceptable Z_{hh} and Z_{dr} pairs is obtained by adding or subtracting a given tolerance from Z_{hh} as in Figure 3.13. For illustration purposes $\pm$ 6 dB was selected, but several other options (i.e., $\pm$ 2, 4, and 8 dB) were examined as well. Table 3.3 lists all options together with their corresponding performances for μ, D_m, and N_T. We see that by removing certain points beyond the lower and upper limits in the Z_{hh}-Z_{dr} space, it is possible to improve the correlation between the observed and

retrieved μ, D_m, and N_T values while keeping a similar bias. For μ and D_m, the best tolerance (in terms of correlation) seems to be $\pm$ 2 dB and $\pm$ 4 dB. However, these are rather strict, which means that a large fraction of the data points would have to be discarded (i.e., 56% and 23%, respectively) for a modest gain in performance. For the N_T retrievals, the optimal tolerance appears to be $\pm$ 6 dB, which discards less than 9% of the data but
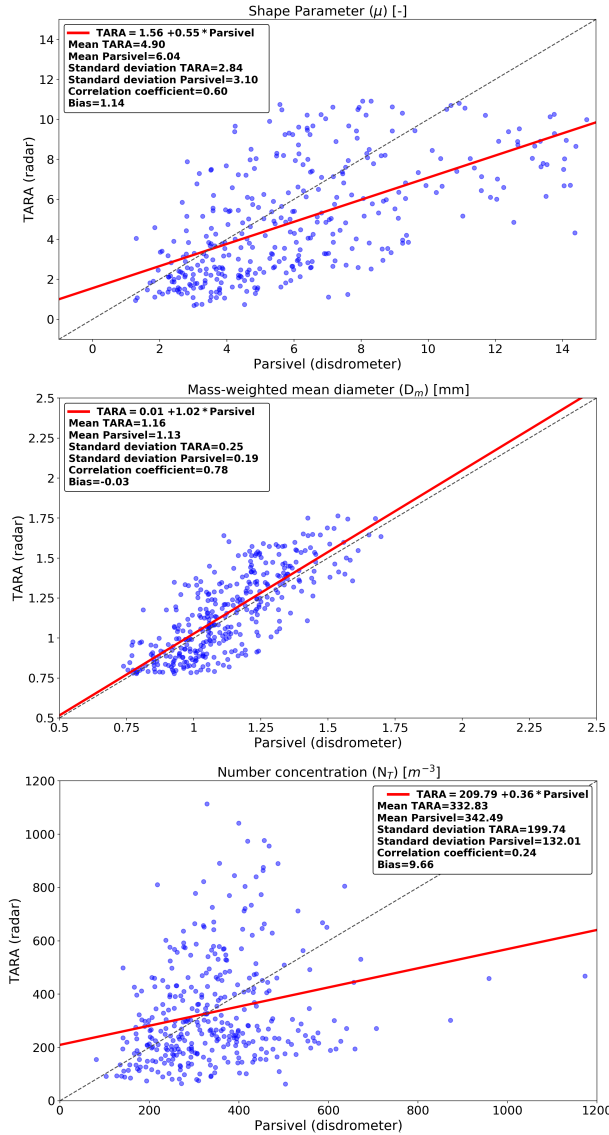

Figure 3.14: Scatter plot of (top to bottom) DSD retrievals (μ, D_m, and N_T) between the radar and disdrometer after applying the Z_{hh}-Z_{dr} relation outlier removal.

still manages to increase the correlation (0.12 to 0.24) and decrease the absolute value of the bias (-32 to 10 m^{-3}). Note that, contrarily to μ and D_m, filtering out more data points does not necessarily increase the performance in terms of the N_T retrievals. Figure 3.14 shows the final radar DSD retrieval results after applying a filter with a tolerance of $\pm$ 6 dB.

3.6 Conclusions

A previously proposed method for retrieving DSDs based on radar reflectivity measurements (Z_{hh}), differential reflectivity (Z_{dr}), and an empirical relation between the shape (μ) and slope (Λ) parameters of a gamma DSD model was investigated. Observations from a nearby optical disdrometer were used to derive the μ-Λ relationship as well as for performing an indirect validation of the retrieved DSDs. While the retrieval method itself is well-known, this study primarily focused on the critical assumptions behind it in order to outline potential sources of errors and uncertainties. First, a thorough sensitivity analysis of the μ-Λ relation to various factors such as the temporal sampling resolution, the adequacy of the gamma model hypothesis, sensitivity to the concentration number (N_T), and event-by-event variations was conducted. Then, the influence of calibration errors in radar observations and scale differences between radar and disdrometer observations were highlighted and investigated. Finally, a filter designed to mitigate uncertainty during N_T retrievals was proposed. According to the results the following conclusions can be drawn.

1. The μ-Λ relationship derived from a nearby disdrometer proved quite robust to the choice of the temporal sampling resolution, validity of the gamma model hypothesis, sample size and event by event variability. However, only seven, rather similar stratiform rain events were considered. More research is necessary to fully understand and quantify inter-event variability of μ-Λ relationships in convective rain.

2. Radar calibration biases significantly affect the accuracy and reliability of the retrieved DSDs. Both Z_{hh} and Z_{dr} must be bias-corrected before retrieving the DSD.

3. Even for well-calibrated radars, a small, additional bias correction to account for the scale difference between radar and disdrometer observations can be useful to reduce conditional biases in retrieved μ and N_T values.

4. Finding the right bias and scale corrections for Z_{hh} and Z_{dr} is not straightforward. Often the bias due to scale differences cannot be separated from the bias due to calibration errors and measurement noise. In our case, Z_{dr} was very well calibrated which allowed us to investigate the scale correction in more detail. However, due to the large calibration offset, the scale correction for Z_{hh} could not be determined.

5. Despite our best efforts, the retrieved N_T values remained highly uncertain. Two different types of outliers were identified, resulting in severely underestimated or

overestimated N_T values. A simple filter for removing outliers in the Z_{hh}-Z_{dr} space was proposed. The filter gets rid of some problematic cases, which slightly improves the reliability of the N_T retrievals. But improvements remained modest and removing more data did not systematically result in better performances.

Finally, it should be mentioned that we do not expect the exact same adjustments to hold for other DSD retrieval algorithms or radar systems. The adjustments mentioned in this study are specific to the TARA radar and Parsivel optical disdrometer. For example, the radar elevation angle was 45°, which is not ideal for such retrievals. Uncertainties for lower elevation angles would probably be smaller due to higher Z_{dr} values. Depending on the radar system, corrections more elaborate than a simple shift in Z_{dr} might be necessary to achieve optimal performance across a larger number of rain events. Similarly, more convective rain events should be included to study the performance and reliability of DSD retrievals based on μ-Λ relationships during heavy convective rain with larger drop sizes. Finally, future work could look at the importance of μ-Λ relations in DSD retrievals from other relevant rainfall sensors, such as satellite observations, which have much larger sampling volumes and errors than ground-based radar and for which the scale corrections might therefore play a more important role.

Power-law μ-Λ relationships in convective and stratiform rainfall

In this study, we take a closer look at the important issue of μ-Λ relationships in raindrop size distributions (DSDs) by conducting a systematic analysis of twenty months of data collected by disdrometers in the Netherlands. A new power-law model for representing μ-Λ relationships based on the double normalization framework is proposed and used to derive separate μ-Λ relationships for stratiform and convective rain events. The sensitivity of the obtained relationships to measurement uncertainty is studied by applying two different quality control filters based on the mass-weighted mean drop diameter (D_m) and liquid water content (LWC). Our results show that there are significant differences in μ-Λ relationships between convective and stratiform rainfall types. However, the retrieved relationships appear to be quite robust to measurement noise and there is good agreement with other reference relations for similar climatological conditions.

4.1 Introduction

The μ-Λ relationship in rainfall microphysics refers to a deterministic function linking the shape (μ) and scale (Λ) parameters of a gamma raindrop size distribution (DSD) model (Zhang *et al.*, 2001). Such relationships are important for understanding the microstructure and dynamics of precipitation and are essential for retrieving DSDs from polarimetric radar measurements. The primary use of μ-Λ relationships in radar remote sensing is to reduce the number of model parameters (from three to two) in DSD retrieval algorithms. However, DSD retrieval remains challenging and subject to various sources of uncertainty, including the accuracy of the remote sensing observations, the limitations of the DSD retrieval algorithms, and the choice of the μ-Λ relationship.

Numerous μ-Λ relationships have been proposed in the literature, with second-order polynomial functions being the most popular. The first relationships were proposed by Zhang *et al.* (2001) and Zhang *et al.* (2003) using DSD data collected in Florida, USA. Since then, several other relationships have been proposed for different datasets and rainfall climatologies. For example, van Leth *et al.* (2020) derived a relationship for the Netherlands using nine months of disdrometer data in Wageningen. Their relationship differs from those reported by Zhang *et al.* (2001) and Zhang *et al.* (2003), which is reasonable given that stratiform rain dominates in the Netherlands and convective and stratiform precipitation have different DSDs. Notably, the drop sizes in convective rain tend to be larger and more variable, which results in a broader DSD with smaller μ and Λ values. Conversely, raindrops in stratiform rain are typically smaller and more uniform in size, corresponding to larger μ values for a given Λ. Vivekanandan *et al.* (2004) pointed out that correlation between μ and Λ exists but may vary across different types of rain, highlighting the need for further understanding of μ-Λ variability. Despite the fact that the μ-Λ relationship changes depending on rain-type, Chu and Su (2008) have shown that μ-Λ relations exhibit similar behavior for small μ values, which usually correspond to heavier rainfall events, while the relations start to deviate as μ and Λ increase, indicating light to moderate rain events.

At the microphysics scale, Bringi *et al.* (2003) showed that a linear relationship with a negative slope exists between the generalized intercept parameter (N_w) in logarithmic scale and the mass-weighted mean diameter (D_m) for stratiform rainfall. For convective rain, two clusters of data emerge, with one cluster consisting of maritime-like convective points and the other of continental-like points. The latter is characterized by larger raindrop sizes and lower concentration, whereas the former exhibits the opposite trend, with a higher concentration of smaller-sized drops.

Similarly, other studies have examined discrepancies in μ-Λ relationships based on either regional (Chen *et al.*, 2016) or seasonal criteria (Seela *et al.*, 2018), showing that both factors are influenced by the prevailing climatic conditions and the dominant rain type. Besides the rain type and climatology, other factors that could potentially affect the μ-Λ relation have also been partially investigated, such as sampling errors (Zhang *et al.*, 2003), temporal sampling resolution, and the adequacy of the gamma model itself (Gatidis *et al.*, 2022). Zhang *et al.* (2003) discussed how sampling errors or deviations from the gamma distribution could result in a correlation between μ and Λ. Using DSD observations of moderate-intensity stratiform rain events in Cabauw, the Netherlands,

Gatidis *et al.* (2022) found that the μ-Λ relationship remained robust regardless of the sampling resolution and the validity of the gamma model.

Another issue that arises when studying μ-Λ relationships is the rainfall classification. Several techniques have been proposed to classify rainfall into stratiform and convective regimes using a variety of different sensors. These methods may include weather radar data, Micro Rain Radar (MRR) vertical profiles, and machine learning models for the bright-band detection (Ghada *et al.*, 2022; Powell *et al.*, 2016; Qi *et al.*, 2013; Romatschke and Dixon, 2022). For example, Yang *et al.* (2019) used a K-nearest neighbor supervised machine learning algorithm for the classification and Doppler radar data to train the model. Other studies use a combination of ground-based sensors like rain gauges or disdrometers and radar data (Bringi *et al.*, 2003; Tokay and Short, 1996; Ulbrich and Atlas, 2007). In this work, the stratiform and convective classification relies primarily on rain intensity estimations by disdrometer, data from a cloud radar, and vertical profiles of reflectivity from an MRR for detecting the melting layer. Additionally, a combination of CAPE and lightning activity data assists in making the final classification decision.

In this paper, we take a closer look at μ-Λ relationships for convective and stratiform rain. A total of twenty months of DSD data were collected in the Netherlands using two co-located Parsivel[2] optical disdrometers. Our analysis starts by applying a quality control filter to D_m and liquid water content (LWC) to discard observations for which the two sensors showed large disagreement. Within the double-moment normalization framework, a new μ-Λ power-law relationship is introduced and fitted to the remaining data, resulting in coefficients with meaningful physical interpretation. Finally, the data are classified into convective and stratiform rain, and differences between the derived μ-Λ relationships are highlighted.

The work is organized as follows. In Section 4.2, we introduce the data used, and in Section 4.3 the methodology is presented. In Section 4.4, the main results for the quality control filter and the μ-Λ relationship analysis for the different rainfall regimes are shown. Finally, the conclusions are provided in Section 4.5.

4.2 Data

The DSD data used in this study were collected by two co-located, perpendicularly oriented Parsivel[2] (Particle Size and Velocity) optical disdrometers (hereafter Parsivel 1 and Parsivel 2) in Cabauw, a polder area located in the western part of the Netherlands between 1 January 2021 and 31 August 2022. The disdrometer data were collected within the framework of the Ruisdael Observatory, a national research infrastructure that consists of a large network of observations and models in the Netherlands where data are merged together to study atmospheric processes across scales and achieve a better understanding of climate change and weather (Russchenberg *et al.*, 2022). The measurement principle and characteristics of the Parsivel[2] have already been extensively described in previous studies (Löffler-Mang and Joss, 2000; Thurai *et al.*, 2011; Tokay *et al.*, 2014) and will not be repeated here. In the past, several studies have highlighted the effect of strong winds on Parsivel data (Friedrich *et al.*, 2013a; Lin *et al.*, 2021), which

could result in unrealistic big raindrops with small fall velocities. Thus, Friedrich *et al.* (2013b) proposed a quality control method for removing all these spurious observations. In the present work even though no action was taken in this direction, the observations from the two co-located sensors were compared to each other. Whenever the agreement between the two sensors was low, the DSDs were removed from the analysis. The total dataset used for this study consisted of 21,178 1-minute DSDs. After filtering, the dataset was reduced to 16,975 DSDs. A detailed description of the filtering process will be given in a following section. No effort was made to investigate the reasons behind the occasional disagreements. The latter have already been extensively studied and documented in the literature and include, among others, errors due to wind, sampling, splashing and internal processing.

In addition to the disdrometer data, the following resources were used for visualization purposes and qualitative precipitation classification:

- Radar data collected by CLARA (CLoud Atmospheric RAdar), a dual-frequency (35-94 GHz) polarimetric scanning cloud radar in Cabauw (https://cloudnet.fmi.fi/search/data?site=cabauw).

- Vertical profiles of reflectivity from an MRR at Cabauw (https://dataplatform.knmi.nl/dataset/ruisdael-mrr-cabauw-2).

- Convective available potential energy from ERA5, ECMWF reanalysis data, (https://doi.org/10.24381/cds.adbb2d47).

- Lightning activity (strikes) from the ZEUS long-range cloud-to-ground lightning detection system (https://www.meteo.gr/talos/en/).

4.3 Methodology

The methodology can be summarized as follows. Firstly, rain events are classified into two types: convective and stratiform. The data from the two co-located disdrometers are then used to fit a gamma model for each 1-min time interval and derive the corresponding shape (μ) and slope (Λ) parameters. The data from the two disdrometers are cross-checked and any time steps for which the two sensors disagree with each other are removed. The remaining data are used to fit the overall μ-Λ relation, as well as the relations for convective and stratiform rainfall types. Finally, the results are compared with those available in the literature to ensure consistency and validity.

4.3.1 DSD model and parameter fitting

The DSD $N(D)$ [mm^{-1} m^{-3}] is modeled using a normalized gamma distribution with shape parameter μ [-], slope Λ [mm^{-1}], and intercept N_w [mm^{-1} m^{-3}] as in Bringi *et al.* (2003) and Testud *et al.* (2001):

$$N(D) = N_w f(\mu) \left(\frac{D}{D_m} \right)^\mu e^{-(4+\mu)\frac{D}{D_m}}, \tag{4.1}$$

$$f(\mu) = \frac{6}{4^4} \frac{(\mu+4)^{(\mu+4)}}{\Gamma(\mu+4)}, \tag{4.2}$$

$$N_w = \frac{4^4}{\pi \rho_w} \left(\frac{LWC}{D_m{}^4} \right), \tag{4.3}$$

$$D_m = \frac{\int_{D_{min}}^{D_{max}} N(D) D^4 \, dD}{\int_{D_{min}}^{D_{max}} N(D) D^3 \, dD} = \frac{4+\mu}{\Lambda}, \tag{4.4}$$

$$LWC = \frac{\pi \rho_w}{6} \int_{D_{min}}^{D_{max}} N(D) D^3 \, dD. \tag{4.5}$$

In the equations above, D_m [mm] is the mass-weighted mean diameter, LWC [g m^{-3}] the liquid water content, ρ_w [10^{-3} g mm^{-3}] the density of liquid water, and D_{min}-D_{max} the integration limits due to the finite range of drop sizes which can occur in nature. This model has been extensively used and assessed in the literature (Gatidis *et al.*, 2020; Thurai *et al.*, 2019). Similarly to Bringi and Chandrasekar (2001), Gatidis *et al.* (2020) and Thurai *et al.* (2014), the method of moments and more particularly the 3rd and 4th DSD moments were used to fit the gamma DSD and estimate the three unknown parameters μ, Λ, and N_w from empirical DSD spectra, with μ values ranging between -3 and 15, as described by Thurai *et al.* (2014). The advantages and disadvantages of the method of moments with respect to other methods such as maximum likelihood estimation were discussed in previous studies (Gatidis *et al.*, 2020; Kliche *et al.*, 2008; Smith and Kliche, 2005; Smith *et al.*, 2009) and will not be repeated here.

4.3.2 μ-Λ relationship

Numerous empirical μ-Λ relationships have been proposed and discussed in the literature (Gatidis *et al.*, 2022; van Leth *et al.*, 2020; Zhang *et al.*, 2003). The most common is the second-order polynomial model proposed by Zhang *et al.* (2001) and Zhang *et al.* (2003):

$$\mu = -0.016\Lambda^2 + 1.213\Lambda - 1.957, \tag{4.6}$$

$$\Lambda = 0.0365\mu^2 + 0.735\mu + 1.935. \tag{4.7}$$

While polynomial relationships are a practical way to represent empirical μ-Λ relationships, they lack theoretical justification, and their coefficients do not have clear physical interpretations. Thus, we propose an alternative model that offers better justification and interpretation. Our model is:

$$\Lambda = \alpha(\mu+3)^\beta(\mu+4)^{1-\beta}, \tag{4.8}$$

where α [mm^{-1}] and β [-] are two model coefficients inferred using a non-linear least-squares fit on pairs of (μ,Λ) values.

Justification

The μ-Λ relationship in Equation 4.8 can be derived from the double-moment normalization framework by Lee *et al.* (2004). In this framework, the DSD is expressed as $N(D) = N_c\, h(\frac{D}{D_c})$ where D_c [mm] is a characteristic drop diameter that depends on two references moments, N_c [mm^{-1} m^{-3}] is a drop number concentration parameter, and h is a template function for describing the shape of the normalized DSD. The two reference moments M_i and M_j used for the normalization depend on the application. In all generality,

$$D_c = \left(\frac{M_j}{M_i}\right)^{\frac{1}{j-i}},$$ (4.9)

$$N_c = M_i^{(j+1)(j-i)} M_j^{(i+1)(i-j)}.$$ (4.10)

To simplify, we consider the special case in which $j = i+1$ and $D_c = M_j\,/\,M_{j-1}$. For example, when j = 4 and i = 3, we get $D_c = M_4\,/\,M_3 = D_m$. If in addition we assume that the DSD is gamma, then we get the model for $N(D)$ as in Equation 4.1.

One key property of the double-moment normalization framework is that any moment M_n of the DSD can be expressed as a power-law of the characteristic drop size D_c:

$$M_n = \int_0^\infty D^n N(D) dD = N_c \xi_n D_c^{n+1},$$ (4.11)

where

$$\xi_n = \int_0^\infty x^n h(x) dx.$$ (4.12)

However, since the DSD variability might not be fully captured by two reference moments, we will assume that

$$M_n = N_c a_n D_c^{b_n},$$ (4.13)

where a_n and b_n are two empirical coefficients which can be slightly different from their theoretical expressions in Equation 4.11. Assuming Equation 4.13 holds, we must have

$$\frac{M_n}{M_{n-1}} = \frac{a_n}{a_{n-1}} D_c^{b_n - b_{n-1}}.$$ (4.14)

Considering that the DSD is assumed to follow a gamma model and given that $\int_0^\infty D^a e^{-bD} dD = \Gamma(a+1)/b^{(a+1)}$ and $\Gamma(a+1) = a\Gamma(a)$, where $\Gamma(a)$ is gamma function, then D_c (the ratio of two successive reference moments with $i = j-1$) is given by:

$$D_c = \frac{M_j}{M_{j-1}} = \frac{\mu + j}{\Lambda}.$$ (4.15)

Combining Equations 4.14 and 4.15 yields:

$$\frac{M_n}{M_{n-1}} = \frac{a_n}{a_{n-1}} \left(\frac{\mu + j}{\Lambda}\right)^{b_n - b_{n-1}}.$$ (4.16)

For a gamma DSD, the left-hand side is: $\frac{\mu+n}{\Lambda}$. Therefore,

$$\frac{\mu+n}{\Lambda} = \frac{a_n}{a_{n-1}} \left(\frac{\mu+j}{\Lambda}\right)^{b_n - b_{n-1}}, \tag{4.17}$$

which can be rewritten as:

$$\Lambda = \alpha_n (\mu+n)^{\beta_n} (\mu+j)^{1-\beta_n}, \tag{4.18}$$

where $\beta_n = (b_{n-1} - b_n + 1)^{-1}$ and $\alpha_n = \left(\frac{a_{n-1}}{a_n}\right)^{\beta_n}$. This leads to a general μ-Λ relationship of the form:

$$\Lambda = \alpha (\mu+n)^{\beta} (\mu+j)^{1-\beta}, \tag{4.19}$$

where α and β depend on the two chosen pairs of consecutive reference moments (M_{j-1}, M_j) and (M_{n-1}, M_n). In particular, if n = 3 and j = 4, then we get $D_c = D_m$ and Equation 4.8, which is the equation we will use in this study. Note that the choice n = j is impossible because it just leads to a self-consistency constraint $D_c = \frac{\mu+4}{\Lambda}$. In other words, for any characteristic drop size D_c, two additional moments are needed to estimate the scaling law linking M_n to D_c.

Equation 4.19 is interesting because it shows that within the framework of double-moment normalization, the relationship between μ and Λ depends on the chosen reference moments used to fit and/or model the DSD. This is a finding that has been previously hinted at by other studies, such as Seifert (2005), but has not been fully explained until now.

4.3.3 DSD filtering

One advantage of having co-located disdrometers is that the DSD measurements can be cross-checked to make sure they are consistent with each other. Suspicious DSDs are identified in a two-step procedure: First, the D_m values for both disdrometers are calculated from the measured DSD spectra. If the absolute value of the difference in D_m values for two co-located measurements exceeds 0.5 mm, both DSD spectra are discarded. The 0.5 mm threshold is inspired by the Global Precipitation Measurement (GPM) mission, which states that D_m should be known to within ± 0.5 mm (Tokay *et al.*, 2020). Then, a second filter that uses a relative error threshold of ± 50% on the LWC between Parsivel 1 and Parsivel 2 is applied. The justification for this second filter can be found in Equation 4.3, which shows the linear relation between N_w and LWC (assuming D_m is known). The use of a relative error threshold means that the DSDs corresponding to low values of LWC (i.e., low rainfall intensities) are filtered more strictly than the DSDs corresponding to moderate and high values of LWC.

4.3.4 Convective-stratiform classification

In the literature, various methods have been introduced for rain type classification, utilizing different datasets, sensors, and techniques. One popular method referred to as

BR03 (Bringi *et al.*, 2003) based on disdrometer data uses the standard deviation of the rain rate over a 10-minute moving time window. If the standard deviation exceeds 1.5 mm h^{-1}, the period is classified as convective; otherwise, it is labeled as stratiform.

Figures 4.1 and 4.2 illustrate the application of the BR03 method to our cloud radar and disdrometer data, respectively, collected in Cabauw on 22 May 2021 during a 3-hour period of stratiform rain. The BR03 method identified two short convective periods within the event. However, the 35 GHz cloud radar co-polar correlation coefficient (ρ_{co}) [-] reveals a distinct melting layer signature throughout the entire event, which contradicts the classification suggested by BR03 (Figure 4.2).
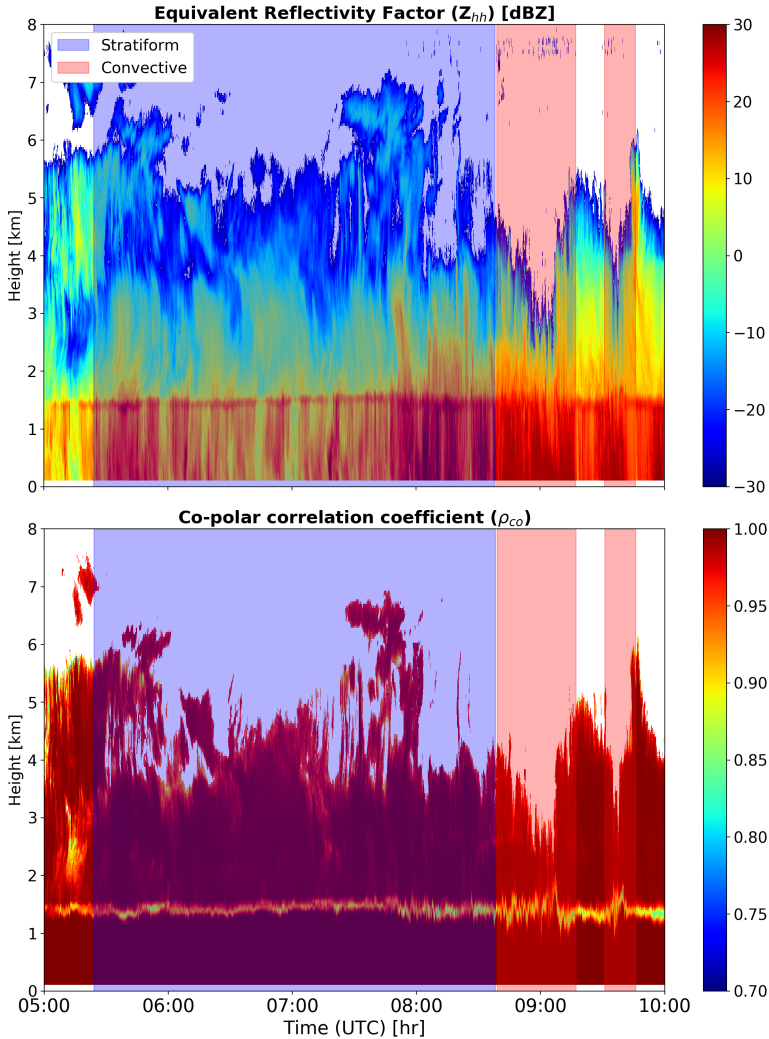
Figure 4.1: Classification of a stratiform event on 22 May 2021 based on the BR03 method. Height–time plots (top to bottom) of reflectivity factor [dBZ] and co-polar correlation coefficient [-] from cloud radar.

To avoid issues with an automated procedure for rain type classification, we manually classified each time period based on the available data sources. To be classified as convective, a time period had to meet the following criteria:

1. Rainfall intensity (by disdrometer) above $10\,\text{mm}\,\text{h}^{-1}$.

2. No melting layer signature in the cloud radar and MRR.

3. Convective available potential energy (CAPE) above 1000 J/kg.

4. Lightning activity around Cabauw.
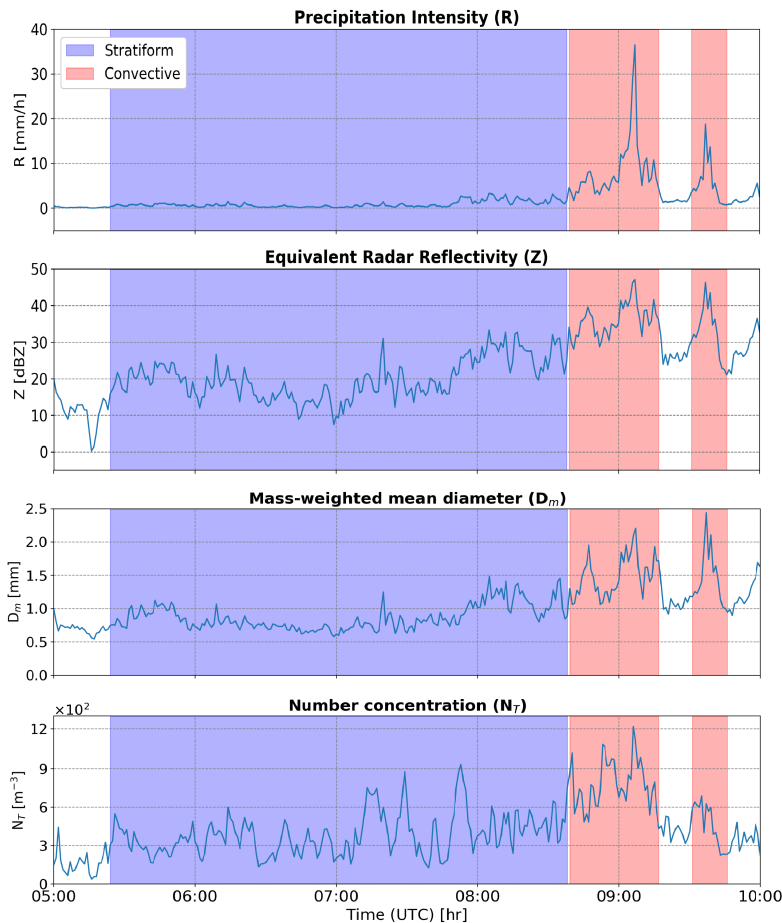
Figure 4.2: Classification of a stratiform event on 22 May 2021 based on the BR03 method. Time series (top to bottom) of precipitation intensity [mm h^{-1}], equivalent reflectivity factor [dBZ] in the Rayleigh scattering regime, mass-weighted mean diameter [mm], and number concentration [m^{-3}] from the disdrometer. Note that after 09:00 UTC there is a peak in rainfall intensity that caused strong attenuation of the cloud radar signal.

To determine the convective events, we start by identifying all 1-min DSD measurements for which the rain rate exceeds 10 mm h^{-1}. We then remove all periods for which there is a clear melting layer signature, since these correspond to stratiform rain. Regarding requirements 3 and 4, please note that no processing was performed on the associated datasets. CAPE and lightning activity are only used as additional diagnostic variables to help with the final classification decision. For the final selection of convective events, only the periods for which the CAPE values were larger than 1000 J/kg and for which lightning strikes were detected over the Cabauw area are kept. A high CAPE level indicates favorable conditions for strong updrafts and storm development, potentially leading to convective rain, while lightning is a phenomenon that can accompany convective storms. However, it is important to state that they are not the exclusive drivers of convective processes (Schumacher *et al.*, 2013). In this study, they are used as an additional indicator for potential convection which together with the high rain intensity and the absence of the melting layer will ensure that no false convective events are identified. The reasoning behind this approach is that we think it is preferable to be too strict and exclude a few convective events rather than being too tolerant and including some stratiform or mixed-type events in the convective dataset.

Table 4.1 presents an overview of the eight convective events that were identified in this way, together with some basic statistics for R, N_w, D_m, and LWC. All eight convective events occurred during late spring and summer and were associated with moist unstable atmospheric conditions (i.e., thermal convection). The average rainfall intensity for the convective events is between 15.1 and 123.1 mm h^{-1}, and the highest intensity occurred on 19 May 2022 (mean LWC of 6.1 g mm^{-3} and average D_m of 2.4 mm).

Table 4.1: Overview of the selected convective events, including the date, number of 1-minute samples, mean ($\overline{x}$) and standard deviation (σ) of rain intensity (R), generalized intercept parameter (N_w), mass-weighted mean diameter (D_m), and liquid water content (LWC). Note that the number of samples denotes the total number of 1-min samples available after filtering (both disdrometers combined).

Event	Date	No. of samples	R ($\overline{x}$ / σ) [mm h^{-1}]	N_w ($\overline{x}$ / σ) [mm^{-1} m^{-3}]	D_m ($\overline{x}$ / σ) [mm]	LWC ($\overline{x}$ / σ) [g m^{-3}]
1	17/08/2022	10	32.4 / 13.5	708.3 / 232.9	2.8 / 0.7	1.4 / 0.5
2	30/06/2022	16	15.2 / 4.5	974.7 / 138.1	1.7 / 0.2	0.9 / 0.2
3	24/06/2022	22	66.1 / 33.6	2604.7 / 341.2	2.4 / 0.4	3.5 / 1.6
4	19/05/2022	9	123.1 / 11.1	4460.4 / 597.2	2.4 / 0.2	6.1 / 0.5
5	05/07/2021	19	16.0 / 3.5	1193.0 / 258.3	1.6 / 0.2	1.0 / 0.2
6	04/07/2021	14	15.1 / 4.1	443.8 / 62.7	2.2 / 0.2	0.7 / 0.2
7	03/07/2021 A'	21	18.8 / 8.2	982.9 / 222.2	1.8 / 0.3	1.0 / 0.3
8	03/07/2021 B'	31	20.9 / 5.5	898.1 / 458.5	2.5 / 0.5	1.0 / 0.3
Overall convective	-	142	30.8 / 29.9	1315.5 / 977.5	2.2 / 0.5	1.6 / 1.5
Overall stratiform	-	16833	1.8 / 3.9	394.3 / 417.4	1.2 / 0.4	0.2 / 0.4

Note that while we are confident that all our convective events were indeed convective, it is likely that some additional cases of convective rainfall were missed and wrongly attributed to the stratiform case because they did not meet all of the requirements mentioned above. However, since the Netherlands experiences predominantly stratiform rainfall, the inclusion of a few convective cases in the stratiform category is likely to have a minimal impact on the results.

4.4 Results

4.4.1 Quality control of DSD data

For the quality control of the DSD data, initially the D_m filter is applied as was described in Section 4.3.3. This first filter substantially reduces the measurement uncertainty affecting the D_m values. The root-mean-square difference (RMSD) of measured D_m values decreases from 0.32 mm to 0.14 mm and the Pearson correlation coefficient increases from 0.53 to 0.88. However, the scatter of $\log_{10}(N_w)$ is still high (RMSD of 0.32 and correlation of 0.70).

Therefore, the second filter on LWC values is used. Figure 4.3 shows the N_w values in logarithmic scale before and after the two filters on D_m and LWC. We can see that the combination of these two filters greatly reduces the scatter. The correlation coefficient increases from 0.70 to 0.86 and the RMSD decreases from 0.32 to 0.16. The LWC filter also slightly improves the agreement of D_m (correlation coefficient increases from 0.88 to 0.90 and RMSD is reduced from 0.14 to 0.12 mm). In total, 19.8% of the DSDs were discarded during the filtering.
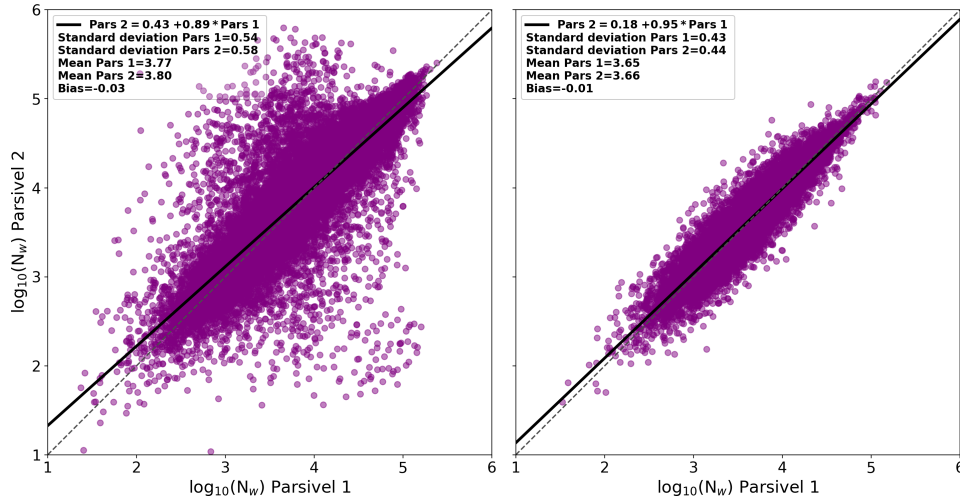
Figure 4.3: Scatter plots of $\log_{10} N_w$ between Parsivel 1 and Parsivel 2 (left to right) before and after the D_m and LWC quality control filter.

4.4.2 Fitted μ-Λ relationships

First, the overall μ-Λ relationship without any distinction for the rainfall type is presented. For this part, all 1-min pairs of (μ,Λ) values from the two disdrometers were combined into a single dataset and the optimal α and β coefficients of the power-law in Equation 4.8 were fitted using non-linear least squares. To assess the effect of the quality control procedure, the analysis was done with and without the D_m-LWC filters.

However, to our surprise, the optimal power-law coefficients (α = 1.632 and β = 5.038) of the μ-Λ relationship with and without filters were almost the same. Similarly, the RMSD values and goodness of fit with and without filters were identical. The results above are highly encouraging, as they suggest that the suspicious DSDs removed during quality control were mainly affected by random noise rather than systematic errors. Consequently, the filters applied did not significantly impact the overall μ-Λ relationship, except for reducing the measurement uncertainty. Furthermore, the μ-Λ relationship for each disdrometer was obtained and then compared. There is relatively good agreement between the two sensors, particularly for smaller μ values ($\mu < 4$) where the RMSD of Λ values is 0.28 mm^{-1}. For cases with μ greater than 4, the RMSD increases to 1.1 mm^{-1}. The slightly bigger differences between the two relations for higher μ values can be explained by the existing sampling uncertainty in the lower rainfall intensities. All of the above implies that a single disdrometer may suffice to derive representative μ-Λ relationships without requiring co-location.

Next, the convective-stratiform classification procedure as described in Section 4.3.4 was applied. Note that for this part of the analysis, only the DSD measurements that passed the D_m-LWC filters were used. The obtained μ-Λ relationships for each rainfall type are presented in Figure 4.4. We can see that there are two clearly different μ-Λ relationships for the stratiform and convective rain events. Although the DSD data for the convective regime originate from eight distinct events, the (μ,Λ) pairs corresponding to them nicely align with each other along the fitted power-law. This is remarkable given that the μ values cover a relatively large range from -1 to 9. However, it should be highlighted that predictions for $\mu > 9$ in convective events should be interpreted very carefully, given that we do not have any observations beyond this range. The data for the stratiform cases also nicely follow the power-law model, albeit with larger scatter. The μ values corresponding to the stratiform cases also cover a larger range of values from -2 up to 15, with the most probable value being between 2 and 6. Note that μ values exceeding 15 are possible but only the DSDs with $\mu < 15$ were used in this study.

The stratiform relationship shows striking similarity to the results obtained by van Leth *et al.* (2020) and Gatidis *et al.* (2020), who also focused on stratiform rain in the Netherlands with low to moderate rainfall intensities. Compared to the convective one, the stratiform relationship predicts higher Λ values for a given μ, which is consistent with lower D_m values. The convective μ-Λ relationship is similar to the ones obtained by Zhang *et al.* (2001) and Zhang *et al.* (2003) in Florida during the summer months in an environment that is prone to convection due to thermal instability and tropical cyclones. It is worth noting that for small μ values ranging from -2 to 4, corresponding to higher rainfall rates, the stratiform and convective relationships exhibit remarkable similarity, reflected in an RMSD of 0.77 mm^{-1} for Λ values. For μ values greater than 4, larger deviations between the two relationships can be noted (RMSD = 4.96 mm^{-1}). The fact that the two relationships diverge for higher μ values can be attributed to the fact that the characteristic drop sizes for a given DSD shape tend to be higher for convective events, which becomes more visible when the DSDs are peaked (i.e., large μ). The fact that the Parsivel struggles to detect small raindrops is unlikely to explain the differences since all suspicious DSDs for which the two co-located disdrometers disagreed with each other were removed prior to analysis.
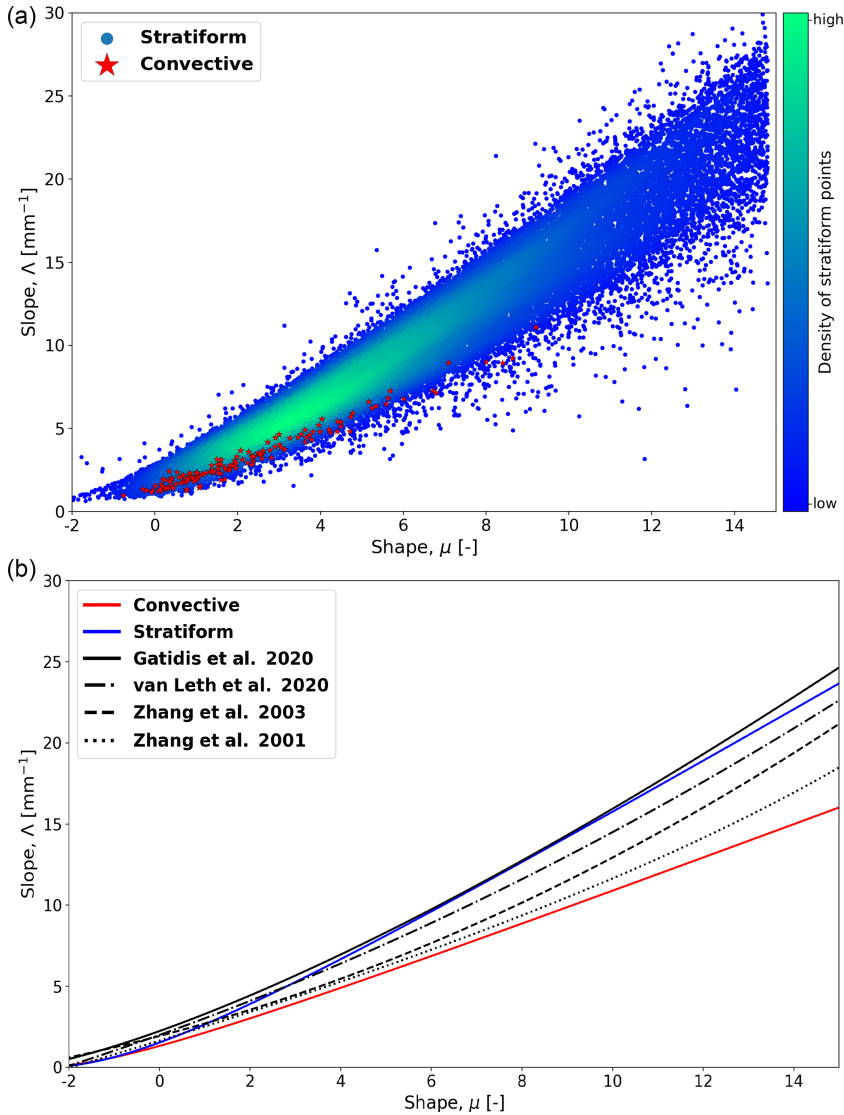
Figure 4.4: a) μ-Λ pairs for convective rain (stars) and stratiform rain (points). The density of stratiform points increases from blue to green. b) μ-Λ relationships for convective and stratiform rain types, together with commonly cited models from the literature.

The significant differences we see between convective and stratiform μ-Λ relationships suggest that choosing a good relationship is key for retrieving physically meaningful and realistic DSDs from polarimetric radar observations, even though the exact consequences of a wrong μ-Λ relation for the DSD retrieval procedure still require further investigation. Using a single, global μ-Λ relationship regardless of the rainfall type could be problematic, especially for lower rainfall rates and very peaked DSDs.

4.5 Conclusions

A study was conducted to analyze μ-Λ relationships in convective and stratiform rainfall in the Netherlands. A total of twenty months of DSD data were collected in Cabauw using two co-located Parsivel[2] optical disdrometers. A quality control filter on D_m and LWC was applied to eliminate periods during which the two disdrometers showed large disagreement. Subsequently, the data from both sensors were combined, and a new μ-Λ power-law relationship based on the double-moment normalization framework was fitted. According to the results the following conclusions can be drawn.

1. The D_m-LWC filter based on two co-located disdrometers substantially reduces the uncertainty affecting the measured DSDs but does not change the μ-Λ relationship. This means that reliable μ-Λ relationships can be obtained using a single disdrometer.

2. The μ-Λ relationships differ significantly between convective and stratiform precipitation, particularly for higher μ and Λ values, which correspond to more peaked DSDs and lower-intensity rainfall (less than 5 mm h^{-1}).

3. The obtained μ-Λ relationships are consistent with other relationships from the literature.

4. The new power-law model looks very similar to previously proposed polynomial models but offers better physical interpretation. For example, Equation 4.19 shows how the order of the moments used to fit the DSD data influences the μ-Λ relationship.

While this study gives further insight into μ-Λ relationships and their differences between stratiform and convective rainfall in the Netherlands, it is still necessary to further investigate the impact of having two clearly different relations during DSD retrievals and whether the correct choice of the relationship matters for a given retrieval algorithm and rainfall intensity. Also, more convective-type events should be considered to get a more representative idea of the natural variability of μ-Λ relations within and between events. Currently, a new extended DSD dataset is being prepared, which is expected to provide further insights into these issues. Finally, a future work could further investigate the characteristics of the discarded DSDs to determine when the two sensors exhibit the most significant differences and under which rainfall regime.

Chapter 5

Conclusions and Outlook

This chapter presents the conclusions that can be drawn from the work discussed in the previous chapters, followed by an outlook of possible future work.

5.1 Conclusions

Precipitation is a profoundly important meteorological process and crucial component of the hydrological cycle. However, accurately measuring rainfall remains notoriously difficult. The complexity of the rainfall field, characterized by strong spatio-temporal variations in raindrop sizes, shapes and concentrations, affects the reliability of remotely-sensed rainfall estimates. The drop size distribution (DSD) plays a crucial role in this context, by offering valuable insights into the microphysical properties of precipitation and linking radar observations to physical quantities such as liquid water content and rainfall rate. However, in most of the cases, the DSD in the radar target volume remains unknown, and simple mathematical models must be used to approximate it. The choice of the DSD model, the mathematical assumptions behind it, and how well the model performs across different spatio-temporal scales can have significant effects on the accuracy of rainfall estimates and DSD retrieval techniques. These issues are often overlooked in the literature.

The objective of this PhD thesis was to better understand the small-scale variability of rain and improve the quantitative estimation of rainfall using weather radar by investigating important aspects linked to the modeling, measurement and retrieval of DSDs. The conclusions are related to the main research questions posed in Chapter 1 (see Section 1.9), which are covered in depth in Chapters 2, 3 and 4 and are briefly listed as follows.

5.1.1 Evaluation of the gamma DSD model

In Chapter 2, the adequacy of the gamma model for representing DSDs was evaluated. Initially, the gamma model was fitted on disdrometer DSD data and a combination of Kolmogorov–Smirnov goodness-of-fit test (K-S test) and Kullback–Leibler divergence (D_{KL}) was used to assess the adequacy of the model. The question was: do DSDs really follow a gamma distribution? **The results show that the majority of DSDs do not strictly follow the gamma model, even though they are well approximated by it. In fact, only 42% of the DSD spectra satisfied the gamma DSD hypothesis. Among these (42%, gamma DSD accepted cases), nearly 79% were not perfectly gamma according to K-S test, but close enough to be approximated by one according to D_{KL}.** The work showed that using the K-S test can be problematic, as results can be strongly affected by sample size. Indeed, the K-S test is more likely to accept the gamma model for DSDs with low drop number concentrations and much more likely to reject it for high drop number concentrations. By contrast, the D_{KL} metric, which mainly focuses on the shape of the distribution, can be used to assess how well the gamma model approximates the empirical distribution. The combination of both metrics leads to a better and more nuanced testing procedure.

Next, the effect of sampling resolution and how it affects the adequacy of the gamma DSD model was investigated. An adaptive sampling algorithm for determining the highest possible resolution at which the gamma hypothesis is adequate was introduced and applied. **For the majority of the cases (around 85%), the gamma model hypothesis was found to be acceptable at resolutions between 30 and 300 s. This means that 15% of the recorded DSD spectra were not well approximated by a gamma model at high temporal resolutions. Among these special cases (15%, non-gamma DSD spectra), one third (around 5.5%) did not comply with the gamma model at any resolution (up to 1800 s).** By testing the gamma model across different time scales, our algorithm can reveal entire periods during which the DSDs are not distributed according to the gamma model, irrespective of the temporal resolution. Our work shows that these periods often correspond to transitions between different rainfall types or regimes. Therefore, in addition to improving DSD modeling and fitting, our method also turns out to be a good way to identify time intervals with interesting rainfall dynamics.

5.1.2 Sensitivity analysis of DSD retrievals based on the μ-Λ relationship

In Chapter 3, a well-known DSD retrieval technique based on polarimetric radar observations was studied. Using DSD observations from a disdrometer, the gamma model was fitted and the μ-Λ relationship was derived. Initially, a sensitivity analysis of the μ-Λ relation to various factors was conducted. **According to the analysis, the relationship was found to be remarkably robust, regardless of the choice of sampling resolution, sample size, inter-event variability, or gamma model hypothesis.**

Then, based on radar data for the same events, the DSD retrieval method was compared against DSD observations from a disdrometer. Various factors contributed to errors and uncertainties during the retrievals, including calibration biases in Z_{hh} and Z_{dr},

measurement noise and differences in scale between the two sensors. According to the analysis, the calibration bias affecting Z_{hh} was large (around a factor of 4.5). **The calibration correction significantly improved the accuracy of the retrieved N_T values, reducing the bias from 276 to 89 m^{-3}. However, determining the scale correction for Z_{hh} turned out to be complicated. The large calibration offset in Z_{hh} meant that the bias due to differences in scale between radar and disdrometer could not be properly determined.** Nonetheless, since Z_{dr} was very well-calibrated, we were still able to correct for the scale difference in retrieved μ values. In the end, we managed to obtain good agreement with the ground measurements for D_m and μ (correlation coefficient of 0.74 and 0.57, respectively), but the retrieved N_T values remained highly uncertain.

5.1.3 Power-law μ-Λ relationships in convective and stratiform rainfall

In Chapter 4, an analysis of the μ-Λ relationship in convective and stratiform rainfall in the Netherlands was conducted. Taking advantage of the fact that the two disdrometers were next to each other, a two-level filter based on the mass-weighted mean drop diameter (D_m) and liquid water content (LWC) was applied to the DSD spectra to remove all suspicious observations. The first level of the quality control removed errors affecting D_m values while the cross-check of the LWC measurements improved the uncertainty associated with the generalized intercept parameter (N_w). **Interestingly, the analyzes showed that the applied filters do not affect the overall μ-Λ relationship but only help reduce the overall scatter due to random noise. This suggests that reliable μ-Λ relationships can be derived using a single disdrometer, despite large measurement uncertainties.**

The main contribution of this third paper was a new power-law model for representing μ-Λ relationships based on the double normalization framework. **The new power-law model is visually very similar to previously proposed second-degree polynomials. However, its coefficients have clear physical meaning, which leads to better interpretation and understanding.** Using the new power-law model, we derived separate μ-Λ relationships for stratiform and convective rainfall events. **The two μ-Λ relationships were consistent with other relationships from the literature and significantly different from each other, especially for high μ and Λ values.** The fact that stratiform and convective events are characterized by different μ-Λ relationships means that we cannot use a single, universal relationship during DSD retrievals. **Most importantly, our research shows that μ-Λ relationships are not a statistical artifact but a natural consequence of the scaling laws linking the different moments of the DSD to each other. These relationships are influenced by multiple factors, including the rainfall type, but also the choice of the DSD model and even the choice of moments used to normalize the DSD.**

5

5.2 Outlook

The work presented in this thesis represents a substantial contribution to the field of DSD modeling and retrieval. Several answers to a number of scientific questions were provided. However, many issues still remain unanswered. In this section, a few recommendations and ideas for further research are given.

In previous sections we discussed the issues affecting DSD retrievals from ground-based weather radars and the different assumptions that we had to make when going from smaller scales to larger ones. Since continuous precipitation monitoring is needed at global scale, this type of research could be further extended to satellite retrievals, e.g., from Global Precipitation Measurement (GPM) mission. In particular, one should take a closer look at the importance of μ-Λ relations and bias corrections in DSD retrievals from GPM, which has a much larger sampling volume and different measurement errors than ground-based radar. For GPM, the scale-related bias corrections in Z_{hh} and Z_{dr} might therefore be more important for retrieving accurate DSDs. Moreover, the spatial scale dependence on the μ-Λ relationship for GPM can be investigated by deploying a large network of spatially distributed disdrometers (other studies have only partially explored this aspect e.g., Adirosi *et al.*, 2021 and Gatlin *et al.*, 2020). Other related activities can involve cases when the GPM sampling volume is heterogeneously filled (e.g., different rainfall types, non-uniform beam-filling).

In Chapters 3 and 4, the importance of μ-Λ relationship for the DSD retrieval was highlighted. A possible step forward could be to conduct a quantitative study on the derived convective and stratiform relations and their influence on the actual DSD retrievals from a polarimetric radar. For example the impact of using the wrong relationship when retrieving DSDs could be studied for different types of rainfall regimes. Furthermore, another recommendation is to study the stability of the μ-Λ relationship across different types of convective events. Indeed, the nature of convective rain is more complicated and chaotic than stratiform events. The strong vertical motions and short-lived convective cells can result in vastly different DSDs, and there might be differences in μ-Λ from one storm to another. In addition, by studying the possible changes in μ-Λ relationship over time, further insights can be gained regarding the physical characteristics that lead to different relations. Based on bulk variables (e.g., rain rate, number concentration etc.) the available data can be stratified into groups. For each group, a unique μ-Λ relationship can be fitted. Then the characterization of each μ-Λ relationship could reveal variables potentially controlling how the relation changes over time.

In Chapter 4, a new power-law model for representing μ-Λ relationships based on double normalization framework was introduced. According to the underlying philosophy of the model, it is possible to establish a relationship as a function of the DSD moments utilized for normalization. Practically, this means that there is a whole family of μ-Λ relationships from which the user can choose one that fits best with the data at hand and intended application. For example, if the radar reflectivity and differential reflectivity are used, two of the normalizing moments should be M_6 and M_7, which will lead to different μ-Λ relations than if we use M_4 and M_3. But other choices are possible and further investigations are necessary to verify this idea and enhance our understanding of the underlying linking mechanism between μ and Λ.

Appendix A

MLE for truncated and binned data

The rescaling of the likelihood function in Equation 2.13 and the theoretical complications that follow from it are heavily dependent on the assumption that the DSD is indeed a gamma distribution, which we know is hardly ever the case. As a result, the corrections are not necessarily beneficial and could actually make the fit worse. To quantify this, we applied the rescaling and truncation to the case study. With this new way of fitting, we saw a drastic decrease in the cumulative acceptance rate up to 5 min from 86.8% to 65.3%. This can be explained if we take into account that most of the spectra of the case study at 30-s resolution are not gamma (according to K-S test only 10% are accepted). Consequently, the correction (rescaling) for the remaining 90% of them was based on the wrong initial hypothesis which led to a worse MLE fit than before.

To investigate this issue further, we applied the new rescaled and truncated MLE fit to the entire DSD dataset at 30-s resolution and we calculated the four bulk variables (R, Z, D_m, N_T) corresponding to the fitted DSDs. Combining them together with the "true" values calculated directly from the disdrometer, we derived the root-mean-square error (RMSE) of the bulk variables for the whole campaign (Table A.1).

Table A.1: Root-mean-square error for the four bulk variables (R, Z, D_m, N_T) at 30-s resolution, for the whole DSD dataset, for the non-gamma DSDs, and for gamma DSDs using MLE for truncated and binned data.

	All DSDs	non-gamma DSDs	gamma DSDs
Rain intensity (R) [mm h^{-1}]	0.89	0.97	0.37
Reflectivity factor (Z) [dBZ]	7.41	7.81	2.63
Mass-weighted mean diameter (D_m) [mm]	0.31	0.34	0.12
Number concentration (N_T) [m^{-3}]	22.27	50.79	9.14

The results show that the RMSE of each variable calculated using the truncated and rescaled MLE increased compared with the values presented in Table 2.3 (MLE without rescaling). The RMSE of the rain intensity increased from 0.75 to 0.89 mm h^{-1}, reflectivity from 3.53 to 7.41 dBZ, D_m from 0.21 to 0.31 mm, and N_T from 3.98 to 22.27 m^{-3}. This

A

is attributed to the fact that most of the time, the DSDs are not strictly gamma. This can be seen very clearly if we calculate the RMSE of the bulk variables separately for all the DSDs which satisfy the gamma assumption (according to our algorithm) and for those which do not (Table A.1). For the gamma shaped DSDs, the truncation and rescaling resulted in lower RMSE values from 0.89 to 0.37 mm h^{-1} for rain intensity, from 7.41 to 2.63 dBZ for reflectivity, from 0.31 to 0.12 mm for mean diameter, and from 22.27 to 9.14 m^{-3} for number concentration. On the other hand, for the non-gamma DSDs the RMSE increased to 0.97 mm h^{-1} for rain intensity, 7.81 dBZ for reflectivity, 0.34 mm for mean diameter, and 50.79 m^{-3} for the number concentration.

All the above shows that the best way to estimate the parameters when we are not sure whether the distribution is really gamma or not is to use:

- Estimates which are based on a few moments calculated directly from the sample (see Table 2.3, RMSE MoM), instead of fitting the whole density function as in MLE.

- Simple numerical solutions which make as little assumptions as possible about the underlying distribution (MLE without rescaling and truncation).

Appendix B

"Exact" K-S test (using Monte Carlo simulations)

An alternative way to apply the K-S test, suitable for cases when population parameters are unknown and must be estimated by sample statistics was implemented. Specifically, we applied the "LcKS" function from the KScorrect package (R programming language), which uses Monte Carlo simulations to estimate the p-values. A total of 4999 random samples (recommended by the authors of the package) were drawn from a gamma distribution with parameters calculated from the sample. Based on these simulations we found that there were no significant changes to the final results. For the study case, the acceptance rates at resolutions between 30 and 300 s differed by less than 1% compared with the previous ones, increasing from 86.8% to 87.3%. Also, because the "exact" K-S test resulted in a lower rejection rate, the left branch of the decision tree was followed slightly more often (from 25%/75% it went to 28%/72%). But overall, no big differences could be observed. This is due to the algorithm construction itself, which is mostly based on the value of D_{KL}. The purpose of the K-S test is mainly to give a first opinion, but the final decision is always based on D_{KL}.

Because there is no significant difference in term of acceptance and rejection rates and because the "exact" K-S test is computationally very expensive and slow, we recommend using the simpler, slightly biased version of the K-S test without Monte Carlo simulations when applying the resampling algorithm.

Appendix C

Sensitivity analysis for C_1 and C_2

A sensitivity analysis was carried out in order to investigate the stability of the acceptance and rejection rates of the gamma hypothesis for different C_1 and C_2 values. A total of four new combinations of C_1 and C_2 values were considered, corresponding to twice/half the original values (see Table C.1). For each combination, the adaptive resampling algorithm was applied at every possible resolution from 30 seconds up to 5 minutes with a step of 30 seconds. The cumulative acceptance rates (up to 5 minutes) and the contributions of the two branches were derived (Table C.1).

Table C.1: Sensitivity analysis of the thresholds C_1 and C_2 (case study only). The impact of different C_1 and C_2 on the cumulative acceptance rates up to 5 min of the gamma DSD hypothesis is assessed. The relative contributions of the left and right branches of the flow-chart are also given. The first combination of C_1 and C_2 values ($C_1 = 0.09$ and $C_2 = 0.05$) is the one used in this study.

C_1 / C_2	Acceptance rate [%]	Accepted both by K-S test and D_{KL} [%]	Rejected by K-S test but accepted by D_{KL} [%]
0.09 / 0.05	86.83	25.12	74.88
0.18 / 0.05	87.07	27.73	72.27
0.045 / 0.05	85.12	23.06	76.94
0.09 / 0.1	94.88	14.91	85.09
0.09 / 0.025	66.59	57.51	42.49

Table C.1 shows that when C_2 is fixed ($C_2 = 0.05$) and we change C_1 (from 0.09 to either 0.18 or 0.045), the results remain relatively stable. The acceptance rate varies by $\pm$ 1% and the left and right branch contributions of the decision tree by $\pm$ 2%. When C_1 is fixed ($C_1 = 0.09$) and C_2 takes different values, the results are more sensitive. When we increase the D_{KL} tolerance (C_2) from 0.05 to 0.1, almost 95% of the cases get accepted, mainly through the right branch of the decision tree (~15/85). However, it should be noted that this specific combination of values ($C_1 = 0.09$ and $C_2 = 0.1$) is not realistic since by definition C_1 should be greater than C_2 to ensure a lower tolerance on D_{KL} in case the K-S test gets rejected. As for the last case where the tolerance on D_{KL} is much lower ($C_2 = 0.025$), we see a drastic drop in the acceptance rate to 66%.

Overall, from the sensitivity analysis we conclude that:

- Values for C_1 and C_2 can be adapted depending on user requirements and application.

- The algorithm is more sensitive on C_2.

- Results depend on the choice of C_1 and C_2. The chosen values for this study are not claimed to be optimal.

C

References

Adirosi, E., Baldini, L., Lombardo, F., Russo, F., Napolitano, F., Volpi, E., and Tokay, A. (2015). Comparison of different fittings of drop spectra for rainfall retrievals. *Advances in Water Resources*, *83*, 55–67. https://doi.org/10.1016/j.advwatres.2015.05.009

Adirosi, E., Volpi, E., Lombardo, F., and Baldini, L. (2016). Raindrop size distribution: Fitting performance of common theoretical models. *Advances in Water Resources*, *96*, 290–305. https://doi.org/10.1016/j.advwatres.2016.07.010

Adirosi, E., Gorgucci, E., Baldini, L., and Tokay, A. (2014). Evaluation of gamma raindrop size distribution assumption through comparison of rain rates of measured and radar-equivalent gamma DSD. *Journal of Applied Meteorology and Climatology*, *53*(6), 1618–1635. https://doi.org/10.1175/jamc-d-13-0150.1

Adirosi, E., Montopoli, M., Bracci, A., Porcù, F., Capozzi, V., Annella, C., Budillon, G., Bucchignani, E., Zollo, A. L., Cazzuli, O., Camisani, G., Bechini, R., Cremonini, R., Antonini, A., Ortolani, A., and Baldini, L. (2021). Validation of GPM rainfall and drop size distribution products through disdrometers in Italy. *Remote Sensing*, *13*(11). https://doi.org/10.3390/rs13112081

Andsager, K., Beard, K. V., and Laird, N. F. (1999). Laboratory measurements of axis ratios for large raindrops. *Journal of the Atmospheric Sciences*, *56*(15), 2673–2683. https://doi.org/10.1175/1520-0469(1999)056%3C2673:lmoarf%3E2.0.co;2

Atlas, D., Srivastava, R. C., and Sekhon, R. S. (1973). Doppler radar characteristics of precipitation at vertical incidence. *Reviews of Geophysics*, *11*(1), 1–35. https://doi.org/10.1029/rg011i001p00001

Atlas, D., and Ulbrich, C. W. (1977). Path- and area-integrated rainfall measurement by microwave attenuation in the 1–3 cm band. *Journal of Applied Meteorology and Climatology*, *16*(12), 1322–1331. https://doi.org/10.1175/1520-0450(1977)016%3C1322:paairm%3E2.0.co;2

Atlas, D., and Ulbrich, C. W. (1990). Early foundations of the measurement of rainfall by radar. *Radar in Meteorology: Battan Memorial and 40th Anniversary Radar Meteorology Conference*, 86–97. https://doi.org/10.1007/978-1-935704-15-7_12

Barthlott, C., Zarboo, A., Matsunobu, T., and Keil, C. (2022). Importance of aerosols and shape of the cloud droplet size distribution for convective clouds and precipitation. *Atmospheric Chemistry and Physics*, *22*(3), 2153–2172. https://doi.org/10.5194/acp-22-2153-2022

Battaglia, A., Rustemeier, E., Tokay, A., Blahak, U., and Simmer, C. (2010). Parsivel snow observations: A critical assessment. *Journal of Atmospheric and Oceanic Technology*, *27*(2), 333–344. https://doi.org/10.1175/2009jtecha1332.1

Battan, L. J. (1973). *Radar observation of the atmosphere*. The University of Chicago Press, 324 pp.

Beard, K. V. (1976). Terminal velocity and shape of cloud and precipitation drops aloft. *Journal of Atmospheric Sciences, 33*(5), 851–864. https://doi.org/10.1175/1520-0469(1976)033%3c0851:tvasoc%3e2.0.co;2

Beard, K. V. (1985). Simple altitude adjustments to raindrop velocities for Doppler radar analysis. *Journal of Atmospheric and Oceanic Technology, 2*(4), 468–471. https://doi.org/10.1175/1520-0426(1985)002%3c0468:saatrv%3e2.0.co;2

Beard, K. V., and Kubesh, R. J. (1991). Laboratory measurements of small raindrop distortion. Part 2: Oscillation frequencies and modes. *Journal of Atmospheric Sciences, 48*(20), 2245–2264. https://doi.org/10.1175/1520-0469(1991)048%3C2245:lmosrd%3E2.0.co;2

Berne, A., Jaffrain, J., and Schleiss, M. (2012). Scaling analysis of the variability of the rain drop size distribution at small scale. *Advances in Water Resources, 45*, 2–12. https://doi.org/https://doi.org/10.1016/j.advwatres.2011.12.016

Berne, A., and Schleiss, M. (2009). Retrieval of the rain drop size distribution using telecommunication dual-polarization microwave links. *American Meteorological Society 34th Conference on Radar Meteorology Proceedings*. https://ams.confex.com/ams/34Radar/techprogram/paper_155668.htm

Brandes, E. A., Zhang, G., and Vivekanandan, J. (2002). Experiments in rainfall estimation with a polarimetric radar in a subtropical environment. *Journal of Applied Meteorology, 41*(6), 674–685. https://doi.org/10.1175/1520-0450(2002)041%3c0674:eirewa%3e2.0.co;2

Bringi, V. N., and Chandrasekar, V. (2001). *Polarimetric doppler weather radar: Principles and applications*. Cambridge University Press, 662 pp. https://doi.org/10.1017/cbO9780511541094

Bringi, V. N., Chandrasekar, V., Hubbert, J., Gorgucci, E., Randeu, W. L., and Schoenhuber, M. (2003). Raindrop size distribution in different climatic regimes from disdrometer and dual-polarized radar analysis. *Journal of the Atmospheric Sciences, 60*(2), 354–365. https://doi.org/10.1175/1520-0469(2003)060%3C0354:rsdidc%3E2.0.co;2

Bringi, V. N., Huang, G.-J., Chandrasekar, V., and Gorgucci, E. (2002). A methodology for estimating the parameters of a gamma raindrop size distribution model from polarimetric radar data: Application to a squall-line event from the TRMM/Brazil campaign. *Journal of Atmospheric and Oceanic Technology, 19*(5), 633–645. https://doi.org/10.1175/1520-0426(2002)019%3C0633:amfetp%3E2.0.co;2

Brussaard, G. (1974). Rain-induced crosspolarisation and raindrop canting. *Electronics Letters, 10*, 411–412(1). https://digital-library.theiet.org/content/journals/10.1049/el_19740328

Caretta, M., Mukherji, A., Arfanuzzaman, M., Betts, R., Gelfan, A., Hirabayashi, Y., Lissner, T., Liu, J., Lopez, G., Morgan, R., Mwanga, S., and Supratid, S. (2022). Water. In *Climate change 2022: Impacts, adaptation and vulnerability. contribution of working group II to the sixth assessment report of the intergovernmental panel on climate change (IPCC)*. Cambridge University Press, 551-712. https://doi.org/10.1017/9781009325844.006

Carey, L. D., and Petersen, W. A. (2015). Sensitivity of C-band polarimetric radar–based drop size estimates to maximum diameter. *Journal of Applied Meteorology and Climatology*, *54*(6), 1352–1371. http://www.jstor.org/stable/26178345

Chambers, J., Cleveland, W., Kleiner, B., and Tukey, P. (1983). *Graphical Methods for Data Analysis, Duxbury*, 410 pp. https://doi.org/10.1201/9781351072304

Chandrasekar, V., and Bringi, V. N. (1987). Simulation of radar reflectivity and surface measurements of rainfall. *Journal of Atmospheric and Oceanic Technology*, *4*(3), 464–478. https://doi.org/10.1175/1520-0426(1987)004%3c0464:sorras%3e2.0.co;2

Chandrasekar, V., Cooper, W. A., and Bringi, V. N. (1988). Axis ratios and oscillations of raindrops. *Journal of Atmospheric Sciences*, *45*(8), 1323–1333. https://doi.org/10.1175/1520-0469(1988)045%3C1323:araoor%3E2.0.co;2

Chen, B., Wang, J., and Gong, D. (2016). Raindrop size distribution in a midlatitude continental squall line measured by thies optical disdrometers over east China. *Journal of Applied Meteorology and Climatology*, *55*(3), 621–634. https://doi.org/10.1175/jamc-d-15-0127.1

Chu, Y.-H., and Su, C.-L. (2008). An investigation of the slope–shape relation for gamma raindrop size distribution. *Journal of Applied Meteorology and Climatology*, *47*(10), 2531–2544. https://doi.org/10.1175/2008jamc1755.1

Cugerone, K., and De Michele, C. (2015). Johnson SB as general functional form for raindrop size distribution. *Water Resources Research*, *51*(8), 6276–6289. https://doi.org/10.1002/2014wr016484

Durden, S. L., and Tanelli, S. (2008). Predicted effects of nonuniform beam filling on GPM radar data. *IEEE Geoscience and Remote Sensing Letters*, *5*(2), 308–310. https://doi.org/10.1109/lgrs.2008.916068

Ekerete, K.-M. E., Hunt, F. H., Jeffery, J. L., and Otung, I. E. (2015). Modeling rainfall drop size distribution in southern England using a Gaussian mixture model. *Radio Science*, *50*(9), 876–885. https://doi.org/10.1002/2015rs005674

Feingold, G., and Levin, Z. (1986). The lognormal fit to raindrop spectra from frontal convective clouds in Israel. *Journal of Applied Meteorology and Climatology*, *25*(10), 1346–1363. https://doi.org/10.1175/1520-0450(1986)025%3c1346:tlftrs%3e2.0.co;2

Findeisen, W., Volken, E., Giesche, A. M., and Brönnimann, S. (2015). Colloidal meteorological processes in the formation of precipitation. *Meteorologische Zeitschrift*, *24*(4), 443–454. https://doi.org/10.1127/metz/2015/0675

Foresti, L., Sideris, I. V., Nerini, D., Beusch, L., and Germann, U. (2019). Using a 10-year radar archive for nowcasting precipitation growth and decay: A probabilistic machine learning approach. *Weather and Forecasting*, *34*(5), 1547–1569. https://doi.org/10.1175/waf-d-18-0206.1

Frech, M., and Hubbert, J. (2020). Monitoring the differential reflectivity and receiver calibration of the German polarimetric weather radar network. *Atmospheric Measurement Techniques*, *13*(3), 1051–1069. https://doi.org/10.5194/amt-13-1051-2020

Friedrich, K., Higgins, S., Masters, F. J., and Lopez, C. R. (2013a). Articulating and stationary Parsivel disdrometer measurements in conditions with strong winds and heavy rainfall. *Journal of Atmospheric and Oceanic Technology*, *30*(9), 2063–2080. https://doi.org/10.1175/jtech-d-12-00254.1

Friedrich, K., Masters, F. J., Kalina, E. A., and Lopez, C. R. (2013b). Drop-size distributions in thunderstorms measured by optical disdrometers during VORTEX2. *Monthly Weather Review*, *141*(4), 1182–1203. https://doi.org/10.1175/mwr-d-12-00116.1

Gatidis, C., Schleiss, M., and Unal, C. (2022). Sensitivity analysis of DSD retrievals from polarimetric radar in stratiform rain based on the μ–Λ relationship. *Atmospheric Measurement Techniques*, *15*(16), 4951–4969. https://doi.org/10.5194/amt-15-4951-2022

Gatidis, C., Schleiss, M., and Unal, C. (2024). A new power-law model for μ–Λ relationships in convective and stratiform rainfall. *Atmospheric Measurement Techniques*, *17*(1), 235–245. https://doi.org/10.5194/amt-17-235-2024

Gatidis, C., Schleiss, M., Unal, C., and Russchenberg, H. (2020). A critical evaluation of the adequacy of the gamma model for representing raindrop size distributions. *Journal of Atmospheric and Oceanic Technology*, *37*(10), 1765–1779. https://doi.org/10.1175/jtech-d-19-0106.1

Gatlin, P. N., Petersen, W. A., Pippitt, J. L., Berendes, T. A., Wolff, D. B., and Tokay, A. (2020). The GPM validation network and evaluation of satellite-based retrievals of the rain drop size distribution. *Atmosphere*, *11*(9). https://doi.org/10.3390/atmos11091010

Ghada, W., Casellas, E., Herbinger, J., Garcia-Benadí, A., Bothmann, L., Estrella, N., Bech, J., and Menzel, A. (2022). Stratiform and convective rain classification using machine learning models and micro rain radar. *Remote Sensing*, *14*(18). https://doi.org/10.3390/rs14184563

Gires, A., Tchiguirinskaia, I., Schertzer, D., and Berne, A. (2015). 2DVD data revisited: Multifractal insights into cuts of the spatiotemporal rainfall process. *Journal of Hydrometeorology*, *16*(2), 548–562. https://doi.org/10.1175/jhm-d-14-0127.1

Gorgucci, E., and Baldini, L. (2009). Analysis of the mean raindrop shape model for dual polarization radar rainfall estimation. *2009 IEEE International Geoscience and Remote Sensing Symposium, 3*, III-113-III–116. https://doi.org/10.1109/igarss.2009.5418064

Gorgucci, E., Baldini, L., and Chandrasekar, V. (2006). What is the shape of a raindrop? An answer from radar measurements. *Journal of the Atmospheric Sciences, 63*(11), 3033–3044. https://doi.org/10.1175/jas3781.1

Gorgucci, E., Chandrasekar, V., Bringi, V. N., and Scarchilli, G. (2002). Estimation of raindrop size distribution parameters from polarimetric radar measurements. *Journal of the Atmospheric Sciences, 59*(15), 2373–2384. https://doi.org/10.1175/1520-0469(2002)059%3C2373:eorsdp%3E2.0.co;2

Gorgucci, E., Scarchilli, G., Chandrasekar, V., and Bringi, V. N. (2001). Rainfall estimation from polarimetric radar measurements: Composite algorithms immune to variability in raindrop shape–size relation. *Journal of Atmospheric and Oceanic Technology, 18*(11), 1773–1786. https://doi.org/10.1175/1520-0426(2001)018%3c1773:refprm%3e2.0.CO;2

Heijnen, S., Ligthart, L., and Russchenberg, H. (2000). First measurements with TARA; An S-band transportable atmospheric radar. *Physics and Chemistry of the Earth, Part B: Hydrology, Oceans and Atmosphere, 25*(10), 995–998. https://doi.org/10.1016/s1464-1909(00)00140-4

Hu, Z., and Srivastava, R. C. (1995). Evolution of raindrop size distribution by coalescence, breakup, and evaporation: Theory and observations. *Journal of Atmospheric Sciences, 52*(10), 1761–1783. https://doi.org/10.1175/1520-0469(1995)052%3C1761:eorsdb%3E2.0.co;2

Hubbert, J., and Pratte, F. (2006). Differential reflectivity calibration for NEXRAD. *2006 IEEE International Symposium on Geoscience and Remote Sensing*, 519–522. https://doi.org/10.1109/igarss.2006.138

Ignaccolo, M., and De Michele, C. (2014). Phase space parameterization of rain: The inadequacy of gamma distribution. *Journal of Applied Meteorology and Climatology, 53*(2), 548–562. https://doi.org/10.1175/jamc-d-13-050.1

Ignaccolo, M., De Michele, C., and Bianco, S. (2009). The droplike nature of rain and its invariant statistical properties. *Journal of Hydrometeorology, 10*(1), 79–95. https://doi.org/10.1175/2008jhm975.1

Imhoff, R. O., Brauer, C. C., Overeem, A., Weerts, A. H., and Uijlenhoet, R. (2020). Spatial and temporal evaluation of radar rainfall nowcasting techniques on 1533 events. *Water Resources Research, 56*(8). https://doi.org/10.1029/2019wr026723

Jaffrain, J., and Berne, A. (2011). Experimental quantification of the sampling uncertainty associated with measurements from Parsivel disdrometers. *Journal of Hydrometeorology, 12*(3), 352–370. https://doi.org/10.1175/2010jhm1244.1

Jameson, A. R., and Kostinski, A. B. (2001). What is a raindrop size distribution? *Bulletin of the American Meteorological Society*, *82*(6), 1169–1178. https://doi.org/10.1175/1520-0477(2001)082%3C1169:wiarsd%3E2.3.co;2

Jiang, H., Sano, M., and Sekine, M. (1997). Weibull raindrop-size distribution and its application to rain attenuation. *IEE Proceedings - Microwaves, Antennas and Propagation*, *144*, 197–200. https://digital-library.theiet.org/content/journals/10.1049/ip-map_19971193

Johnson, R. W., Kliche, D. V., and Smith, P. L. (2011). Comparison of estimators for parameters of gamma distributions with left-truncated samples. *Journal of Applied Meteorology and Climatology*, *50*(2), 296–310. https://doi.org/10.1175/2010jamc2478.1

Johnson, R. W., Kliche, D. V., and Smith, P. L. (2014). Maximum likelihood estimation of gamma parameters for coarsely binned and truncated raindrop size data. *Quarterly Journal of the Royal Meteorological Society*, *140*(681), 1245–1256. https://doi.org/10.1002/qj.2209

Johnson, R. W., Kliche, D. V., and Smith, P. L. (2015). Modeling raindrop size. *Journal of Statistics Education*, *23*(1). https://doi.org/10.1080/10691898.2015.11889725

Joss, J., and Waldvogel, A. (1967). Ein spektrograph für niederschlagstropfen mit automatischer auswertung / a spectrograph for raindrops with automatic interpretation. *Pure and Applied Geophysics*, *68*(1), 240–246. https://doi.org/10.1007/bf00874898

Kliche, D. V., Smith, P. L., and Johnson, R. W. (2008). L-moment estimators as applied to gamma drop size distributions. *Journal of Applied Meteorology and Climatology*, *47*(12), 3117–3130. https://doi.org/10.1175/2008jamc1936.1

Kullback, S., and Leibler, R. A. (1951). On information and sufficiency. *The Annals of Mathematical Statistics*, *22*(1), 79–86. https://doi.org/10.1214/aoms/1177729694

Laio, F. (2004). Cramer-von Mises and Anderson-Darling goodness of fit tests for extreme value distributions with unknown parameters. *Water Resources Research*, *40*(9). https://doi.org/10.1029/2004wr003204

Lee, G. W., and Zawadzki, I. (2005). Variability of drop size distributions: Time-scale dependence of the variability and its effects on rain estimation. *Journal of Applied Meteorology*, *44*(2), 241–255. https://doi.org/10.1175/jam2183.1

Lee, G. W., Zawadzki, I., Szyrmer, W., Sempere-Torres, D., and Uijlenhoet, R. (2004). A general approach to double-moment normalization of drop size distributions. *Journal of Applied Meteorology*, *43*(2), 264–281. https://doi.org/10.1175/1520-0450(2004)043%3C0264:agatdn%3E2.0.co;2

Lin, L., Bao, X., Zhang, S., Zhao, B., and Xia, W. (2021). Correction to raindrop size distributions measured by Parsivel disdrometers in strong winds. *Atmospheric Research*, *260*, 105728. https://doi.org/10.1016/j.atmosres.2021.105728

Löffler-Mang, M., and Joss, J. (2000). An optical disdrometer for measuring size and velocity of hydrometeors. *Journal of Atmospheric and Oceanic Technology, 17*(2), 130–139. https://doi.org/10.1175/1520-0426(2000)017%3C0130:aodfms%3E2.0.co;2

Marshall, J. S., and Palmer, W. M. K. (1948). The distribution of raindrops with size. *Journal of Meteorology, 5*(4), 165–166. https://doi.org/10.1175/1520-0469(1948)005%3C0165:tdorws%3E2.0.co;2

Marshall, J., Hitschfeld, W., and Gunn, K. (1955). Advances in radar weather. *Advances in Geophysics, 2*, 1–56. https://doi.org/10.1016/s0065-2687(08)60310-6

Maur, A. N. A. (2001). Statistical tools for drop size distributions: Moments and generalized gamma. *Journal of the Atmospheric Sciences, 58*(4), 407–418. https://doi.org/10.1175/1520-0469(2001)058<0407:stfdsd>2.0.co;2

McFarquhar, G. M. (2022). Rainfall microphysics. In *Rainfall: Modeling, measurement and applications.* Elsevier, 1-26. https://doi.org/10.1016/b978-0-12-822544-8.00009-3

Michaelides, S., Levizzani, V., Anagnostou, E., Bauer, P., Kasparis, T., and Lane, J. (2009). Precipitation: Measurement, remote sensing, climatology and modeling. *Atmospheric Research, 94*(4), 512–533. https://doi.org/10.1016/j.atmosres.2009.08.017

Mohd Razali, N., and Yap, B. (2011). Power comparisons of Shapiro-Wilk, Kolmogorov-Smirnov, Lilliefors and Anderson-Darling tests. *Journal of Statistical Modeling and Analytics, 2*, 21–33. https://api.semanticscholar.org/CorpusID:18639594

Moisseev, D. N., and Chandrasekar, V. (2007). Examination of the μ-Λ relation suggested for drop size distribution parameters. *Journal of Atmospheric and Oceanic Technology, 24*(5), 847–855. https://doi.org/10.1175/jtech2010.1

Mróz, K., Battaglia, A., Kneifel, S., D'Adderio, L. P., and Dias Neto, J. (2020). Triple-frequency Doppler retrieval of characteristic raindrop size. *Earth and Space Science, 7*(3). https://doi.org/10.1029/2019ea000789

Pfitzenmaier, L., Unal, C. M. H., Dufournet, Y., and Russchenberg, H. W. J. (2018). Observing ice particle growth along fall streaks in mixed-phase clouds using spectral polarimetric radar data. *Atmospheric Chemistry and Physics, 18*(11), 7843–7862. https://doi.org/10.5194/acp-18-7843-2018

Powell, S. W., Houze, R. A., and Brodzik, S. R. (2016). Rainfall-type categorization of radar echoes using polar coordinate reflectivity data. *Journal of Atmospheric and Oceanic Technology, 33*(3), 523–538. https://doi.org/10.1175/jtech-d-15-0135.1

Pruppacher, H. R., and Beard, K. V. (1970). A wind tunnel investigation of the internal circulation and shape of water drops falling at terminal velocity in air. *Quarterly Journal of the Royal Meteorological Society, 96*(408), 247–256. https://doi.org/10.1002/qj.49709640807

Qi, Y., Zhang, J., and Zhang, P. (2013). A real-time automated convective and stratiform precipitation segregation algorithm in native radar coordinates. *Quarterly Journal of the Royal Meteorological Society*, *139*(677), 2233–2240. https://doi.org/10.1002/qj.2095

Ralph, F., Dettinger, M., White, A., Reynolds, D., Cayan, D., Schneider, T., Cifelli, R., Redmond, K., Anderson, M., Gherke, F., Jones, J., Mahoney, K., Johnson, L., Gutman, S., Chandrasekar, V., Lundquist, J., Molotch, N., Brekke, L., Pulwarty, R., . . . Wick, G. (2014). A vision for future observations for western U.S. extreme precipitation and flooding. *Journal of Contemporary Water Research and Education*, *153*(1), 16–32. https://doi.org/10.1111/j.1936-704x.2014.03176.x

Raupach, T. H., and Berne, A. (2015). Correction of raindrop size distributions measured by Parsivel disdrometers, using a two-dimensional video disdrometer as a reference. *Atmospheric Measurement Techniques*, *8*(1), 343–365. https://doi.org/10.5194/amt-8-343-2015

Romatschke, U., and Dixon, M. J. (2022). Vertically resolved convective–stratiform echo-type identification and convectivity retrieval for vertically pointing radars. *Journal of Atmospheric and Oceanic Technology*, *39*(11), 1705–1716. https://doi.org/10.1175/jtech-d-22-0019.1

Rose, C. R., and Chandrasekar, V. (2006). A GPM dual-frequency retrieval algorithm: DSD profile-optimization method. *Journal of Atmospheric and Oceanic Technology*, *23*(10), 1372–1383. https://doi.org/10.1175/jtech1921.1

Russchenberg, H., Apituley, A., and Holzinger, R. (2022). The Ruisdael Observatory: advancing atmospheric science in the Netherlands. *European Meteorological Society Annual Meeting Proceedings*. https://doi.org/10.5194/ems2022-200

Ryzhkov, A. V. (2007). The impact of beam broadening on the quality of radar polarimetric data. *Journal of Atmospheric and Oceanic Technology*, *24*(5), 729–744. https://doi.org/10.1175/jtech2003.1

Ryzhkov, A. V., Schuur, T. J., Burgess, D. W., Heinselman, P. L., Giangrande, S. E., and Zrnic, D. S. (2005). The joint polarization experiment: Polarimetric rainfall measurements and hydrometeor classification. *Bulletin of the American Meteorological Society*, *86*(6), 809–824. https://doi.org/10.1175/bams-86-6-809

Schleiss, M., Berne, A., and Uijlenhoet, R. (2009). Geostatistical simulation of two - dimensional fields of raindrop size distributions at the meso-γ scale. *Water Resources Research*, *45*(7). https://doi.org/10.1029/2008wr007545

Schleiss, M., Chamoun, S., and Berne, A. (2014). Nonstationarity in intermittent rainfall: The "dry drift". *Journal of Hydrometeorology*, *15*(3), 1189–1204. https://doi.org/10.1175/jhm-d-13-095.1

Schönhuber, M., Lammer, G., and Randeu, W. L. (2008). The 2D-video distrometer. In *Precipitation: Advances in measurement, estimation and prediction*. Springer, 3-31. https://doi.org/10.1007/978-3-540-77655-0_1

Schumacher, R. S., Clark, A. J., Xue, M., and Kong, F. (2013). Factors influencing the development and maintenance of nocturnal heavy-rain-producing convective systems in a storm-scale ensemble. *Monthly Weather Review, 141*(8), 2778–2801. https://doi.org/10.1175/mwr-d-12-00239.1

Seela, B. K., Janapati, J., Lin, P.-L., Wang, P. K., and Lee, M.-T. (2018). Raindrop size distribution characteristics of summer and winter season rainfall over north Taiwan. *Journal of Geophysical Research: Atmospheres, 123*(20), 11602–11624. https://doi.org/10.1029/2018jd028307

Seifert, A. (2005). On the shape–slope relation of drop size distributions in convective rain. *Journal of Applied Meteorology, 44*(7), 1146–1151. https://doi.org/10.1175/jam2254.1

Sekelsky, S. M., and Clothiaux, E. E. (2002). Parallax errors and corrections for dual-antenna millimeter-wave cloud radars. *Journal of Atmospheric and Oceanic Technology, 19*(4), 478–485. https://doi.org/10.1175/1520-0426(2002)019%3c0478:peacfd%3e2.0.co;2

Seliga, T. A., and Bringi, V. N. (1976). Potential use of radar differential reflectivity measurements at orthogonal polarizations for measuring precipitation. *Journal of Applied Meteorology, 15*(1), 69–76. https://doi.org/10.1175/1520-0450(1976)015%3c0069:puordr%3e2.0.co;2

Smith, P. L., and Kliche, D. V. (2005). The bias in moment estimators for parameters of drop size distribution functions: Sampling from exponential distributions. *Journal of Applied Meteorology, 44*(8), 1195–1205. https://doi.org/10.1175/jam2258.1

Smith, P. L., Kliche, D. V., and Johnson, R. W. (2009). The bias and error in moment estimators for parameters of drop size distribution functions: Sampling from gamma distributions. *Journal of Applied Meteorology and Climatology, 48*(10), 2118–2126. https://doi.org/10.1175/2009jamc2114.1

Testud, J., Oury, S., Black, R. A., Amayenc, P., and Dou, X. (2001). The concept of "normalized" distribution to describe raindrop spectra: A tool for cloud physics and cloud remote sensing. *Journal of Applied Meteorology, 40*(6), 1118–1140. https://doi.org/10.1175/1520-0450(2001)040%3C1118:tcondt%3E2.0.co;2

Thompson, G., Rasmussen, R. M., and Manning, K. (2004). Explicit forecasts of winter precipitation using an improved bulk microphysics scheme. Part I: Description and sensitivity analysis. *Monthly Weather Review, 132*(2), 519–542. https://doi.org/10.1175/1520-0493(2004)132%3C0519:efowpu%3E2.0.co;2

Thurai, M., Huang, G. J., Bringi, V. N., Randeu, W. L., and Schönhuber, M. (2007). Drop shapes, model comparisons, and calculations of polarimetric radar parameters in rain. *Journal of Atmospheric and Oceanic Technology, 24*(6), 1019–1032. https://doi.org/10.1175/jtech2051.1

Thurai, M., Petersen, W. A., Tokay, A., Schultz, C., and Gatlin, P. (2011). Drop size distribution comparisons between Parsivel and 2-D video disdrometers. *Advances in Geosciences, 30*, 3–9. https://doi.org/10.5194/adgeo-30-3-2011

Thurai, M., Williams, C., and Bringi, V. (2014). Examining the correlations between drop size distribution parameters using data from two side-by-side 2D-video disdrometers. *Atmospheric Research, 144*, 95–110. https://doi.org/10.1016/j.atmosres.2014.01.002

Thurai, M., and Bringi, V. N. (2008). Rain microstructure from polarimetric radar and advanced disdrometers. In *Precipitation: Advances in measurement, estimation and prediction*. Springer, 233-284. https://doi.org/10.1007/978-3-540-77655-0_10

Thurai, M., and Bringi, V. N. (2018). Application of the generalized gamma model to represent the full rain drop size distribution spectra. *Journal of Applied Meteorology and Climatology, 57*(5), 1197–1210. https://doi.org/10.1175/jamc-d-17-0235.1

Thurai, M., Bringi, V., Gatlin, P. N., Petersen, W. A., and Wingo, M. T. (2019). Measurements and modeling of the full rain drop size distribution. *Atmosphere, 10*(1). https://doi.org/10.3390/atmos10010039

Tokay, A., Chamberlain, R., and Schoenhuber, M. (2000). Laboratory and field measurements of raindrop oscillations [First European Conference on Radar Meteorology]. *Physics and Chemistry of the Earth, Part B: Hydrology, Oceans and Atmosphere, 25*(10), 867–870. https://doi.org/10.1016/S1464-1909(00)00117-9

Tokay, A., D'Adderio, L. P., Wolff, D. B., and Petersen, W. A. (2020). Development and evaluation of the raindrop size distribution parameters for the NASA Global Precipitation Measurement Mission ground validation program. *Journal of Atmospheric and Oceanic Technology, 37*(1), 115–128. https://doi.org/10.1175/jtech-d-18-0071.1

Tokay, A., and Short, D. A. (1996). Evidence from tropical raindrop spectra of the origin of rain from stratiform versus convective clouds. *Journal of Applied Meteorology and Climatology, 35*(3), 355–371. https://doi.org/10.1175/1520-0450(1996)035%3c0355:eftrso%3e2.0.co;2

Tokay, A., Wolff, D. B., and Petersen, W. A. (2014). Evaluation of the new version of the laser-optical disdrometer, OTT Parsivel[2]. *Journal of Atmospheric and Oceanic Technology, 31*(6), 1276–1288. https://doi.org/10.1175/jtech-d-13-00174.1

Torres, D. S., Porrà, J. M., and Creutin, J.-D. (1998). Experimental evidence of a general description for raindrop size distribution properties. *Journal of Geophysical Research: Atmospheres, 103*(D2), 1785–1797. https://doi.org/10.1029/97jd02065

Torres, D. S., Porrà, J. M., and Creutin, J.-D. (1994). A general formulation for raindrop size distribution. *Journal of Applied Meteorology and Climatology, 33*(12), 1494–1502. https://doi.org/10.1175/1520-0450(1994)033%3c1494:agffrs%3e2.0.co;2

Uijlenhoet, R. (2001). Raindrop size distributions and radar reflectivity–rain rate relation-
ships for radar hydrology. *Hydrology and Earth System Sciences, 5*(4), 615–628.
https://doi.org/10.5194/hess-5-615-2001

Uijlenhoet, R., Steiner, M., and Smith, J. A. (2003). Variability of raindrop size distribu-
tions in a squall line and implications for radar rainfall estimation. *Journal of
Hydrometeorology, 4*(1), 43–61. https://doi.org/10.1175/1525-7541(2003)004%
3C0043:vorsdi%3E2.0.co;2

Ulbrich, C. W. (1983). Natural variations in the analytical form of the raindrop size distri-
bution. *Journal of Climate and Applied Meteorology, 22*(10), 1764–1775. https:
//doi.org/10.1175/1520-0450(1983)022%3C1764:nvitaf%3E2.0.co;2

Ulbrich, C. W. (1985). The effects of drop size distribution truncation on rainfall integral
parameters and empirical relations. *Journal of Climate and Applied Meteorol-
ogy, 24*(6), 580–590. https://doi.org/10.1175/1520-0450(1985)024%3C0580:
teodsd%3E2.0.co;2

Ulbrich, C. W., and Atlas, D. (1984). Assessment of the contribution of differential polar-
ization to improved rainfall measurements. *Radio Science, 19*(1), 49–57. https:
//doi.org/10.1029/rs019i001p00049

Ulbrich, C. W., and Atlas, D. (2007). Microphysics of raindrop size spectra: Tropical con-
tinental and maritime storms. *Journal of Applied Meteorology and Climatology,
46*(11), 1777–1791. https://doi.org/10.1175/2007jamc1649.1

Unal, C. (2015). High-resolution raindrop size distribution retrieval based on the
Doppler spectrum in the case of slant profiling radar. *Journal of Atmospheric
and Oceanic Technology, 32*(6), 1191–1208. https://doi.org/10.1175/jtech-d-
13-00225.1

van Leth, T. C., Leijnse, H., Overeem, A., and Uijlenhoet, R. (2020). Estimating raindrop
size distributions using microwave link measurements: Potential and limita-
tions. *Atmospheric Measurement Techniques, 13*(4), 1797–1815. https://doi.org/
10.5194/amt-13-1797-2020

Villermaux, E., and Bossa, B. (2009). Single-drop fragmentation determines size distri-
bution of raindrops. *Nature Physics, 5*(9), 697–702. https://doi.org/10.1038/
nphys1340

Vivekanandan, J., Zhang, G., and Brandes, E. (2004). Polarimetric radar estimators based
on a constrained gamma drop size distribution model. *Journal of Applied Mete-
orology, 43*(2), 217–230. https://doi.org/10.1175/1520-0450(2004)043%3c0217:
preboa%3e2.0.co;2

Watanabe, Y., and Ingram, D. M. (2016). Size distributions of sprays produced by vio-
lent wave impacts on vertical sea walls. *Proceedings of the Royal Society London:
Mathematical, Physical and Engineering Sciences, 472A*(2194), 20160423. https:
//doi.org/10.1098/rspa.2016.0423

Williams, C. R., Bringi, V. N., Carey, L. D., Chandrasekar, V., Gatlin, P. N., Haddad, Z. S., Meneghini, R., Joseph Munchak, S., Nesbitt, S. W., Petersen, W. A., Tanelli, S., Tokay, A., Wilson, A., and Wolff, D. B. (2014). Describing the shape of raindrop size distributions using uncorrelated raindrop mass spectrum parameters. *Journal of Applied Meteorology and Climatology*, *53*(5), 1282–1296. https://doi.org/10.1175/jamc-d-13-076.1

Willis, P. T. (1984). Functional fits to some observed drop size distributions and parameterization of rain. *Journal of Atmospheric Sciences*, *41*(9), 1648–1661. https://doi.org/10.1175/1520-0469(1984)041%3c1648:fftsod%3E2.0.co;2

Yakubu, M. L., Yusop, Z., and Yusof, F. (2014). The modelled raindrop size distribution of Skudai, Peninsular Malaysia, using exponential and lognormal distributions. *The Scientific World Journal*, *2014*, 361–703. https://doi.org/10.1155/2014/361703

Yang, Z., Liu, P., and Yang, Y. (2019). Convective/stratiform precipitation classification using ground-based Doppler radar data based on the K-nearest neighbor algorithm. *Remote Sensing*, *11*(19). https://doi.org/10.3390/rs11192277

Zhang, G., Vivekanandan, J., and Brandes, E. (2001). A method for estimating rain rate and drop size distribution from polarimetric radar measurements. *IEEE Transactions on Geoscience and Remote Sensing*, *39*(4), 830–841. https://doi.org/10.1109/36.917906

Zhang, G., Vivekanandan, J., Brandes, E. A., Meneghini, R., and Kozu, T. (2003). The shape–slope relation in observed gamma raindrop size distributions: Statistical error or useful information? *Journal of Atmospheric and Oceanic Technology*, *20*(8), 1106–1119. https://doi.org/10.1175/1520-0426(2003)020%3C1106:tsriog%3E2.0.co;2

Before I came here I was confused about this subject.
Having listened to your lecture I am still confused.
But on a higher level.

Enrico Fermi

Acknowledgements

There are no limits when you are surrounded by people who believe in you,
or by people whose expectations are not set by the short-sighted attitudes of society,
or by people who help to open doors of opportunity, not close them.

Neil deGrasse Tyson

My PhD finally comes to the end and I can not realize that now I am writing the most challenging lines of my thesis: the acknowledgments, where I should fit all the great people who helped to complete this work. This thesis would have not been possible without the support of many individuals, to whom I feel the need to express my gratitude.

First and foremost, I would like to express my sincere gratitude to my promotor Prof. dr. ir. Herman Russchenberg for giving me the opportunity to pursue my PhD degree in TU Delft. Herman supported my ideas and requests giving me the necessary freedom for my research. Since the initial interview and in every meeting his feedback, expressed through challenging and unexpected questions which often made me feel uncomfortable. However, I quickly realized that his intention was to encourage me to think out of the box and to see things from a different perspective. Moreover, I am particularly grateful for his contributions in leading the Department of Geoscience and Remote Sensing, Ruisdael Observatory, and promoting public awareness about climate crisis.

I would like to equally thank my copromotor Dr. Marc Schleiss, who served as my daily supervisor, together with Ir. Christine Unal as daily cosupervisor over the last six years. I could not have asked for a more supportive supervisory team, always available to provide advice for all the challenges I faced as a PhD candidate. Marc is perhaps the most well-rounded researcher at this high level I have met, and it was great pleasure working with him. His positive attitude, scientific integrity, and constructive criticism on my work helped me crucially enhance the quality of my research. Special thanks to him for his patience during our meetings every time I struggled with finding the correct words to express my thoughts in English. On the other hand, Christine, with her friendly behavior and scientific guidance introduced me to the beautiful world of weather radar. Her passion in the field of atmospheric remote sensing has always amazed me and she quickly became a source of motivation. Also, special thanks to her for the meticulous proofreading of my documents finding small inconsistencies in equations, tables and graphs even when I used tiny, unreadable fonts for the elements of the latter (axis labels, ticks, legends, etc.). Marc and Christine's questions and suggestions have played a major role in shaping this thesis. But more importantly, they taught me to be more confident in my results and become more independent researcher. We walked through the PhD journey together, and I feel privileged for having the chance to do that with you guys!

In addition, I would like to express my sincere gratitude to all members of my doctoral committee for time and efforts to review my work, providing valuable comments and suggestions. I also want to thank all the anonymous reviewers who improved my

Curriculum Vitæ

Christos *Gatidis*

02-06-1990   Born in Kavala, Greece

Education

2018–2024   **Ph.D. in Atmospheric Remote Sensing**
Delft University of Technology, Delft, the Netherlands
Thesis: Variability of the raindrop size distribution: model and estimation uncertainties across different scales
Promotor: Prof. dr. ir. H.J.W. Russchenberg
Copromotor: Dr. M.A. Schleiss

2013–2016   **M.Sc. in Atmospheric Sciences and the Environment**
University of Ioannina, Ioannina, Greece
Thesis: Seasonal variability and spatial distribution of lightning activity over Greece and their connection to atmospheric circulation over Mediterranean Sea.
Promotor: Prof. dr. A. Bartzokas

2008–2012   **B.Sc. in Mathematics**
University of Ioannina, Ioannina, Greece

2005–2008   **High School Diploma**
General Lyceum of Chrysoupoli, Kavala, Greece

2002–2005   **Middle School Diploma**
General Gymnasium of Chrysoupoli, Kavala, Greece

Work experience

Current	**Meteorologist** Weathernews Inc., Sea Planning, Athens, Greece
2018–2021	**Teaching assistant** Department of Geoscience and Remote Sensing, Faculty of Civil Engineering and Geosciences, Delft University of Technology, Delft, the Netherlands
2017	**Internship (Operational Meteorologist / Research Assistant)** Weatherquest, Norwich, United Kingdom
2016	**Internship (Research Assistant)** Laboratoire d'Aérrologie (LAERO), Université Toulouse III (Paul Sabatier), CNRS, OMP, Toulouse, France
2014–2015	**Teaching assistant** Laboratory of Meteorology, Department of Physics, University of Ioannina, Ioannina, Greece

List of peer-reviewed journal publications

1. **Gatidis, C.**, Schleiss, M., and Unal, C. (2024). A new power-law model for μ-Λ relationships in convective and stratiform rainfall, *Atmospheric Measurement Techniques*, 17, 235–245, https://doi.org/10.5194/amt-17-235-2024.

2. **Gatidis, C.**, Schleiss, M., and Unal, C. (2022). Sensitivity analysis of DSD retrievals from polarimetric radar in stratiform rain based on the μ-Λ relationship, *Atmospheric Measurement Techniques*, 15, 4951–4969, https://doi.org/10.5194/amt-15-4951-2022.

3. **Gatidis, C.**, Schleiss, M., Unal, C., and Russchenberg, H. (2020). A critical evaluation of the adequacy of the gamma model for representing raindrop size distributions, *Journal of Atmospheric and Oceanic Technology*, 37, 1765–1779, https://doi.org/10.1175/jtech-d-19-0106.1.

4. **Gatidis, C.**, Lolis, C.J., Lagouvardos, K., Kotroni, V., and Bartzokas, A. (2018). On the seasonal variability and the spatial distribution of lightning activity over the broader Greek area and their connection to atmospheric circulation, *Atmospheric Research*, 208, 180-190, https://doi.org/10.1016/j.atmosres.2017.08.024.

List of conference contributions

1. **Gatidis, C.**, and Paschos, F. (2023). Meteorological applications from the perspective of a private weather provider, *16th International Conference on Meteorology, Climatology and Atmospheric Physics (COMECAP), Athens, Greece*, https://doi.org/10.3390/environsciproc2023026013, (Oral presentation).

2. **Gatidis, C.**, Schleiss, M., and Unal, C. (2022). Sensitivity analysis of μ-Λ relationship in stratiform rain, *11th European Conference on Radar in Meteorology and Hydrology (ERAD), Locarno, Switzerland*, (Poster presentation).

3. **Gatidis, C.**, Schleiss, M., Unal, C., and Russchenberg, H. (2019). How adequate is gamma model for representing raindrop size distributions?, *39th International Conference on Radar Meteorology (American Meteorological Society, AMS), Nara, Japan*, (Oral presentation).

4. **Gatidis, C.**, Lolis, C.J., Lagouvardos, K., Kotroni, V., and Bartzokas, A. (2016). A study on the intra-annual variation and the spatial distribution of lightning activity over Greece, *13th International Conference on Meteorology, Climatology and Atmospheric Physics (COMECAP), Thessaloniki, Greece*, (Oral presentation).